Magnetism of postglacial lavas from Snæfells volcano, Iceland: Field reconstruction and archeomagnetic dating

ALMA MATER LEOBIENSIS

Thesis submitted for the degree of Master of Science
Diplomarbeit zur Erlangung des akademischen Grades des Diplomingenieurs

Elisabeth Anna Tauber

Supervisor

Dr. habil. Dipl.-Geophys.

Roman Leonhardt

I declare in lieu of oath, that I wrote this thesis

and performed the associated research myself,

using only literature cited in this volume.

Elisabeth Tauber

Leoben, 2011

Acknowledgements

This master thesis was initiated and supervised by Dr. habil. Dipl.-Geophys. Roman Leonhardt, whom I greatly thank for numerous discussions and supportive advices.

Furthermore I would like to thank Professor Robert Scholger for his support and help in finding a balance between work and my master thesis.

I am very grateful to my colleagues Nina Gegenhuber, Karin Gruber and Marlis Resch for proofreading my work, supporting me and for their motivating discussions.

I would like to express my gratitude to Georg Walach, who helped me during the last few months spent in our office.

I would like to thank Melanie Pichler, who was by my side for so many years, and also Alexander Maier for his support during the last few months.

I owe the greatest thanks to my family, especially my mother, Regina Tauber, who supported and encouraged me over the years and always believed in me and my goals.

Index

1 Introduction 1

2 Fundamentals 4

3 Regional Geology and Volcanogenic Hazards 20

3.1 Regional Geology of Iceland 21

3.1.1 Mid-Ocean Ridges and the Icelandic Plume 21

3.2 Volcanic Evolution of Iceland 22

3.2.1 Subarial Evolution of Iceland 22

3.2.2 Spreading Centers and Volcanic Center 24

3.2.3 Mineralogy 26

3.2.4 Ice Interaction 28

3.3 The Snæfellsnes Peninsula 31

3.3.1 Local Geology 31

3.3.2 Post-Glacial Activity 33

3.3.3 Volcanic Hazard of Snæfellsjökull 36

4 Methods and Results 39

4.1 Rock Magnetism 40

4.1.1 High Temperature and Low Temperature Measurements 40

Analysis of Low and High Temperature Measurements 41

Results and Interpretation of Low and High Temperature Measurements 44

4.1.2 The Anisotropy of Magnetic Susceptibility (AMS) 49

Analysis of the Anisotropy of Magnetic Susceptibility 51

Results of Anisotropy of Magnetic Susceptibility - AMS 53

4.1.3 Thermomagnetic Stability 57

4.1.3.1 Analysis of Thermomagnetic Stability by ARM Measurements 57

4.2 Paleodirections 73

Analysis of Paleodirections 74

Results of Paleodirection and Mean Direction 75

4.3 Paleointensities 84

4.3.1 Thellier-Experiments 84

Analysis of Thellier Measurements 87

Results of Analyses with Thellier Tool 89

4.4 Dating 95

4.4.1 Archeomagnetic Dating 97

5 Discussion 106

6 Appendix 112

7 References 153

Abbreviations

AF	Alternating field
AMS	Anisotropy of magnetic susceptibility
ARM	Anhysteretic remanent magnetization
CRM	Chemical remanent magnetization
D, Dec	Declination
H	Magnetic field
I, Inc	Inclination
M	Magnetic moment
MD	Multi domain
NRM	Natural remanent magnetization
PCA	Principle component analysis
PSD	Pseudo single domain
pTRM	partial thermoremanent magnetization
SD	Single domain
T, mT	Tesla, Millitesla
TRM	Thermoremanent magnetization

List of figures

Figure 1: Geographical setting of Iceland 3

Figure 2: Stereographic projection of plotted anisotropy directional data. 7

Figure 3: Exchange coupling of magnetic materials. 12

Figure 4: Magnetic dipole 15

Figure 5: Geological setting of Iceland 25

Figure 6: Subglacial volcanic edifices in northern Iceland 29

Figure 7: Geological map of the Snæfellsnes peninsula 32

Figure 8: The map of lava flows round the volcano 36

Figure 9: Curie temperature determination 42

Figure 10: Physical Curie temperature determination 42

Figure 11: Low and high-temperature measurement of min-type 1 44

Figure 12: Characterization of min-type 2 46

Figure 13: Low and high temperature measurements of min-type3. 47

Figure 14: Example for min-type 4 48

Figure 15: Geofyzika MFK1-FA Kappabridge from AGICO 49

Figure 16: Positions for AMS measurements for the Kappabridge 50

Figure 17: The figure displays the plotted anisotropy data of site BUH 52

Figure 18: Stereoprojection of AMS data 55

Figure 19: Cryogenic magnetometer in the laboratory in Gams 58

Figure 20: Sample PV1_11a as example for ARM treatment. 59

Figure 21: Susceptibility measurement of BUH 200°C 61

Figure 22: Susceptibility measurement of BUH 400°C. 62

Figure 23: Susceptibility measurement of BUH 700°C. 64

Figure 24: Results of ARM measurements and alteration types 66

Figure 25: Orthogonal projection of specimen BEH1_12a and sample PV1_25a 75

Figure 26: Demagnetization plot of BLH1_12a 76

Figure 27: Demagnetization plot of BEH1_12a 76

Figure 28: Results of paleodirectional analyses 78

Figure 29: Group statistic results of paleodirections. 81

Figure 30: Principal overview of the modified Thellier method 87

Figure 31: Representative examples of paleointensity determination. 89

Figure 32: Example for calculation with RenDate 96

Figure 33: Age determination of Beruvikurhraun.BEH. 97

Figure 34: Age determination of BDH. 99

Figure 35: Age determination of HAH 100

Figure 36: The match probability of site DRH 101

Figure 37: The age determination of site SV. 102

Figure 38: Age determination of HK. 104

Figure 39: Age determination of HNH 105

List of tables

Table 1: Table of the largest volcanic eruptions in the past 23

Table 2: Ancient volcanic eruptions of the Snæfellsjökull. 35

Table 3: Paleodirection results from Snæfellsjökull 83

Table 4: Criteria classes A and B for analysis with Thellier Tool. 88

Table 5: Paleointensity results from Snæfellsjökull 94

Abstract

Recent volcanic eruptions in Iceland demonstrate the importance of assessing volcanogenic hazards. Individual volcanic events occur on average at 5-year intervals while larger eruptions could occur in cycles of 500–1000 years. The determination of historic eruptions, calculation of the frequency of past eruptions, and definitions of eruption cycles as well as of all volcanic processes that may occur are essential for assessing volcanogenic risks. Paleomagnetic investigations are ideal contributions for determining the age of historical lava flows as well as defining eruption cycles. The advantage of this method is that dating is determined for lava flow itself. Other methods often use secondary sources, e.g. the dating of organic material from tephra layers, the origin of which is often ambiguous. Samples from fourteen different lava flows were taken from the Snæfells peninsula in west Iceland. All sampled sites correspond to post-glacial holocene lava flows, related to volcanic activity at Snæfells. The samples were subjected to paleomagnetic and rock magnetic analyses in order to obtain reliable intensities and directions of the ancient magnetic field. Curie-temperatures, measurements of anisotropy of magnetic susceptibility (AMS) and thermally dependent anhysteretic remanent magnetization (ARM) measurements are used to proof the reliability of paleomagnetic information and furthermore to subdivide the samples into specific groups regarding alteration and mineralogy. Paleodirection results yield average inclinations between 54° and 82° and declinations between 290° and 45°, as expected for the high northern latitude. According to rock magnetic results and the classification into alteration- and mineralogy-types, a pre-selection for further paleomagnetic measurements was conducted. Thirty-eight samples were chosen for a modified Thellier-type paleointensity determination, which includes alteration checks and domain state checks. The results allow the estimation of the previously unknown ages of the Holocene flows in the vicinity of Snæfells. For this purpose, the paleomagnetic directions were compared to inclination, declination and also to field intensity by using a Bayesian archeomagnetic dating approach. Two of the investigated lava flows correlate and confirm existing age determination of tephra layers. It was possible to relate one flow, which was previously correlated to an older event, to an eruption that occurred 1000 years later. Three of the determined lava flows are dated with more than 4500 years BP. Furthermore, an additional event occurring 2770 years BP was identified.

Zusammenfassung

Die Bedeutung der Gefahrenanalysen von Vulkanen wird durch die jüngsten Eruptionen auf Island erneut aufgezeigt. Einzelne vulkanische Ereignisse treten im Allgemeinen in Intervallen von 5 Jahren auf, wobei größere Eruptionen in Zyklen von 500 – 1000 Jahren auftreten können. Die Untersuchungen von historischen Eruptionen, die Berechnung der Häufigkeit vergangener Eruptionen und die Abschätzung von Eruptionszyklen sind unumgänglich für eine Risikoanalyse. Mit Hilfe paläomagnetischer Untersuchungen ist es möglich Altersdatierung von historischen Lavaflüssen durchzuführen und Eruptionszyklen zu berechnen. Der große Vorteil besteht darin, dass der Lavafluss direkt datiert wird und nicht auf sekundäre Quellen wie z.B. organische Materialien in Aschelagen, deren Zusammenhang mit bestimmten Lavaflüssen oft nicht eindeutig ist, zurückgegriffen werden muss. Für diese Untersuchungen wurden Proben von vierzehn verschiedenen Lavaflüssen der Snæfells Halbinsel in West Island, genommen. Alle diese Probenahmestellen entsprechen postglazialen Lavaflüssen die durch vulkanische Aktivitäten des Snæfells entstanden sind. Die Proben der jeweiligen Lavaflüsse wurden paläomagnetischen und gesteinsmagnetischen Untersuchungen unterzogen um Daten der damals vorherrschenden magnetischen Intensität und die Richtung des damaligen magnetischen Feldes zu bestimmen. Weiters wurden Curie Temperaturen gemessen, die Anisotropie der magnetischen Suszeptibilität (AMS) und temperaturabhängige Remanenz Messungen (ARM) durchgeführt, um die Zuverlässigkeit der paläomagnetischen Information zu überprüfen. Anhand dieser Messungen war es möglich, die Proben in verschiedene Gruppen bezüglich ihrer Alteration und Mineralogie zu unterteilen. Resultate der Paläorichtungen zeigen Werte der Inklination zwischen 54° und 82° und der Deklination zwischen 290° und 45°, welche durchaus für diese Region zu erwarten sind. Anhand dieser gesteinsmagnetischen Messungen und der Klassifizierung in Alteration und Mineralogie Typen wurde eine Vorauswahl für die spätere Paläointensitätsmessungen getroffen. Achtunddreißig Proben wurden für eine modifizierte Paläointensitätsmessung nach Thellier, welche Überprüfungen der Alteration und des Domänenzustandes beinhalten, ausgewählt. Die Ergebnisse erlauben eine Datierung der bis dahin unbekannten Alter der holozänen Lavaflüsse rund um den Snæfells Vulkan. Die Methodik der Datierung umfasst Kalkulationen für Inklination und Deklination, sowie für die Feldintensität, welche mit den Feldrichtungen anhand einer Bayesischen archäomagnetischen Referenzkurve verglichen wird. Die Daten für zwei der Lavaflüsse bestätigen und korrelieren mit bereits vorhandenen Altersdatierungen von Aschelagen. Ein Lavafluss, der bisher mit einem älteren Ereignis in Verbindung gebracht wurde, konnte einem Ausbruch zugeordnet werden, der 1000 Jahre später stattfand. Drei der untersuchten Lavaflüsse konnten mit einem Alter von mehr als 4500 Jahren BP datiert werden. Weiters konnte ein zusätzliches vulkanisches Ereignis, welches vor etwa 2770 Jahre BP stattfand, von einem Lavafluss datiert werden.

1 Introduction

Iceland is located in the south of the Arctic Circle between 63° N and 67° north (Fig. 1). Today, glaciers cover about 11 % of Iceland’s surface. During the Wechselian Ice Age (Bourgeois et al., 1998) glaciers covered almost the whole island (Andrews et al., 2000). The climatic conditions in Iceland are harsh and rough.

Iceland is known for its volcanic eruptions. After the eruption of the Eyjafjallajökull volcano in spring 2010 the volcanic hazard level of Iceland is again quite a current topic. The efforts to predict volcanic eruptions and thus to save people in the hazard area is a great task for natural sciences. Thus, risk assessments were carried out to evaluate the hazards of volcanic processes and eruptions. A complete risk analysis contains the record of past eruptions of the volcano being researched, and the frequency of eruptions. Furthermore, these data help to define cycles of the eruptions. In addition, various kinds of volcanic processes and the affected area of possible occurrences have to be determined.

The investigated volcano is the Snæfells, which has been very famous since Jules Verne described the entrance for the journey to the center of the earth at Snæfellsjökull. During a field trip to Iceland in summer 2009, Dr. Roman Leonhardt took samples of various holocene lava flows of the Snæfells peninsula. The working area is shown in Figure 1 and marked with a black rectangle. In this study we focus on postglacial lavas since the last ice age.

The aim of this thesis is the age determination of lava flows by means of archeomagnetic dating using paleodirection and paleointensity of the rocks. This is supported by rock magnetic analyses of given samples.

For rock magnetic research the Curie temperatures, the anisotropy of magnetic susceptibility and thermally dependent ARM were subjected. In accordance with the high temperature measurements, the samples were subdivided into four different mineralogy types. The ARM analyses enable the characterization of four different alteration types to get an ideal selection for further paleointensity determinations.

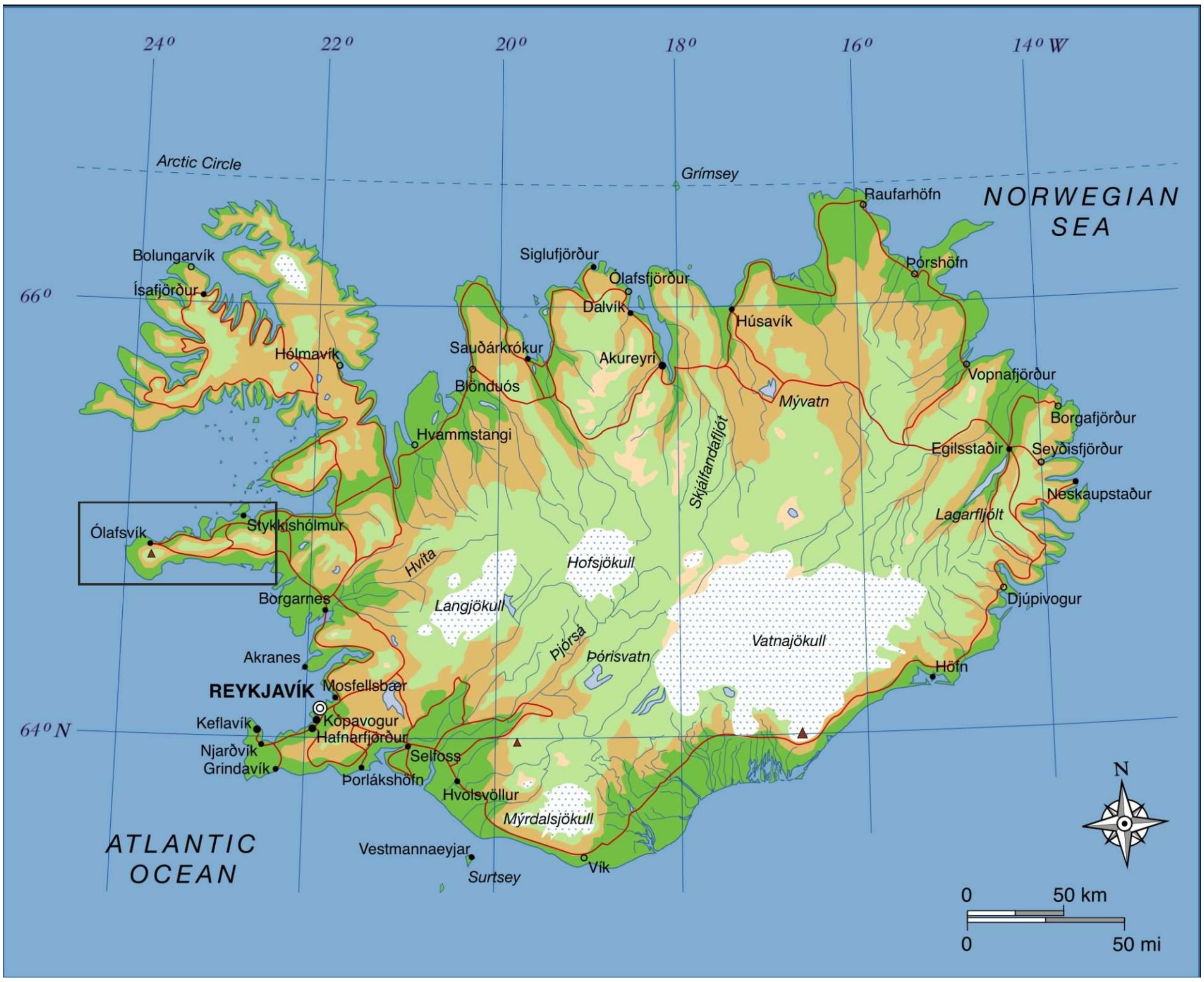

Figure 1: Geographical setting of Iceland. The black rectangle marks the area of work, the Snæfells peninsula.

The compromise of AMS data, mineralogy types and alteration types yield the pre-selection for further Thellier type measurements and age dating.

This thesis was written within a research project financially supported by FWF-P21221 and conducted at the Department of Geophysics of the University Leoben under supervision of Dr. Roman Leonhardt.

2 Fundamentals

Fundamentals

The following definitions of magnetic principles closely follow Morris (2003), Soffel (1991) and Butler (1992) and cover the majority of principles, abbreviations and definitions used in this thesis. Several other special definitions that are not covered in this chapter are found in the specific context.

Alternating field demagnetization (AF)

Alternating field demagnetization measurements are a means of characterizing magnetic particles in the specimens and are a measurement step for the Thellier experiments. A stepwise demagnetization of the samples enables the establishment of the remaining magnetic intensity. The AF is carried out by subjecting a specimen to an alternating magnetic field of gradually decreasing magnitude in the presence of a zero direct magnetic field. The alternating field is produced by passing an alternating current through a coil. Maximum obtainable fields are usually around 100 mT. The current ramps up to produce the selected peak alternating field (Morris, 2003).

AF demagnetization is most effective for rocks that contain magnetite or titanomagnetite as the dominant ferromagnetic mineral. An advantage of this measurement is that it does not produce chemical alteration in a specimen as might occur during thermal demagnetization. AF demagnetization is not effective for rocks in which hematites or goethites represent the remanence-carrying minerals. They have coercivities that exceed the peak field of most AF demagnetization systems (Morris, 2003).

Anhysteretic Remanent Magnetization (ARM)

Measurements of the anhysteretic remanent magnetization are conducted in order to determine the thermal stability of tested samples. A magnetic remanence is acquired when a ferromagnetic grain is subjected simultaneously to alternating and direct magnetic fields.

In principle, these kinds of measurements generate remanent magnetization by applying a well defined DC field during AF demagnetization. The ARM will be compared to the NRM.

Anisotropy of magnetic susceptibility (AMS)

The anisotropy of magnetic susceptibility, AMS, is a property of a material whereby an identical magnetic field applied in different directions produces different intensities of induced magnetization. AMS reflects the statistical alignment of platy or elongated magnetic grains. AMS is defined in terms of the magnetic susceptibility ellipsoid (Fig. 2), which has principal axes along the directions of maximum (k_1), intermediate (k_2) and minimum (k_3) susceptibility. If $k_1=k_2=k_3$, the ellipsoid is spherical and the specimen has an isotropic magnetic susceptibility. In the case of $k_1 \approx k_2 > k_3$; the ellipsoid is oblate (disc-shaped), and if $k_1 > k_2 \approx k_3$, the ellipsoid is prolate (cigar-shaped).

Oblate susceptibility ellipsoids (Fig. 2c) are commonly observed in sedimentary rocks and in rocks with significant foliation, with k_3 oriented rectangularly to the bedding and foliation, respectively.

Prolate ellipsoids (Fig. 2b) can be observed in volcanic lava flows and current-deposited sediments, where k_1 is aligned parallel to the paleoflow direction (Tarling and Hrouda, 1993).

Significant magnetic anisotropy can also be produced during the straining of rocks, and has been used to infer the orientation of the strain ellipsoid (Morris, 2003).

Anisotropy of remanent magnetization is a kind of magnetic anisotropy, in which acquired remanent magnetization may deviate from the direction of the magnetic field at the time of remanence acquisition. This kind of magnetic anisotropy is of special interest for paleomagnetic analysis (Butler, 1992), and in particular for paleointensity determination (Rogers et al.1979, Veitch et al., 1984). The anisotropy of the remanent magnetization is roughly estimated by the far less elaborate AMS determination, although AMS is only a poor proxy for the remanence fabric in the samples (Selkin et al., 2000).

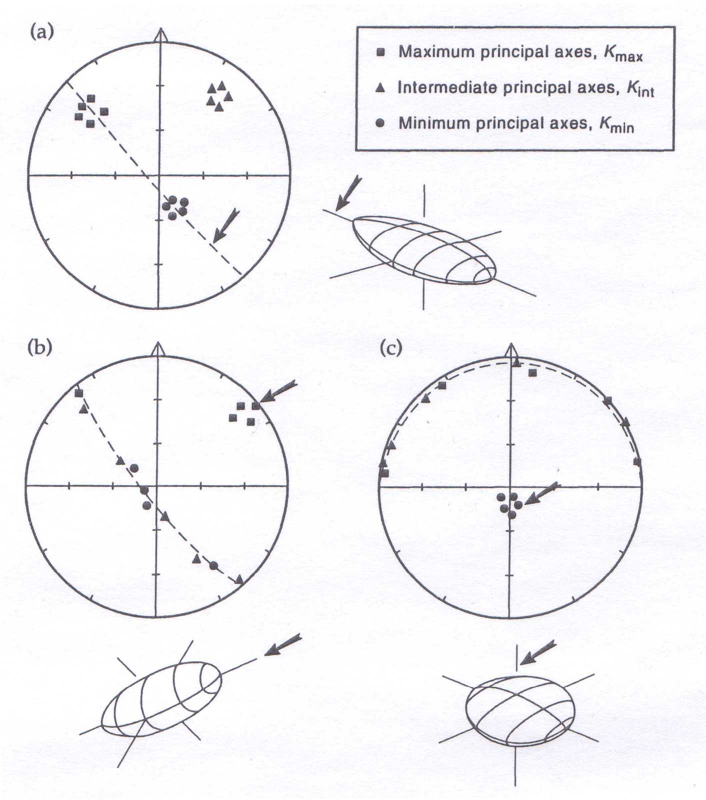

Figure 2: Stereographic projection of plotted anisotropy directional data. The projections shown here are the equal-area type. The standard projection is polar, i.e. the center corresponds to an inclination of ± 90° and the circumference corresponds to the horizontal plane. The direction of maximum principal axes, k_{max}, are plotted as squares, that of the intermediate principal axes, k_{int}, as triangles, and the direction of minimum principal axes, k_{min}, as circles. For (a) triaxial ellipsoids with the same orientation, the three principal axes form distinct groups, while (b) prolate ellipsoids of similar orientation have their maximum axes well grouped and their intermediate and minimum axes distributed within a girdle at 90° from the maximum directions. (c) Oblate ellipsoids of similar orientation show well-grouped minimum axes, and their maximum and intermediate directions fall within a girdle 90° from the minima. As the principal axes are orthogonal, it is not always necessary to plot the intermediate axes (Tarling and Hrouda, 1993).

Antiferromagnetism

Antiferromagnetism (Fig. 3b) describes the behavior of solids with anti-parallel couplings between adjacent layers of atomic magnetic moments, where opposing layers have equal magnetic moments and thus produce no net magnetization (Morris, 2003). In antiferromagnetic substances, the magnetic moments are aligned partly in parallel. The sum of magnetic moments of a part-volume is zero, and there is no magnetization without an external field.

Bulk Susceptibility

The magnetic susceptibility is due to all minerals in a specimen, but usually dominated by ferromagnetic minerals (Butler, 1992).

Chemical Remanent Magnetism (CRM)

Chemical changes that form ferromagnetic minerals below their blocking temperature in a magnetizing field result in acquisition of chemical remanent magnetism CRM. Chemical reactions involving ferromagnetic minerals include either alteration of ferromagnetic minerals or the precipitation of a ferromagnetic mineral from solution (Butler, 1992). This kind of process can affect the magnetomineralogical composition of lavas after emplacement, and thus alter the recorded magnetic field information.

Coercivity

Magnetic grains are magnetized along 'easy' axes (domains). The coercivity of a single-domain grain is the magnetic field that must be applied to force its magnetization to flip direction by 180° (i.e., resulting in a 'permanent' change in direction of magnetization upon removal of the field) (Morris, 2003).

Confidence limits (α_{95})

The semi-angle of the cone of 95% confidence surrounding a mean direction of magnetization or pole positions (Morris, 2003).

Curie temperature (T_c)

The Curie temperature is a significant property of magnetic minerals and is used to distinguish between different magnetic minerals. Above the Curie temperature, ferri- and ferromagnetic minerals behave like paramagnetic minerals. The Curie temperature is characteristic and helps to identify minerals.

Since interatomic distances increase upon heating, the strength of exchange coupling between atomic magnetic moments decreases with increasing temperature, thereby reducing the resultant magnetization. At the Curie temperature, interatomic distances reach such a high level that exchange coupling breaks down, the atomic magnetic moments become independent, and the mineral exhibits paramagnetism. Upon cooling below the Curie temperature, exchange coupling and ferro- or ferrimagnetism reappear (Morris, 2003). The phenomenon of the Curie point or Curie temperature is defined for ferri- or ferromagnetic minerals, and known as the Néel temperature in antiferromagnetic minerals.

In the case of ferromagnetic minerals or substances, above the Curie temperature, magnetic moments are oriented randomly, resulting in a zero net magnetization. In this region, the substance is paramagnetic, and its susceptibility is given by the Curie-Weiss law.

$$K = C / T - T_c \qquad \text{(equation 1)}$$

C describes the Curie constant, T the absolute temperature and T_c the Curie temperature (Petrovsky and Kapicka, 2006).

Declination (D)

The declination is the horizontal angle between either a magnetization vector, or the Earth's magnetic field and geographic north (Morris, 2003).

Diamagnetism

A characteristic of diamagnetic minerals or substances is that their molecules do not have a permanent magnetic moment. Usually, all rocks or substances display diamagnetic behavior. Diamagnetism is the result of complete electron shells orbiting around a nucleus. To measure diamagnetism in minerals, an external magnetic field has to be applied. This external magnetic field produces a small induced magnetization in the opposite direction to the applied field. This magnetization is proportional to the applied field and decays to zero when the field is removed. The magnetic susceptibility is low and negative ($\sim 10^{-5}$ SI), and often overprinted by para- and/or ferromagnetism (Morris 2003, Soffel 1991).

Domains

The magnetization within a small region with a ferromagnetic grain is uniform in direction and has a preferred orientation, aligned either along specific crystallographic axes, known as magnetocrystalline 'easy' axes, or along the length of the grain (for small, elongate grains). These axes are hereafter referred to as 'preferred axes'. In larger grains (> 10 μm), a number of volume elements are present, each of which has its magnetization aligned along the preferred axis. These volume elements are the so-called magnetic domains. The domains form an arrangement which minimizes the total magnetic energy of the grains.

Three different types of magnetic behavior, depending on grain size, are determined:

(a) **Single-domain behavior:** SD grains have a high coercivity and their magnetization can be stable over geological time periods. They are thus efficient paleomagnetic carriers. SD grains of cubic magnetite are smaller than 0.1 µm, whereas elongate SD magnetite grains can be up to 1 µm in length.

(b) **Multi-domain behavior:** MD grains have a low coercive force, and their magnetization decays with time. MD grains are less effective paleomagnetic recorders than SD grains.

(c) **Pseudo-single-domain behavior:** The presence of crystal lattice imperfections in some MD grains prevents simple interaction between adjacent domains. For the resulting pseudo-single-domains, PSD, magnetic behavior is then closer to the intermediate size of some grains. In this case, the magnetic moments form a vortex pattern which produces high coercivity grains, but of lower total magnetic moments. The PSD grain-size interval for magnetite is about 0.1-1.0 µm. PSD grains exhibit significant time-stability of remanent magnetization, and can be important paleomagnetic carriers (Butler, 1992; Tarling and Hrouda, 1993; Morris, 2003).

The domain state of magnetic minerals is of particular importance for paleointensity determination, as MD behavior violates various basic conditions for obtaining reliable and correct field estimates (e.g. Coe et al., 1967b; Shcherbakova et al., 2000).

Ferromagnetism

Ferromagnetism occurs in substances in which the electron spins have been spontaneously coupled in a way that aligns all the individual spin magnetizations (Fig. 3a), even in the absence of an external applied magnetic field. This magnetization is described as spontaneous magnetization. Ferromagnetism is superimposed on paramagnetic behavior; if ferromagnetic properties are destroyed, e.g. by heating, previously ferromagnetic materials behave in a paramagnetic way (Tarling & Hrouda, 1993).

Ferrimagnetism

Ferrimagnetism describes the behavior of solids with anti-parallel couplings (Fig. 3c) between adjacent layers of atomic magnetic moments, where opposing layers have unequal magnetic moment and thus produce a net magnetization in the direction of the dominant layer (Morris 2003).

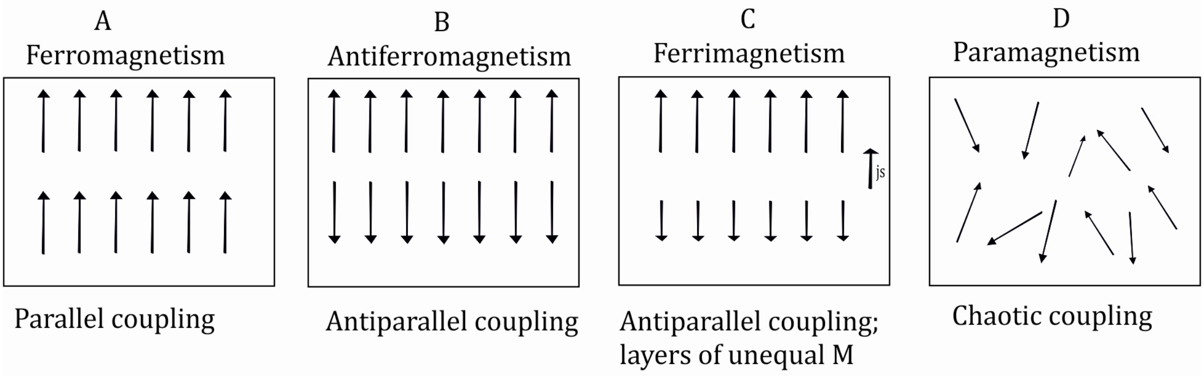

Figure 3: Exchange coupling of magnetic materials. The figure describes the exchange couplings for (a) ferromagnetic, (b) antiferromagnetic, (c) ferrimagnetic and (d) paramagnetic materials. The net magnetization for ferrimagnetic material is shown on the right; the net magnetization of antiferromagnetic material is zero; modified in accordance with Butler, (1992).

Fisher Statistics

Fisher (1953) derived a probability density function for vectors considered as points on a sphere, known as the Fisher distribution, which is used to statistically define the dispersion of a set of magnetization vectors around the mean direction and to perform statistical tests. The theoretical precision parameter, k, for the Fisher distribution varies from zero if all vectors in the total population are randomly distributed to infinity when they are all identical to the mean. The best estimate, k, of this precision parameter (based on the finite number of samples drawn from the total population) is simply given by:

$k = \frac{N-1}{N-R}$ for N > 7 and k > 3: (equation 2)

where R is the length of the resultant vector of the N individual magnetization vector values of k>10 indicating that the observed mean direction is close to the true mean of the total population. The Fisherian confidence limit associated with a calculated mean direction of magnetization is usually quoted for the 0.95 probability level and is given by:

$\alpha_{95} = cos^{-1}\left\{1 - \frac{N-R}{R}\left[\left(20\frac{1}{N-1}\right) - 1\right]\right\}$ (equation 3)

which, if k>7, can be approximated by:

$\alpha_{95} \approx \frac{140}{\sqrt{kN}}$ (equation 4)

There is a 95% probability that the true mean direction of the total population of magnetic vectors (from which the sampled population of magnetic vectors was drawn) will lie within this cone. A well-defined mean direction of magnetization will have a high value of k (>10) and a small α_{95} angle (< 15°) (Morris, 2003).

Inclination (I)

The inclination is described as the angle between either a magnetization vector or the Earth's magnetic field and the horizontal plane (Morris, 2003).

Magnetization (J)

The magnetic intensity, or magnetization, *J*, of a material is the net magnetic dipole moment per unit volume. To compute the magnetization of a particular volume, the vector sum of magnetic moments is divided by the volume enclosing those magnetic moments:

$J = \sum M_i \,/\, \text{Volume}\ [\text{A/m}]$ (equation 5)

M_i describes the constituent magnetic moment.

There are two types of magnetization: induced magnetization and remanent magnetization.

If a material is exposed to a magnetic field H, it obtains an induced magnetization, J_i. The quantities are related by means of the magnetic susceptibility, k (Butler, 1992):

$J_i = k\,H \quad [1]$ (equation 6)

Magnetic Field (H)

The magnetic field, *H*, in a region is defined as the force experienced by a unit positive magnetic charge placed in that region. A magnetic moment that is free to rotate will align with the magnetic field.

Within this study, H_{lab} describes the magnetic field with known intensity applied in the laboratory. H_{pal} describes the quested paleomagnetic field.

Magnetic Moment (M)

Magnetizations of the samples are usually obtained in terms of a magnetic moment. The magnetic dipole moment or the magnetic moment, M, can be defined by referring either to a pair of magnetic charges (Fig. 4a) or to a loop of electrical current (Fig. 4b). For the pair of magnetic charges, the magnitude of charge is m and an infinitesimal distance vector, l, separates the plus charge from the minus charge (Butler, 1992).

$M = ml$ (equation 7)

For a loop with area A, carrying electrical current I, the magnetic moment is

$M = I\,An$ (equation 8)

Where n is the vector of unit length perpendicular to the plane of the loop. The proper direction of n, and therefore M, is given by the right-hand-rule. The current loop definition of magnetic moment is basic in that all magnetic moments are caused by electrical currents (Butler, 1992).

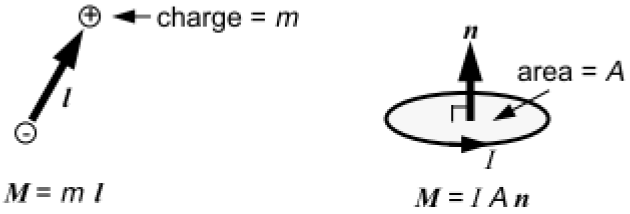

Figure 4: (a) A magnetic dipole constructed from a pair of magnetic charges. The magnetic charge of the plus charge is m, the magnetic charge of the minus charge is –m; the distance vector from the minus charge to the plus charge is l. (b) A magnetic dipole constructed from a circular loop of electrical current. The electrical current in the circular loop is I; the area of the loop is A; the unit normal vector n is perpendicular to the plane of the loop (Butler, 1992).

Magnetic Susceptibility (k)

The magnetic susceptibility can be regarded as the magnetizability of a material or substance. This expression uses a scalar for susceptibility, implying that J_i is parallel to H.

If J_i is not parallel to H, the material displays anisotropy of the magnetic susceptibility (Butler, 1992).

Natural Remanent Magnetization (NRM)

The natural remanent magnetization is the sum of all components of magnetic remanence acquired by natural processes. These factors consist of several components and depend on the magnetic history, the minerals and the present magnetic field (Telford et al., 1990; Morris, 2003).

For instance, the NRM of lava can include a primary thermoremanent magnetization, a secondary magnetization achieved during low-grade metamorphism, and a viscous remanent magnetization acquired in the present-day field. Components of magnetization are separated in laboratory measurements using stepwise demagnetization (Morris, 2003).

Paleointensity

The past intensity of the geomagnetic field is usually determined by analysis of the thermoremanent magnetization carried by an igneous rock. The standard procedure for paleointensity determination involves comparison of TRM acquired by a specimen when cooled in a known laboratory magnetic field with the natural TRM carried by the specimen (Thellier and Thellier, 1959; Coe 1967a). In this study, a modified version of the original stepwise Thellier-technique was used according to Leonhardt et al., (2004).

Paramagnetism

In contrast to diamagnetic minerals, paramagnetic minerals contain ions with uncompensated spin-moments (Fig. 3d). The electron pairs are not complete and not coupled. In an external field, the electronic spins start to process a magnetic moment which has the same direction as the applied field. Just like diamagnetism, paramagnetism disappears as soon as the applied field is removed. The electron-spin of the uncoupled electrons causes a partial alignment of atomic dipole moments and an increase of the total magnetization. Paramagnetic minerals have a positive susceptibility, are temperature dependent and are characterized by the Curie law (Morris, 2003; Soffel, 1991).

Principle Component Analysis (PCA)

Principle component analysis is used for the determination of paleodirections. This statistic determines the direction of a best-fit line through a set of magnetization directions obtained by stepwise demagnetization (as displayed on an orthogonal demagnetization diagram). A quantitative measure of the precision of the calculated best-fit line is given by the **maximum angular deviation (MAD).** There are three ways in which the PCA can be applied to demagnetization of data: (i) the line may be anchored to the origin; (ii) the origin may be used as a separate data point; or (iii) the origin may be ignored to produce a free line fit. Care must be taken if anchored line fits are used, since information from low intensity, high stability components may potentially be lost (Morris, 2003).

Remanent Magnetization

Remanent magnetization describes the permanent magnetization of a material after removal of the magnetization field. The remanent magnetization depends on the strength and the direction of the geomagnetic field at the time of magnetization acquisition and can be determined in ferro- and ferrimagnetic minerals (Morris, 2003).

Tesla (T)

Tesla is the unit of the magnetic field strength (H). In SI units, B in Tesla (fundamental units: kg s^{-1} C^{-1}) is strictly the magnetic induction, whereas

H is measured in Am^{-1} (fundamental units: $C\ s^{-1}\ m^{-1}$) and is the magnetic field (Morris, 2003).

Thermoremanent Magnetism (TRM) and partial Thermoremanent Magnetism (pTRM)

Thermoremanent magnetism (TRM) is the remanent magnetization that is produced by cooling from above the Curie temperature (T_c) in the presence of a magnetic field and forms the basis of the Thellier experiments. TRM is the type of remanent magnetization attained by most igneous rocks. The theory of TRM was adopted in 1949 when Neél (Neél, 1948) explained the stability of SD-TRM and confirmed Thellier's law (Thellier, 1938) of additivity and independence of pTRM carried by SD particles (Fabian, 2000). Many additional studies and modifications, which most follow the approach of Coe (1967a, 1967b), have been contributed since Thellier's fundamental work (Leonhardt et al., 2004). In these modifications, a stepwise demagnetization of the NRM is followed by stepwise acquisition of pTRM at the same temperature that is used for the demagnetization, or in reverse order (Leonhardt et al., 2004).

Upon cooling through the lowest blocking temperature of the assemblage of ferromagnetic grains within the rock, the total TRM of the rock is blocked in. The proportion of the total TRM acquired in a distinct temperature interval during cooling is known as a partial TRM (pTRM) (Morris, 2003). For the classical Thellier measurements, the NRM of rocks is taken as TRM (TRM_{pal}), which is acquired in an unknown paleomagnetic field (H_{pal}). By heating the sample above the Curie temperature and cooling in a field (H_{lab}), an artificial TRM (TRM_{lab}) is acquired and compared with the NRM ($NRM = TRM_{pal}$).

The partial thermoremanent magnetism that is used for the Thellier experiments is not a classical pTRM. The so-called pTRMa or pTRM* is different, as the samples gain the partial thermoremanent magnetization to defined heating steps. During the Thellier type measurements, the pTRM* is gained by heating the specimen to a heating step (T_i) and applying a field (H_{lab}) during cooling to room temperature (T_0).

3 Regional Geology and Volcanogenic Hazards

3.1 Regional Geology of Iceland

3.1.1 Mid-Ocean Ridges and the Icelandic Plume

Iceland is located at the interface of the North American and the Eurasian plate and their causing effects of the constructive plate boundary. The northern part of the Mid-Atlantic Ridge currently has a spreading rate of 0.9 cm/a in each direction around Iceland (Hardarson et al., 1997). In fact, in Iceland the incidence of a divergent plate boundary and a mantle plume coincide, and about 15 Ma ago they lifted Iceland up above the sea level (Kristjánsson et al., 2003).

In general, a mid-ocean ridge does not reach sea level; but Iceland is an exceptional case. The reason for this is related to a mantle plume below the ridge (Jacoby and Gudmundsson, 2007). A plume is a body of upwelling heat in the astenosphere, which transports hot and less dense material upward from the lower mantle. The material flow of crustal and mantle rocks in opposite directions induce strong lateral forces and stress. The stress reduces, due to various factors, in fracturing, earthquakes and volcanic eruptions (Gudmundsson and Kjartansson, 1984).

Recorded by flood basalts in West Greenland, the age of the mantle plume ranges back to 65 Ma (Thordarson and Höskuldsson, 2006). The spreading center of the young north Atlantic slid over the hot-spot and loaded the volcanoes with deep mantle material. Henceforth, the magma supply was higher compared to the rest of the spreading center and a marine plateau was built up. This plateau was significantly higher than the normal Mid-Atlantic Ridge (Hug-Fleck, 1987, 1988). Since that time, the mantle plume has produced more than 10 Mio km^3 of magma in a region that reaches from Greenland over Iceland and the Faeroe Islands to Scotland (Thordarson and Höskuldsson, 2006). The current position of the mantle plume has been estimated from seismics and gravity anomalies, and characterized by the location of high $^3He/^4He$ volcanics (Eysteinsson and Gunnarsson, 1995). Today the center of the mantle plume is located under the Vatnajökull (Einarsson et al., 1997). Submarine volcanoes also build up through the ridge in the north and south. Over sixty submarine volcanoes are known in the area surrounding the Vestmannæyjar islands. In 1963, the emergence of the island of Surtsey could be seen within just a few weeks (Hug-Fleck, 1987).

3.2 Volcanic Evolution of Iceland

3.2.1 Subarial Evolution of Iceland

From a geological viewpoint, Iceland is quite a young volcanic island in the North Atlantic that owes its existence to a mantle plume and a mid-oceanic spreading center. According to Einarsson (1991), the history of Iceland can be divided into four main sections beginning with tertiary vulcanites from the Miocene and Pliocene, followed by basalts from the upper Pliocene to lower Pleistocene, plagonites from the middle Pleistocene and the Holocene as the last section (Einarsson, 1991).

The oldest rocks on Iceland were formed 17 million years ago and are located in the East and West of the island. In this time, the plateau rose above the sea level and massive flood basalts came over the young island. Due to the sea floor spreading, the eastern and western parts of the island drifted apart while the flood basalts were still erupting. This east-west strain can be observed by dint of magneto-stratigraphy, because the flood basalts recorded the prevailing magnetic field with their appearance. Even the fracture zone of the Mid-Atlantic ridge can be traced in Iceland. The central fracture zone in Iceland was constantly filled from the active volcanism, and many volcanoes are now higher than the plateaus of the basalts. The processes of building of the fracture zone and the filling from the volcanoes are in balance (Hug-Fleck, 1987; 1988).

The main volcanic zone in the Quaternary, upper Pliocene and lower Pleistocene runs from the Reykjanes ridge to the north-east and from the center of Iceland to the north. Parallel to the north-south trending rift segment, another rift segment, westwards from the Langjökull, trending to the Skagi peninsula in the North, was active. The volcanism in this zone is inactive, except on the Snæfellsnes peninsula. The ice shields in the Pliocene and Pleistocene are located in general on the volcanic zone. Sediments and pyroclastica from the Quaternary are found along the main volcanic zones, on Snæfellsnes and north Iceland. Cured tephra and pumice from interglacials formed elongated plagonit ridges and cones that still characterize volcanoes from the ice age. The Móberg formation started 700 ka ago and comprised interglacial sediments and lava flows, the subglacial plagonit ridges and table mountains. The Holocene was initiated with the melting of the big ice shields of Iceland (Búdajökull). Around 930 A.D., Eldgjá erupted, producing an enormous amount of lava. It is presumed that 200-250 volcanic eruptions have occurred during the last 110 years (Gudmundsson and Kjartansson, 1984). The following table gives an overview of the most recent large eruptions.

Eldgjá	930 AD
Hekla	1104
Öræfajökull	1362
Öræfajökull	1727
Katla	1918
Skaftáreldar	1783
Laki	1783-1784
Askja	1875
Vestmannæyjar	1973

Table 1: Table of the largest volcanic eruptions in the past, modified according to (Gudmundsson and Kjartansson, 1984).

The eruption of Öræfajökull was still larger than Hekla in 1104, and the volcano spewed three times more tephra than Hekla. Eruptions from Katla caldera caused more than 16 eruptions and melt-water floods as well as massive damage. Kjartansson expects another eruption to occur soon. The eruptions of 1783 from Skaftáreldar were so large that almost 20% of the population of the time died from the sulphuric acid and other gasses resulting the eruption. The effect of the eruption in 1973 was the creation of the Vesterman-islands (Gudmundsson and Kjartansson, 1984).

3.2.2 Spreading Centers and Volcanic Center

In the early Cenozoic, an active spreading center in the Labrador Strait was located between Greenland and the North American continent. In the Mid-Cenozoic, the Labrador Strait was free and the North Atlantic ridge between Greenland and Scandinavia tools over the divergent motions of the North American and the Eurasian lithospheric plate (Thordarson and Höskuldsson, 2006).

The direction of the divergence between the North American and the Eurasian plate is N110°E, and the spreading rate is 0.9 cm/a (Hardarson et al., 1997). Today, the lithospheric accretion occurs in the so-called Neovolcanic Zone, 25.000km^2 (Gudmundsson and Kjartansson, 1984), which connects the Reykjanes Ridge in the Southwest to the Kolbeinsey Ridge in the North. The Neovolcanic Zone is covered by interglacial and subglacial basalts which are dated at less than 700 ka. On both sides of the Neovolcanic Zone, the external zone consists of Tertiary basalts deposited from 16 Ma to 700ka (Moorbath et al., 1968; Saemundsson, 1979).

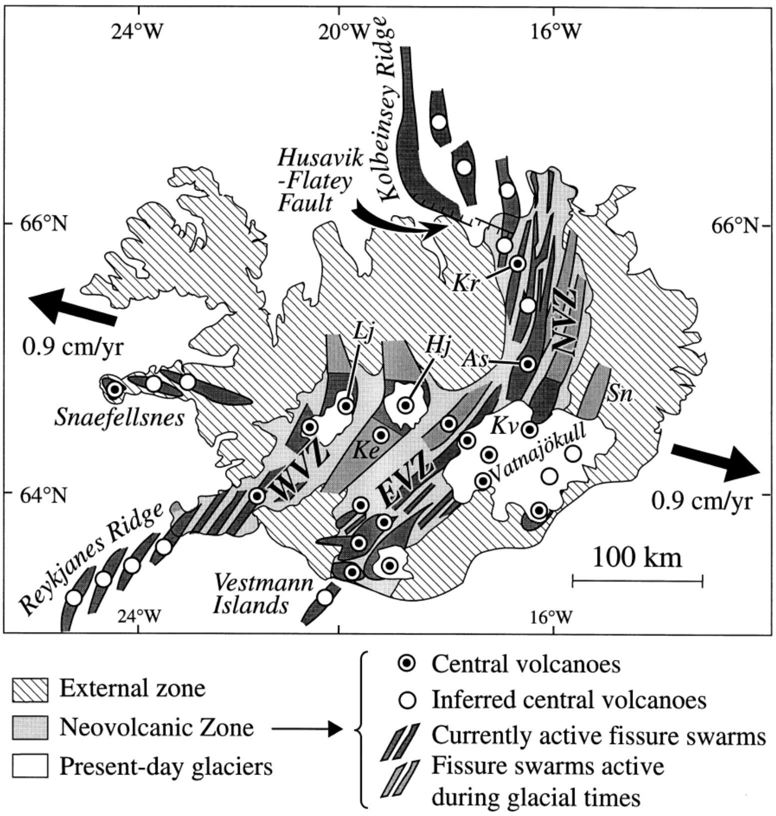

Figure 5: Geological setting of Iceland at the junction between the Reykjanes Ridge to the southwest, and the Kolbeinsey Ridge to the north. Current tectono-volcanic activity occurs in the Neovolcanic Zone, composed of three main branches, the Northern (*NVZ*), Western (*WVZ*) and Eastern (*EVZ*) Volcanic Zones. The Snæfellsnes peninsula, in western Iceland, is also active. Lithospheric spreading occurs in fissure swarms associated with central volcanoes (dark grey: currently active swarms; light grey: swarms active during glacial times, evidenced by this work). Offset of the Neovolcanic Zone with respect to the Mid-Atlantic Ridge is accommodated by en-échelon arrangement of the swarms and by the WNW-trending Husavik–Flatey transfer fault. *As* D Askja; *Hj* D Hofsjökull; *Ke* D Kerlingarfjökull; *Kr* D Krafla; *Lj* D Langjökull; Sn: Snæfellsnes. Graphic is taken from Bourgeois et al (1998).

The Neovolcanic Zone (Fig. 5) has been subdivided into three rift systems (Saemundsson, 1979): The Western Volcanic Zone (WVZ), which is the onland prolongation of the Reykjanes Ridge; the Eastern Volcanic Zone (EVZ), which is situated 100 km to the east and extends from Vestmann Islands in the south to the Vatnajökull glacier in the north; and the Northern Volcanic Zone (NVZ), which reaches from the Vatnajökull glacier to the northern coast of Iceland (Bourgeois et al., 1998). In these zones, the lithospheric accretion is controlled by NNE-trending fissure swarms composed of tension fractures, normal faults and eruptive fissures. Most of these are associated with central volcanoes underlain by magma chambers, which control magma supply at the surface (Saemundsson,

1978) (Fig.5). These fissure swarms are arranged in a left-stepping en-échelon pattern in the south and in a right-stepping en-échelon pattern in the north.

The northern coast is completed by a WNW-trending transfer fault (the Husavik-Flatey fault), which connects the westernmost fissure swarm of the NVZ to the Kolbeinsey Ridge. This disposition was attributed to the fact that the axis of the mantle plume is situated in the east of the island, thus causing an eastward deflection of the Neovolcanic Zone with respect to the Mid-Atlantic Ridge (Tryggvason et al., 1983). The WNW-trending fissure swarms are active in the Snæfellsnes peninsula in north-west Iceland (Bourgeois et al., 1998). Some factors of the plume have to be considered; a release of stresses, an uplift of ductile rock at depth and abrupt changes in heat-flow are factors influencing magma-generation (Gudmundsson and Kjartansson, 1984).

Iceland is known for high volcanic activity throughout the entire country. In fact, the inhabitants of Iceland owe the existence of their island to the volcanoes. Large eruptions are observed to occur in cycles of five years. Numerous volcanoes lurk in the glaciers of Iceland, such as the Kverkfjökull, the Grímsvötn-caldera in Vatnajökull, and the Katla-caldera in Mýrdalsjökull (Gudmundsson and Kjartansson, 1984). The Eyjafjallajökull was also a lurking volcano until March 2010.

3.2.3 Mineralogy

Due to the geological settlement, about 90% of the rocks are eruptives and the rest are clastic sediments of eroded basalts. The coasts are also made of black basalt sands. Metamorphic rocks are non-existent. The main minerals in the black basalts are the white plagioclase, the dark augite (pyroxene) and the greenish olivine with magnetite and apatite as secondary minerals. Very large crystals of the main minerals of the size of a fingernail are to be found. Basalts are compact and can be subdivided into three groups according to the chemical content, ranging from basic rocks to acid rocks (rhyolite) (Gudmundsson and Kjartansson, 1984).

Mafic magma or rocks: The silica content is below 52% and the main minerals are olivine, pyroxene and feldspar. After crystallization, these lavas are called basalts. If they crystallize deep in the lithosphere, they are called gabbros, and due to slow cooling they develop larger crystals (Hug-Fleck, 1987). This magma is very hot, flows well and forms ropy-lava or Pahoe-hoe lava. The eruptions are calm, can last for a very long time and build a lava lake inside the crater. The volcanoes emit the degassing in a thin smoke column, forming lava shields or small lava rings (Gudmundsson and Kjartansson, 1984).

Intermediate magma or rocks: These rocks have a silica content of 52–65% and contain less olivine and pyroxene than mafic rocks. The vulcanites are andesites, and the magmatites are called diorites (Hug-Fleck, 1987). The magma is colder, more viscous and riches in gasses. The eruption of these volcanoes is mixed; therefore the keen degassing in the vent produces tephra, and the lava flows cool as scoria-lava. Coarse tephra is produced by lava-fountains up to hundreds of meters in height that hurl it up in the air. These eruptions are caused by fissures that are also common in central volcanoes, and form a row of spatter and scoria cones (Gudmundsson and Kjartansson, 1984).

Felsic magma or rocks: The silica content is above 65%, which means that quartz can be also produced. Vulcanites are called dazites or rhyolites, and plutonites are known as granodiorites (Hug-Fleck, 1987). The magma is highly viscous; the eruptions cause large explosions that throw out massive amounts of tephra and debris, and the resulting ash cloud can travel many kilometers. Most of the volume of tephra is thrown out in a short time and creates a hole in the earth with a small lake. If the magma erupts sub-aquatically in the sea or under ice shields, it undergoes rapid cooling. As a result of cooling, degassing and low pressure, tephra is formed. These loose particles are thrown around the eruption vent in phreatic explosions and form tuffs (hyaloclastites) in the area surrounding the volcano. The evaporated water also creates an eruption-cloud. This type of eruption was common during the glacial periods of the Ice Age (Gudmundsson and Kjartansson, 1984).

3.2.4 Ice Interaction

It was mentioned that Iceland has seen at least five glacial and interglacial cycles since the Mid-Pleistocene (Bourgeois et al. 1998) as well as over 20 glaciations since the Pliocene. These glaciations are recorded in glacial deposits and can be correlated to the $\partial^{18}O$ record of deep-sea sediments (Geirsdóttir et al. 2007). The last two peak levels of Iceland's ice caps, Alftanesjökull (12,500 years ago) and Búdajökull (11,000 years ago), are equivalent to Würm or Weichsel (North Europe) and Wisconsin in North America (Hug-Fleck, 1987). The Ice Age lasted 2-3 million years and the glaciers formed extensive and varied landscapes all over the island. The ice caps can be subdivided into three groups:

As ice caps proper with many outlets, the ice caps are over 150 km^2 and can be up to 1000 m thick. For example: Mýrdalsjökull and Vatnajökull.

Ice shields: small ice caps that are resting on one single mountain. For example: Eiríksjökull.

Slope glaciers: They are thin ice sheets on high mountains like Snæfellsjökull or between mountains like Tindafjallajökull (Gudmundsson and Kjartansson, 1984).

In the Pleistocene, many volcanoes were formed under subglacial conditions. These volcanoes can be divided into two main types: table volcanoes and ridge-shaped hyaloclastite deposits (Bourgeois et al., 1998).

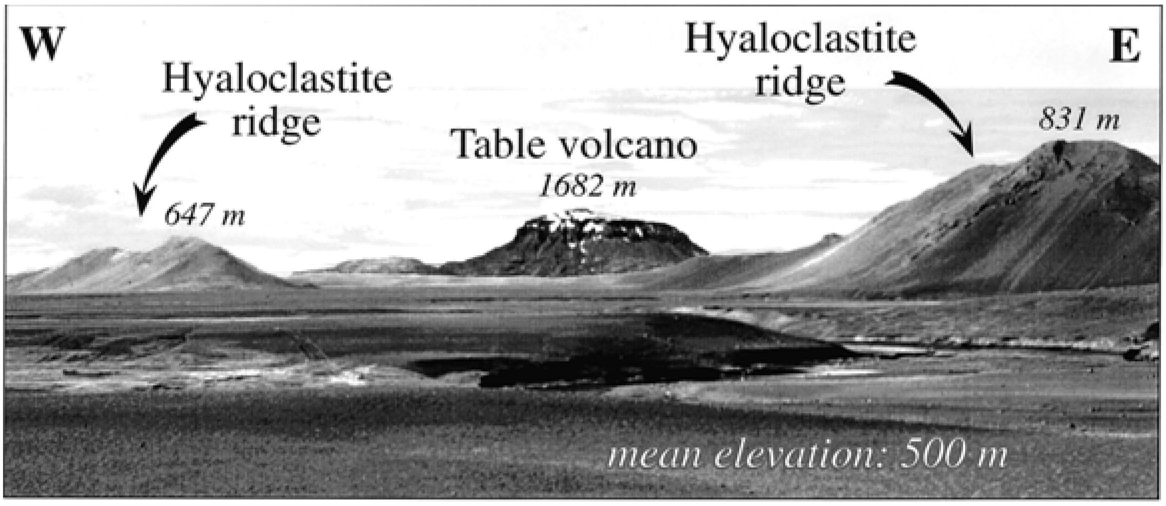

Figure 6: Two kinds of subglacial volcanic edifices in northern Iceland. Herdubreid, in the background, is a typical table volcano. The lower part is composed of volcanic breccias, hyaloclastites, and pillow lavas deposited under subglacial conditions. It is capped by aerial lava flows emplaced above the ice cap surface that form a shield volcano. In the foreground are two typical hyaloclastite ridges emplaced under subglacial conditions above eruptive fissures. Graphic is taken from Bourgeois et al. (1998).

Table volcanoes result from central vent eruptions; they are the subglacial equivalent of shield volcanoes (Bourgeois et al., 1998; Werner et al., 1996) and form roughly circular, steep-sided and flat-topped maintains. They are a few kilometers in diameter and 200-1000 meters in height. Essentially, they consist of pillow lavas and hyaloclastites surrounded by volcanic breccias. If the magmatic supply is sufficient, the volcanoes grow up to the ice surface and are capped by flat aerial lava flows emplaced above the ice cap. The height of these volcanoes is a good indicator for the ice thickness at the time of their emplacement (Bourgeois et al., 1998; Allen, 1979). Hyaloclastite ridges (Fig. 6) are up to 35 km long and 2–4 km wide. They can reach a height of a few hundred meters. Hyaloclastite ridges are mainly aligned with the overall tectonic trend and are a subglacial equivalent of eruptive fissures. They consist of fragmented pillow lavas and hyaloclastites, which are similar to the base of table volcanoes (Allen, 1979).

Iceland’s largest volcanoes are hidden under the ice caps. It is not the eruptions themselves that are the most perilous effect, but rather the melting of snow and ice that is caused by these eruptions. The massive mud flows caused by eruptions can transport thousand of cubic meters of water and boulders per second (Hug-Fleck, 1987).

Earthquakes go hand in hand with volcanism and can reach magnitudes of over 7 in the north-east of Iceland (Gudmundsson and Kjartansson, 1984). The largest earthquakes in the history of Iceland occurred in 1934 in Dalvik (magnitude of 6.3), in 1963 in the north of Skagafjörður and in Kópasker in 1976 with a magnitude of 6.2. In the period from 1784 to 1896, around 20 big earthquakes are known to have occurred, and their magnitude was in the order of 7 and above (Gudmundsson and Kjartansson, 1984).

3.3 The Snæfellsnes Peninsula

3.3.1 Local Geology

The central rift system is marginally curved in the center of Iceland (Fig. 5). A possibility for this observation is that the system could in fact be two rift segments joined by an east-west trending fracture zone. The present Snæfells volcanic zone is probably a part or an extension of this EW-zone. But on the other hand: The Snæfellsnes could also be the dying remains of the former rift system in Iceland, which bisected the present peninsula of Snæfellsnes, and it is accordingly isolated (Gudmundsson and Kjartansson, 1984).

The Snæfells volcanic zone stretches WNW-ESE from Nordurárdalus in Borgarfjördur west along the Snæfellsnes peninsula. The zone includes three central volcanoes that are arranged en echelon (Jóhannesson et al., 1981) and differ from volcanic systems of the axial rift zones of Iceland, which, in contrast to Snæfellsnes, are characterized by a tensional stress field resulting in open fissures and normal faults (Saemundsson, 1978).

The Snæfellsjökull central volcano is the westernmost volcanic system of the Snæfellsnes volcanic zone. It is about 30 km long and stretches E-W from Maelifell in Stadarsveit to the tip of the peninsula. The volcanism in the eastern part is restricted to a narrow zone, but widespread in the western part, especially round the Snæfellsjökull. It appears that the activity has been more intense around the strato-volcano. The oldest rocks are found at the base of the volcano and are assumed to be more than 700,000 years old. They rest unconformably on an eroded tertiary basement. The cone of Snæfellsjökull consists of hyaloclastites that are formed during glacial and interglacial lava flows. Over 20 individual prehistoric lava flows have been identified so far. The eruption sites are either close to the top of the mountain, or in groups in the lowlands around the volcano. The craters close to the top usually erupt intermediate or acid magmas, in contrast to the basaltic magma erupted in the lowlands (Jóhannesson et al., 1981).

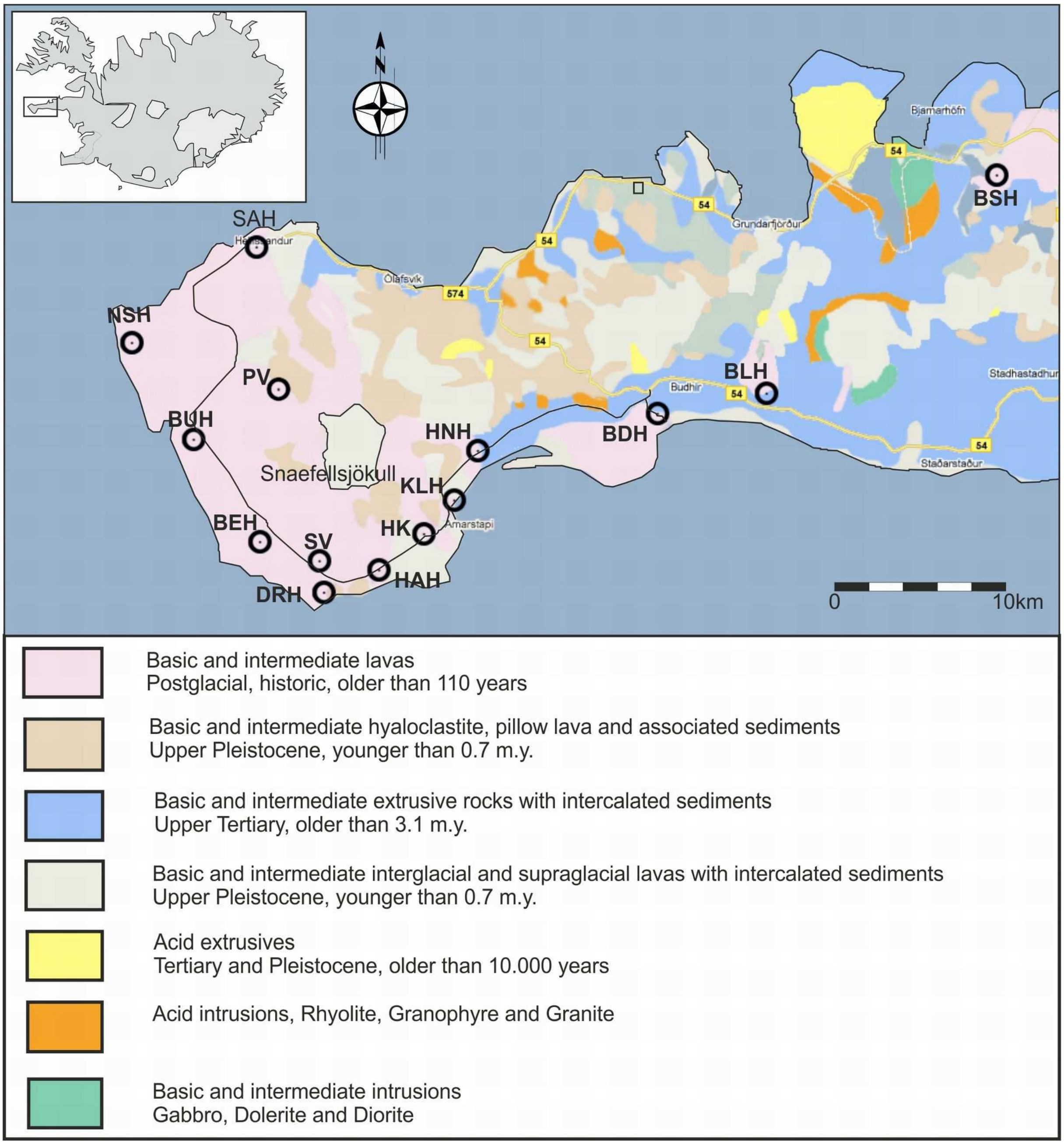

Figure 7: Geological map of the Snæfellsnes peninsula. The names of the sample sections are abbreviated and can be found in the list of abbreviations.

The geological map (Fig. 7) displays the Snæfells peninsula and the location of the site where samples were taken in abbreviations.

3.3.2 Post-Glacial Activity

Ancient volcanism in Iceland has a turbulent history. Not all past volcanic eruptions were reported, but since the settlement of Iceland, most of them have been documented by wise men or chieftains (Snorri goði).

Researched lava flows are distributed radial in every direction of the volcano; hence, the higher topography in the northeast of the volcano limits the spread of lava flows. Younger lava flows have also been identified on the low plains around the volcano, linked with local craters and a shield-type feature to the northwest. Pre-Holocene lava flows are found in the north and east of the volcano. Basaltic lava is produced from lower-flank craters and intermediate-to-silicic magma from the upper-flank craters. Lava flew from the main caldera and flank fissures thick with steep flow fronts. This indicates a viscous and slow flow. Flows on the lower land are thinner and have been described as less viscous lava that has a higher rapidity of flows (Pahoehoe lava – Helluhraun). Floods and lahars, transporting pumice clasts, have flown in most directions from the volcano. These floods were relatively small compared to floods from Katla and Grímsvötn, which can be seen by the smaller ice caps and the numerous directions of flow. Larger floods flowed to the north and east out of the main outlet glaciers, draining the caldera. It is assumed that some water-transported pumice deposits on the southern and western slopes were emplaced by post-eruption, rain-triggered lahars, remobilizing the thick, unconsolidated air fall pumice deposits. It has also been suggested that the Snæfells volcano may have experienced a lateral collapse/blast (like Mount St. Helens in 1980). Although no evidence has been found, this could happen again (H. Jóhannesson, pers. Comm., 2005, Smith et al., 2007; Smith et al., 2008).

It is mentioned that the central volcano of Snæfells erupted over 25 times in the last 10,000 years. These eruptions produced lava, tephra, jökullhlaups or lahrars. The three major Plinian eruptions are recorded (in radiocarbon year BP): 1855 a (±25), 3960a (±100), 7000a-9000a (see Fig. 8)(Steinthórsson, 1976; Jóhannesson et al., 1981; Larsen et al., 2002).

A summary of ancient eruptions of Snæfellsjökull (Table 2) is provided below. The data (taken from www.volcano.si.edu) are given in uncorrected radiocarbon years and calibrated to calendars years BP (before 1950) by means of the program Cablib6, Radiocarbon Calibration Program, Marine04.14C "global" marine calibration dataset (Stuiver, M., and Reimer, P.J., 1993). Corrected calendar years for layer Sn-1 are taken from and Larsen et al. (2002).

Uncorrected radiocarbon years (BP)	Cal ages (BP)	Cal ages (BP)	Area	(VEI)	Characteristics
1750 ± 150	1860-1520	1690 ± 170	Tephra layer SN-1		Central vent eruption, explosive eruption, lava flows
1855 ± 25	1820-1730	1775 ± 45			
2950 ± 500	2112-3329	2720 ± 600	NW flank (Raudhólar)	2	Flank (eccentric) vent, explosive eruption, lava flows
3960 ± 100	3820-4095	3960 ± 130	Tephra layer SN-2		Central vent eruption, explosive eruption
4220 ± 300	3916-4713	4300 ± 400	South flank (Thufuhraun)	0	Flank (eccentric) vent, lava flows
2970 ± 300	4853-5566	5200 ± 350	SE flank (Dagverdarahr	0	Flank (eccentric) vent, lava flows

			aun)		
6500 ± 1000	5863-8011	6900 ± 1000	East of Snæfellsjökull (Budaklettur)	2	Regional fissure eruption, explosive eruption, lava flow(s)
8000 ± 1000	7458-9721	8590 ± 1100	Tephra layer SN-3		Central vent eruption, explosive eruption
10410 ± 200	11222-11770	11500 ± 250			Explosive eruption

Table 2: Ancient volcanic eruptions of the Snæfells volcano. The uncorrected radiocarbon ages and the values of VEI (Volcanic Explosivity Index) are taken from the homepage www.volcano.si.edu and from Larson et al. (2002). The correction to calendar years BP was conducted with the help of Calib6 (Stuiver, M., and Reimer, P.J., 1993). The marine global curve was chosen for the correction in the range of ± 1σ. The age of the layers is reported in calendar years BP (before 1950) and rounded off to the nearest decade.

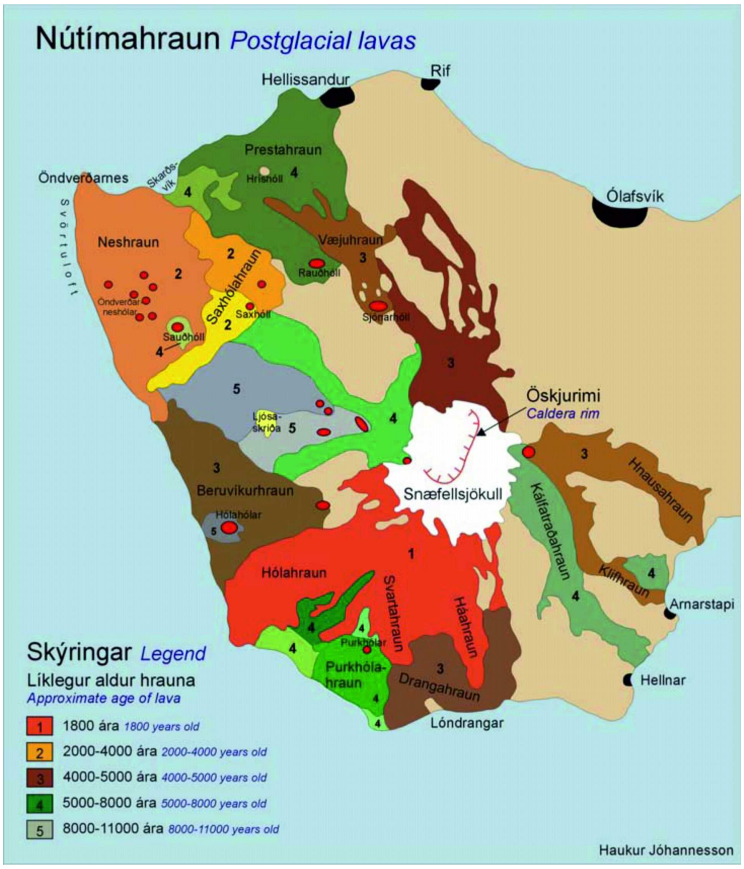

Figure 8: The map of Snæfells displays the distribution and age (in radiocarbon years) of lava flows round the volcano. (Smith, K. T., Sigurðsson, F., Sturkell, E. 2008 Palaeoenvironmental Reconstruction as a Tool in Hazard Assessment: a case study at Snæfellsjökull, Raunvísindaþing Natural Science Symposium, Program Abstracts. p 160).

3.3.3 Volcanic Hazard of Snæfellsjökull

A preliminary study of the volcanic risks at Snæfellsjökull was carried out by Smith, Sigmundsson and Freysteinn (2007). The assessment includes recorded data of past eruptions (see Fig. 8), a determination the frequency of past eruptions, a definition of the time period of reference, identification of volcanic processes that may occur, and the determination of the probability that an area will be affected by any volcanic event.

Two of the most likely scenarios are mentioned; small crater eruptions from the flanks or lowland, and the major central caldera eruption with limited or no ice cover.

Tephra will fall to the northeast due to the dominant wind direction. Tephra has been produced from the central volcano, from small local craters and fissures on the edge of the volcano and, in addition, on the low land surrounding Snæfellsjökull. The thickness of the tephra layers will decrease with distance from the volcano. The impact of tephra fall will mainly affect the northeast of the volcano.

Lava will flow along dominant channels and spread out over flatter surfaces. The locations depend on the position of craters and fissures. Holocene lava flows at Snæfellsjökull are mainly found to the west and south of the main volcano, and only small cones are found in the surrounding lowlands. Therefore, the south and west are more likely to experience lava flows. The relatively low speed of the lava flows should allow traffic diversions to be carried out in good time (Smith, Kate and Sigmundsson, Freysteinn, 2007).

Jökulhlaups depend on the ice cap and snow that cover the volcano at the time of the eruption. Nowadays, only a small ice cap covers Snæfellsjökull, and patterns of snow accumulations lead to the highest jökulhlaup risk to the north, with a lower jökulhlaup hazard level from ice- or snow-covered fissures and crates as well as the caldera rim to the south and west. Post-eruptive lahars caused by the moving of sediments by heavy rain are also very likely. Arnarstpi to the southeast is the settlement closest to a potential flow path (Smith, Kate and Sigmundsson, Freysteinn, 2007).

Earthquakes that are associated with eruptions of the volcano are likely, and could cause rock falls and damage to the roads.

Pyroclastic flows are likely and common for strato volcanoes, although so far no geological evidence has been found for Snæfellsjökull. A pyroclastica flow would follow drainages and may therefore be most likely to the north of the volcano. However, all drainages around the volcano would be a risk, in fact, and would bury or erode roads in their path as well as posing a serious risk to people and vehicles (Smith, Kate and Sigmundsson, Freysteinn, 2007).

Awareness of the fact that volcanoes erupt in several cycles of time is essential for all hazard assessments. In order to assess the hazard, it is necessary to record past eruptions and determine eruption cycles and the frequency of historical eruptions. Furthermore, a risk assessment of possible volcanic processes and their distribution area has to be carried out. For dating analyses, several measurements are used. One of these is C14 radiocarbon dating of tephra layers and, in addition, a tephra chronology and stratigraphy of analyzed data (see Table 2). The measured age in radiocarbon years BP has to be corrected to calendar years BP (before 1950). Another possibility for dating that I focus on in this thesis is the analysis of paleodirections and the determination of the magnetic field intensity. These data are correlated to historical data of field intensity, inclination and declination, which are specific for certain periods of time. By means of this technique, lava flows of the volcano are dated. This provides additional data on the tephra chronology for identifying eruption cycles of Snæfellsjökull as a contribution to volcanic hazard assessments.

4 Methods and Results

4.1 Rock magnetism

4.1.1 High Temperature and Low Temperature Measurements

Using high temperature measurement, the Curie temperature T_C can be determined, which provides information about magnetic mineralogy. Low-temperature measurements give additional information on transition temperature and thus mineralogy and domain state. To measure the temperature variations of the magnetic susceptibility, the MFK-1 Kappabridge, the CS-3 unit and the CS-L unit of AGICO-Instruments, were used. The Kappabridge consists of a non-magnetic furnace and a platinum thermometer.

The CS-L Low Temperature Cryostat and the MFK-1 Kappabridge were used for the low-temperature measurements. For this purpose, the samples had to be ground to a fine powder. At the beginning of this measuring process, the sample is placed in the measuring vessel, which is cooled down to -192°C by liquid nitrogen. When the starting temperature is reached, the liquid nitrogen is blown out of the Cryostat with argon gas. The specimen is automatically warmed up from -192°C to 5°C, controlled by the CS-3 Unit.

The CS-3 high temperature furnace was taken for the high temperature measurements. The finely ground powder of the samples was heated from room temperature to 700°C and cooled down again to room temperature. The CS-3 Unit controls the temperature during the whole measurement process and displays it on the screen. An argon environment is applied during the measuring in order to prevent oxidation of the sample.

The selected adjustments are:

Frequency 1: 976 [Hz]

Field: 200 [A/m]

Heating rate: fast [~11°C/min]

Analysis of Low and High Temperature Measurements

To identify Curie temperatures, different methods can be used. The two-tangent method, developed by Gromme et al. (1969), or the temperature dependence of magnetic susceptibility method, described by Petrovsky and Kapicka (2006), can be used.

Gromme et al. (1969) used the intersection point of two tangents to the thermomagnetic curve that bounds the Curie temperature (Fig. 9).

Moskowitz (1981) (Fig. 10) applied a method based on statistical physics for extrapolating the ferromagnetic behavior, expected from experimental data through the Curie temperature, to determine the point at which the ferromagnetic contribution reaches zero (Tauxe, 2009).

A third method for estimating Curie temperatures from thermomagnetic data, the differential method of Tauxe (1998), seeks the maximum curvature in the thermomagnetic curve. First, the derivative (dM⁄dT) is calculated, and these data are differentiated once again to produce d2M⁄dT2. The maximum in the second derivative occurs at the point of maximum curvature in the thermomagnetic curve, and is a reasonable estimate of the Curie temperature (Tauxe, 2009).

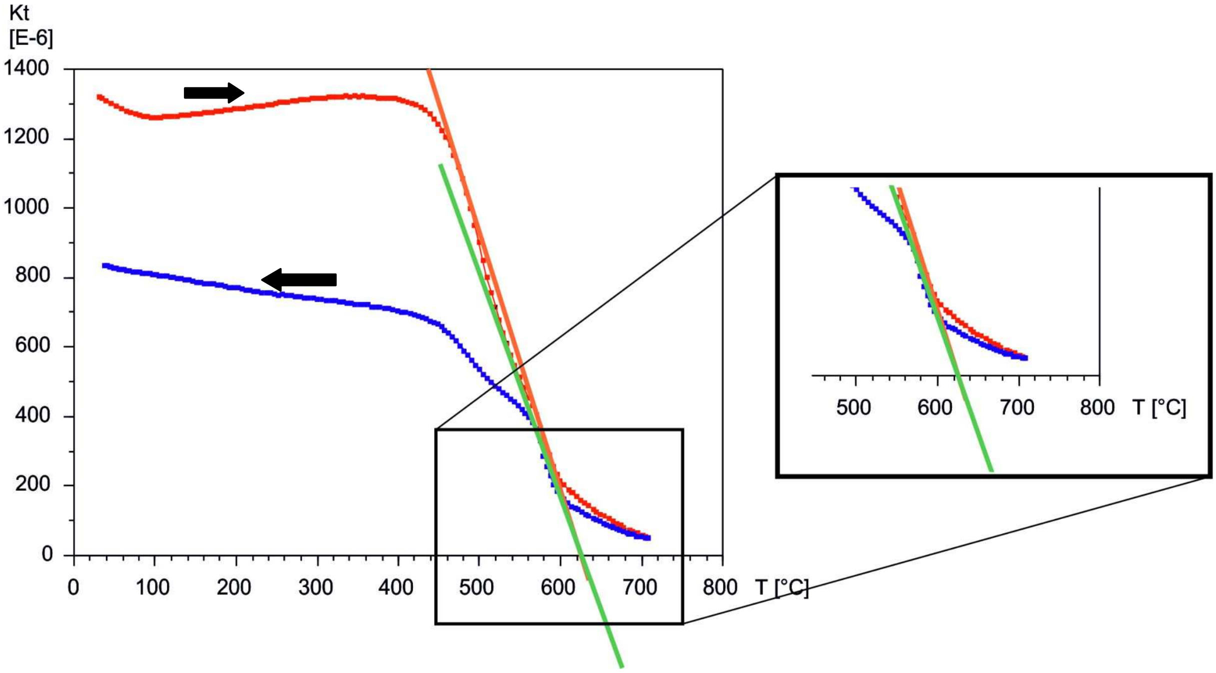

Figure 9: Curie temperature determination of specimen BUH1_700 according to Gromme et al. (1969). $T_c = 610°C$

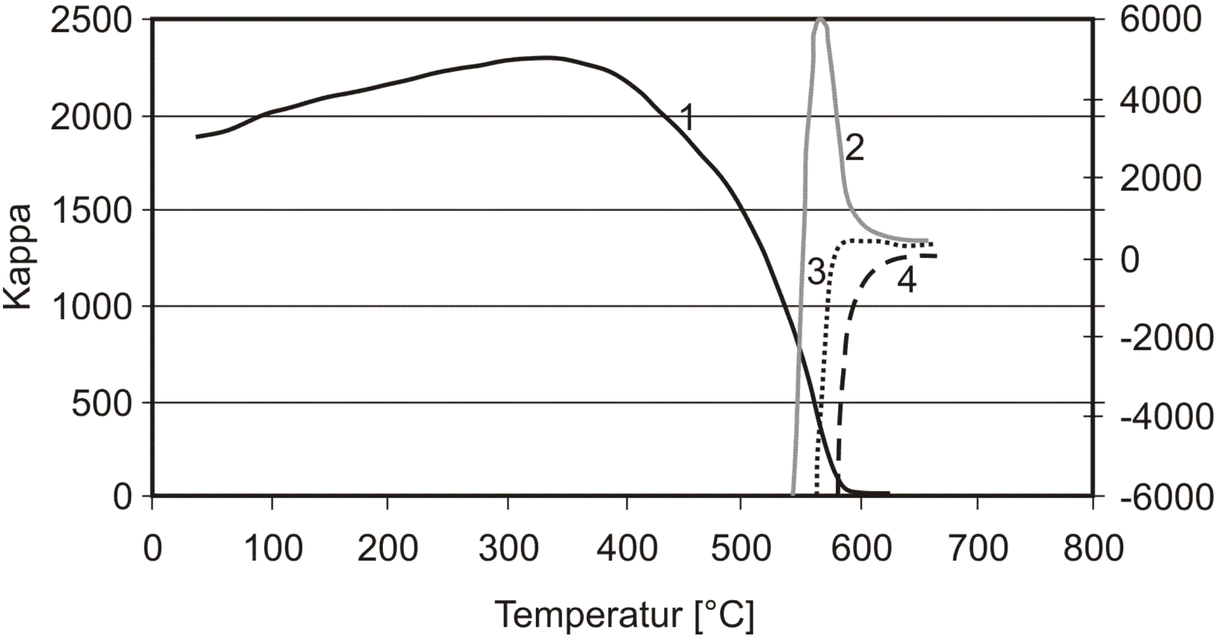

Figure 10: Physical Curie temperature determination according to Moskowitz (1981), from Hemetsberger (2002); 1: heating curve, 2: $k= C (T-T_c)$, estimation for T_c is too low; 3: $k=C/ (T-T_c)$ right estimation for T_c; 4: $k=C/ (T-T_c)$, estimation for T_c is too high. Curie temperature $T_c = 580°C$.

For these experiments, the two-tangent method was used to identify the Curie temperatures and additional the function 1/k versus temperature.

The diagram of the heating and cooling curve of each sample was analyzed with the Cureval 8.0 program from AGICO-Advanced Geoscience Instruments. To correct the measurements, an empty measurement was made before the high temperature and the low temperature measurements. With the Cureval 8.0 program, any noise can be corrected. The heating curve is given in red and the cooling curve in blue. The tangent was pointed to the highest peak of the increasing curve of both curves.

Each sample was measured in several steps:

Step 1: -192°C – 5°C

Step 2: 40°C – 200°C

Step 3: 40°C – 400°C

Step 4: 40°C – 700°C

Results and Interpretation of Low and High Temperature Measurements

According to the results of the low and high temperature measurements, the samples can be divided into four different mineralogy types:

Mineralogy type 1:	BEH, PV, HNH
Mineralogy type 2:	HK, DRH, SAH2
Mineralogy type 3:	SV, HAH
Mineralogy type 4:	BDH, (BLH)

Mineralogy type 1

The characteristics of type 1 are the reversibility of the heating (red) and cooling (blue) curve, and they show a clear decrease of the susceptibility at 60 °C.

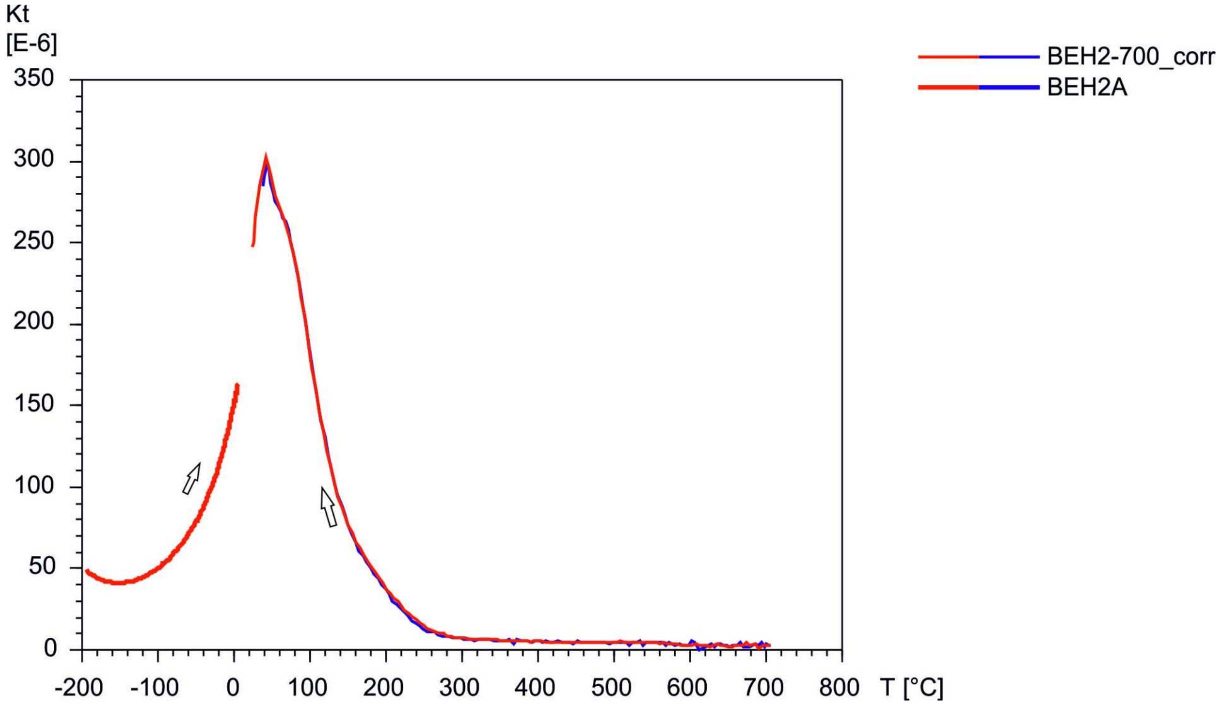

Figure 11: Low and high temperature measurement of specimen BEH2 in the range of -192°C to 700°C. The heating curve is shown in red, while blue denotes cooling.

Both samples, BEH2 (Fig. 11) and PV, show the same steep decrease of magnetic susceptibility at 60°C. The Curie temperatures were determined at 160°C and 580°C for BEH and HNH, and 580°C for PV. The Curie temperature at 580°C is determined for magnetite (Soffel, 1991) and 160°C for unexsolved titanomagnetite (TM 60). Thirty percent of the measured samples belong to min-type 1.

Samples of mineralogy type one are from the original magma. When the magma is produced from the mantle, the content of titanomagnetite is very high. Most of the samples are titanomagnetites TM 60. Titanomagnetite is a cubic mineral from the series of magnetite ($Fe3O4$) and ulvöspinell ($Fe2TiO4$), and can be described with: $xFe2TiO4*(1-x) Fe3O4$. A complete exsolution above 600°C is possible. Below this temperature, exsolution lamellae from ulvöspinell and magnetite are formed. The Curie temperature varies along the exsolution lamellae. Titanomagnetite 60 has a content of 60% of ulvöspinell and a Curie temperature of around 150-200°C (Soffel, 1991).

Mineralogy type 2

Min-type 2 shows a steep decrease of the magnetic susceptibility at 60°C and displays also very similar heating and cooling curves. Samples from HK (Fig. 12), DRH and SAH, display a Curie point at about 150°C and at about 580°C. In additional, to these characteristic temperatures, the samples show a Verwey transition in the low-temperature measurements, which is typical for magnetite. The Curie point at 150°C leads to the unexsolved titanomagnetite TM60. During cooling, the titanite oxidates from the magma, and the higher the content of magnetite, the lower the content of titan. The Curie temperature at 580°C is characteristic for magnetite that is exsolved from the titanomagnetite. Thirty percent of the determined specimens are classified for min-type 2.

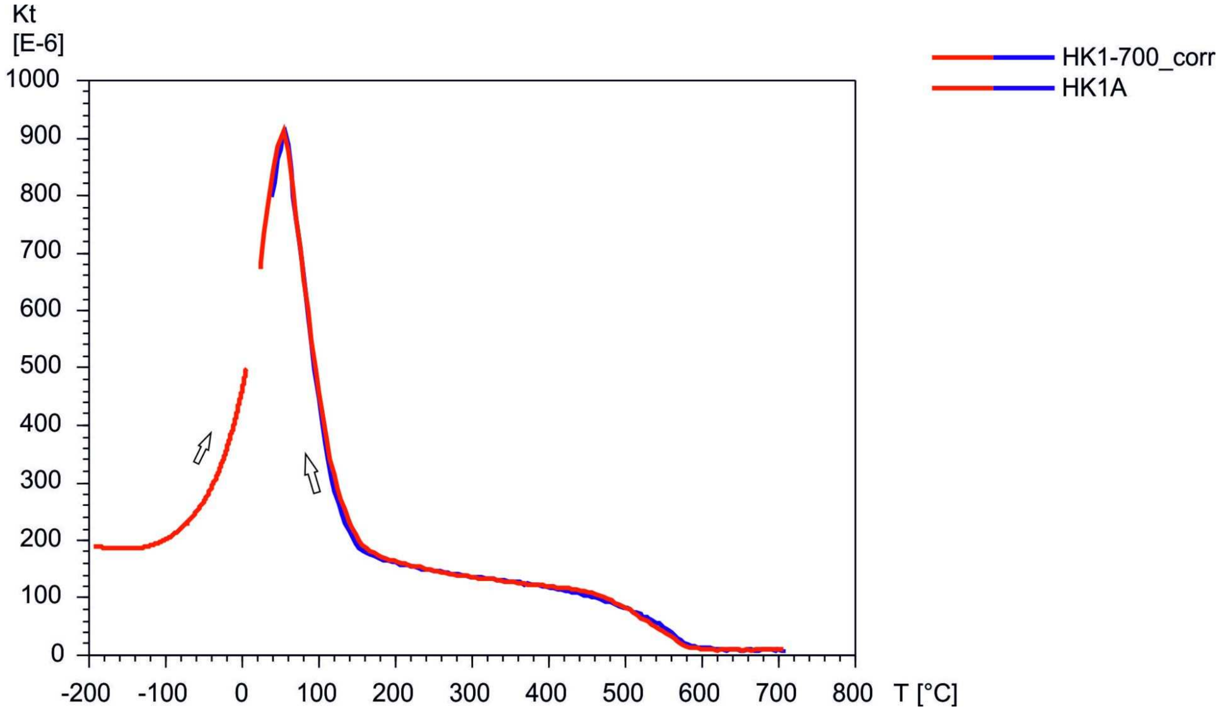

Figure 12: Characterization of min-type 2 by low and high temperature measurements of sample HK1.

Mineralogy type 3

Min-type 3 is characterized with an increase in susceptibility up to 200°C, followed by a steep decrease in sample HAH (Fig. 13) and a moderate decrease of susceptibility in sample SV. Both samples display an additional Curie point at 580°C.

Sample HAH, with min-type 3, shows a reverse heating and cooling curve up to a temperature of about 300-400°C. Above 400 °C the heating curve is non-reversible; the cooling curve shows the same shape as the heating curve. The magnetite can be determined at T_c 580°C. In addition another exsolved mineral phase is existent and observable between 200°C to 500°C. The other mineral phase displays a Curie temperature at 380°C and is said to be TM60. The significant change to lower susceptibility could be titanomaghemite that alterates to hematite. Due to the significant lower susceptibility, the cooling curve is below the heating curve. This transformation occurs due to a mineral phase that is sensitive to oxidation, but this mineral phase is not definable. The main content is magnetite or titan-rich magnetite. Only 20 % of the measured samples belong to min-type 3.

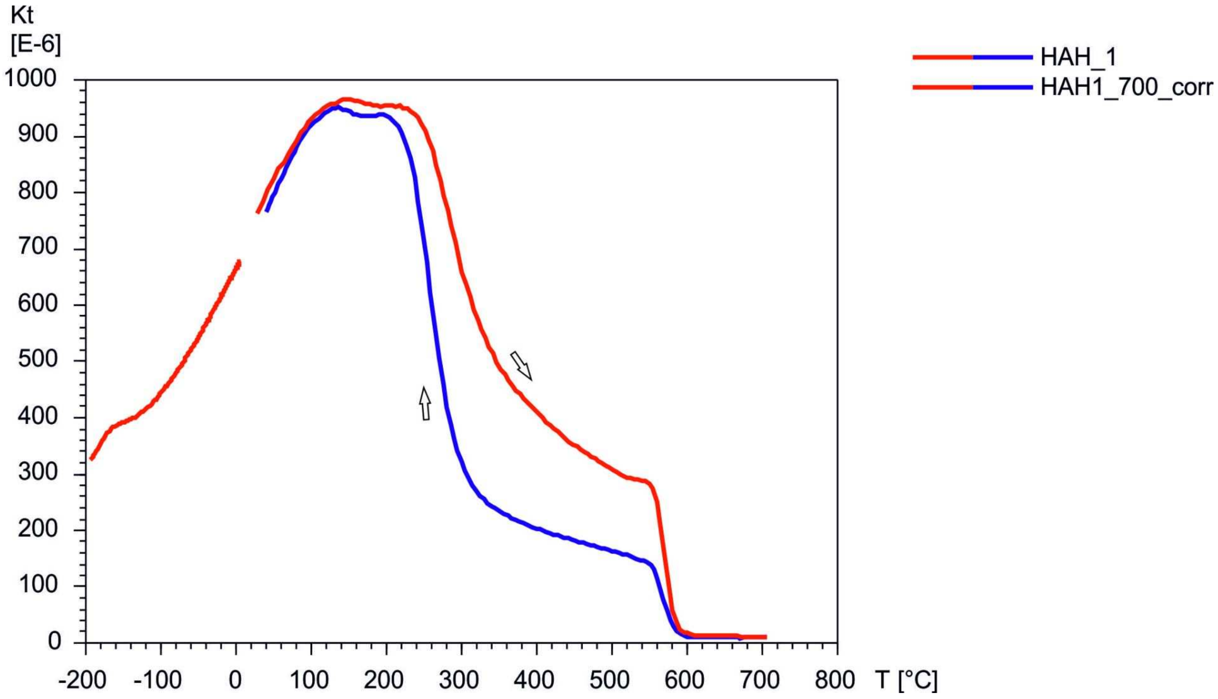

Figure 13: Low and high temperature measurements of HAH as an example for min-type3.

Mineralogy type 4

Sample BDH shows an increase of magnetic susceptibility up to a temperature of 400°C, a steep decrease of susceptibility above this temperature, and a non-reversible heating and cooling curve. A Verwey transition in the low-temperature measurement and the Curie point at 580°C are evidence for magnetite. The second mineral phase adverts to maghemite with a Curie temperature at 520°C. The deviation from low-temperature to high-temperature measurements can be explained by a mistake during calibration (see Appendix).

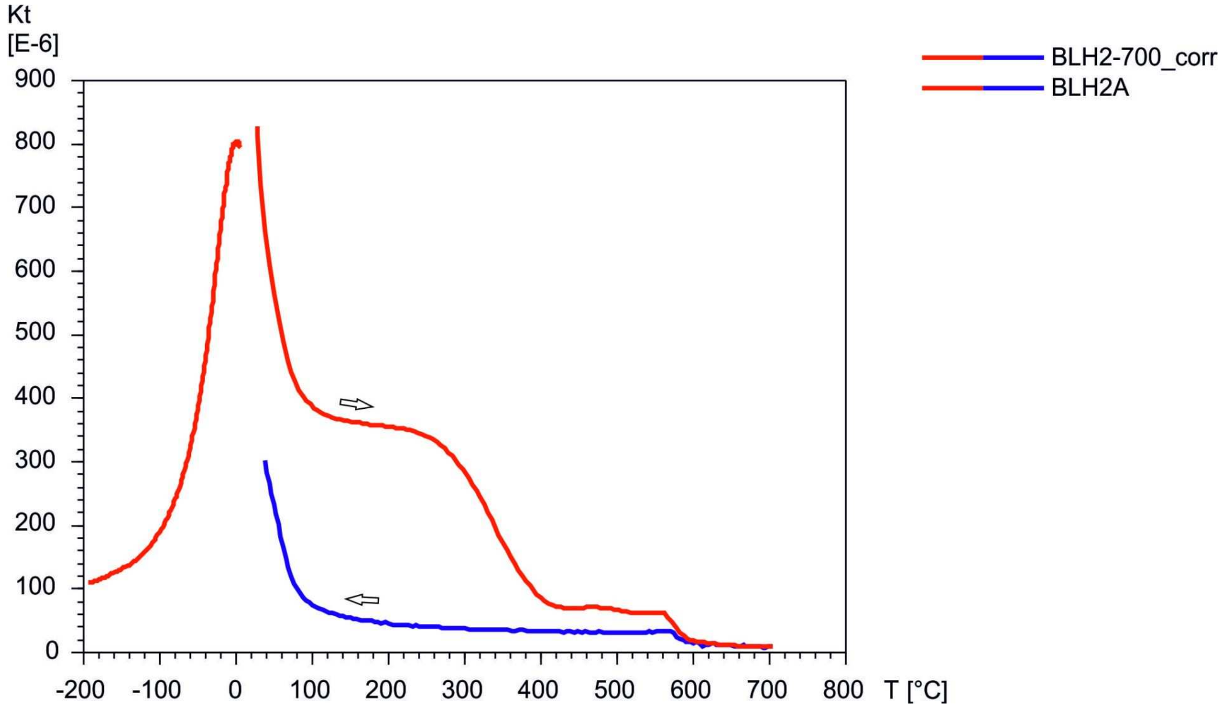

Figure 14: Sample BLH2 as an example for min-type 4, determined with low- and high-temperature measurements.

Sample BLH2 also represents min-type 4 (Fig. 14). Significant changes in the heating and cooling curve are evident. The Verwey transition in the low-temperature measurement and the Curie temperature at 580°C are characteristic for magnetite (Soffel, 1991). Titanomagnetite segregates in maghemite, ilmenite and hemoilmenite. The Curie temperature of hemoilmenites is below 0°C and turns out to be the reason for the difference in the measurements. The Curie temperature at 400°C is interpreted as maghemite. The exsolution of magnetite can result in maghemite. Due to the thermal instability of maghemite, the Curie temperature varies within a wide range due to the state of maghemization. A third mineral phase is observed with a Curie temperature at 80°C. This mineral phase displays thermal stability and remains during the heating cycles. It is interpreted as an exsoluted mineral phase from the original TM60. The irreversible heating and cooling curve indicates a mineral phase that no longer exists anymore after the heating and is interpreted as titanomaghemite. Twenty percent of the collected samples are classified for min-type 4.

4.1.2 The Anisotropy of Magnetic susceptibility (AMS)

The AMS measurements were conducted in the petrophysical laboratory of the University of Leoben. All measurements were conducted at room temperature.

The anisotropy of magnetic susceptibility was measured by the Kappabridge MFK1 from AGICO Geoscience Instruments (Fig. 15). This instrument is an extremely precise susceptibility measuring device with a sensitivity of $2*10^{-8}$ [SI]. The instrument includes a rotator system which enables automatic measurements in 64 directions (see Fig.16). The results can be plotted as susceptibility ellipsoids with k_1, k_2 and k_3, and additionally in a Flinn-plot, which displays oblate or prolate fabric in the values of lineation (k_1/k_2) and foliation (k_2/k_3). The confidence areas are in accordance with Jelinek's statistics (Jelinek, 1978, 1981).

The selected adjustments are:

Frequency	967 [Hz]
Field	200 [A/m]

Figure 15: Geofyzika MFK1-FA Kappabridge from AGICO (from AGICO MFK1-FA Kappabridge User's Guide).

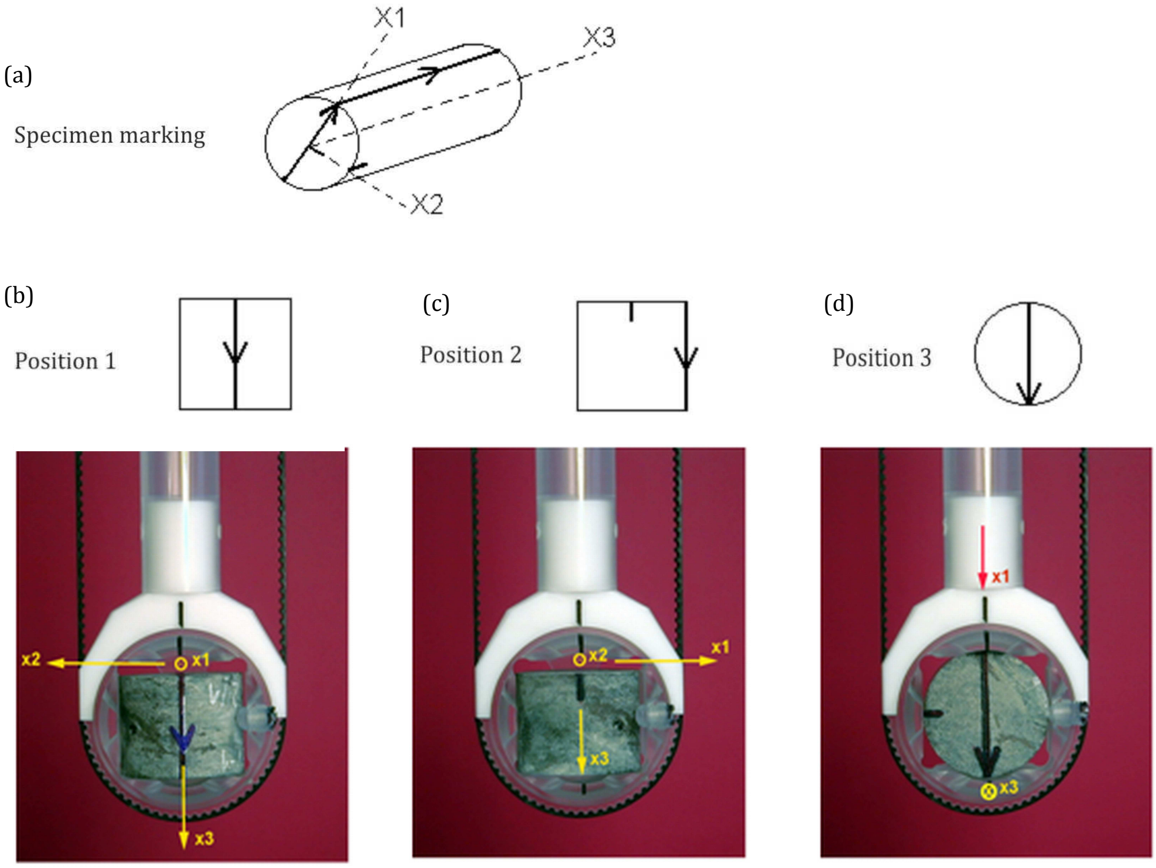

Figure 16: (a) shows the general marking for the specimen (b) shows the first position for AMS measurements for the Kappabridge. (c) displays the second position for AMS measurements, and (d) the third positions for the specimen for AMS measurements with the rotator system for MFK1-FA Kappabridge (pictures taken from AGICO Instruments, User manual).

Analysis of the Anisotropy of Magnetic Susceptibility

For the determination of the anisotropy measurements, a program Anisoft 4.2 from AGICO Geoscience Instruments was used. This program displays the susceptibility and the axes k_1, k_2 and k_3.

In order to interpret the anisotropy of magnetic susceptibility, various parameters have to be considered. The foliation describes the ratio $F=k_2/k_3$, the lineation is determined with $L=k_1/k_2$, and T is the so-called ‘shape parameter’, which helps to determine an oblate or prolate shape. A positive value of the shape factor T describes a prolate shape; hence a negative value describes an oblate shape. If this factor is around zero and the lineation and foliation are equal, the internal structure is triaxial. The factor P describes the degree of anisotropy by $P=k_1/k_3$. P_j (see Fig. 17) is defined as the corrected degree of anisotropy, and is calculated with a lognormal distribution. These parameters are based on Jelinek’s statistics (1978, 1981) and a minimum of five specimens is needed for the determination of all parameters that the Anisoft program provides.

$\eta_1=\ln(k_1)$ (equation 9)

$\eta_2=\ln(k_2)$ (equation 10)

$\eta_3=\ln(k_3)$ (equation 11)

$\eta_m=\sqrt[3]{\eta_1 \cdot \eta_2 \cdot \eta_3}$ (equation 12)

Shape parameter: $T = (2\eta_2 - \eta_1 - \eta_3) / (\eta_1 - \eta_3)$ (equation 13)

Degree of anisotropy: $P = k_1 / k_2$ (equation 14)

Corr. degree of anisotropy: $P_j= \sqrt[exp]{\{2[(\eta_1 - \eta_m)^2 + (\eta_2 - \eta_m)^2 + (\eta_3 - \eta_m)^2]\}}$

(equation 15)

Site BUH as an example for analyses of AMS:

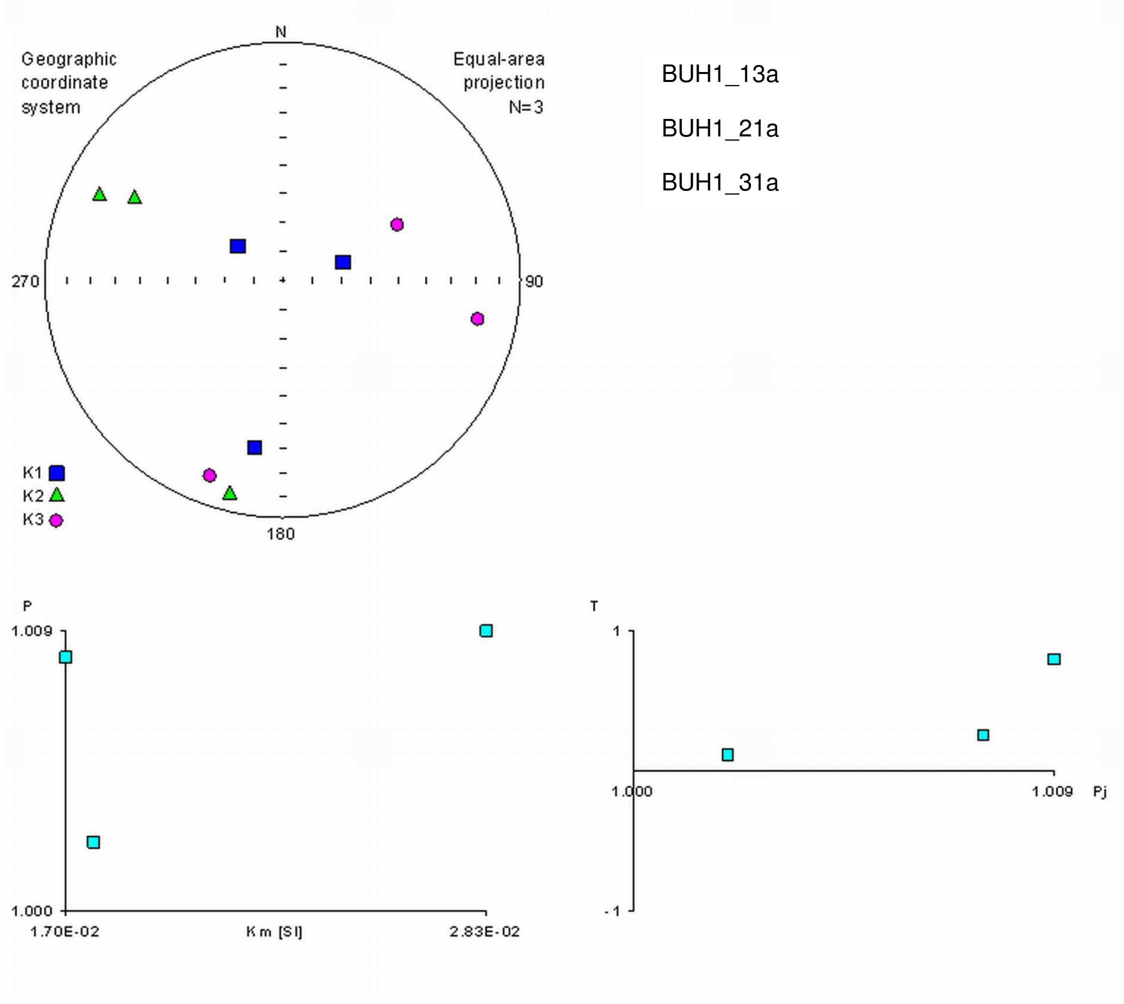

Figure 17: The figure displays the plotted anisotropy data of site BUH. The upper graphic shows the maximum (k_1), the intermediate (k_2) and the minimum principal axes. The two diagrams below display the P-parameter versus the mean susceptibility on the left and the shape parameter plotted against the corrected degree of anisotropy on the right-hand side.

Results of Anisotropy of Magnetic Susceptibility - AMS

The anisotropy of magnetic susceptibility is an indicator for verifications of processes during formation of the rocks and further mechanical deformations, new mineral formations or metamorphoses (Soffel, 1991). For the dating procedure, samples with almost no or very low anisotropy are necessary. Due to the minor anisotropy of magnetic susceptibility it is assumed that the anisotropy of remanence is also very low; hence, a correction of the anisotropy was neglected. The factor P, the degree of anisotropy, and P_j, the corrected factor of anisotropy, were consulted for an evaluation of anisotropy. A corrected factor of anisotropy in the range of 1.02, with a maximum of 1.08, was determined, which shows minor anisotropy and also leads to the conclusion that samples in this range are not faulted.

Beruvikurhraun - BEH

Samples from site BEH have a mean susceptibility between 8.55*10-3 [SI] and 1.23*10-2 [SI]. Two of the samples (Fig. 18a, b) display a low degree of anisotropy, P_j. The combined stereo-projection of samples BEH1 is plotted in Fig. 18(c). The scatter of the main axes is caused by the negligible anisotropy, thus the shape parameter, T, is not meaningful. Only BEH2-15 illustrates a higher degree of anisotropy (P_j: 39.6%), and reflects an exceptional case compared to the other samples of this site. The higher value for P_j in BEH-2 can be caused by deformation or block rotation that occurred only in the area of BEH-2 (Fig. 18f).

Samples of BEH1 and BEH2 differ in their anisotropy. The AMS of BEH2 is much higher (K_m 1.32E-02) than that of BEH1 ($K_{m:}$ BEH1_12a = 8.55E-03 and BEH1_23a = 9.21E-03). This effect is also reflected in the measured paleointensity, and gives reason to exclude BEH2 for further dating analyses. The higher anisotropies would make the dating analyses less accurate.

Budahraun - BDH

The specimen of BDH has a mean susceptibility of 8.23*10-3[SI]. The corrected degree of anisotropy, $P_{j,}$ displays a negligible anisotropy of 3% (Fig. 18e).

Blafeldarhraun - BLH

Samples from Blafeldarhraun show a very similar mean susceptibility with 1.75E-02 [SI] and 1.68E-02[SI]. Both samples of site BLH1 and BLH2 (Fig. 18d) illustrate values of P_j that range from 3.4 % to 0.9%.

Berserkjahraun - BSH

Samples from BSH show a mean susceptibility between 1.30E-02 [SI] and 1.51E-02[SI]. All samples display no significant anisotropy, thus the direction of the main axes is scattered.

Burstahraun – BUH

Specimens from site BUH have a mean susceptibility ranging from 1.70E-02[SI] to 2.83E-02[SI]. All samples are characterized by no significant anisotropy. The anisotropy factor, P_j, is between 0.2 and 0.9%, and the susceptibility fabric is not well defined (see Fig. 17).

Hellnahraun/Kalfatrađahraun - HK

The mean susceptibility of the samples is between 1.22E-02[SI] and 1.37E-02[SI] and displays a negligible degree of anisotropy between 5 and 8%.

Hnaushraun – HNH

Sample HNH1_12 has a mean susceptibility of 6.58E-02[SI] and a corrected degree of anisotropy of 2%. Hence, HNH1_23 displays a mean susceptibility of 3.77E-02[SI], and a value of P_j with 7.5%.

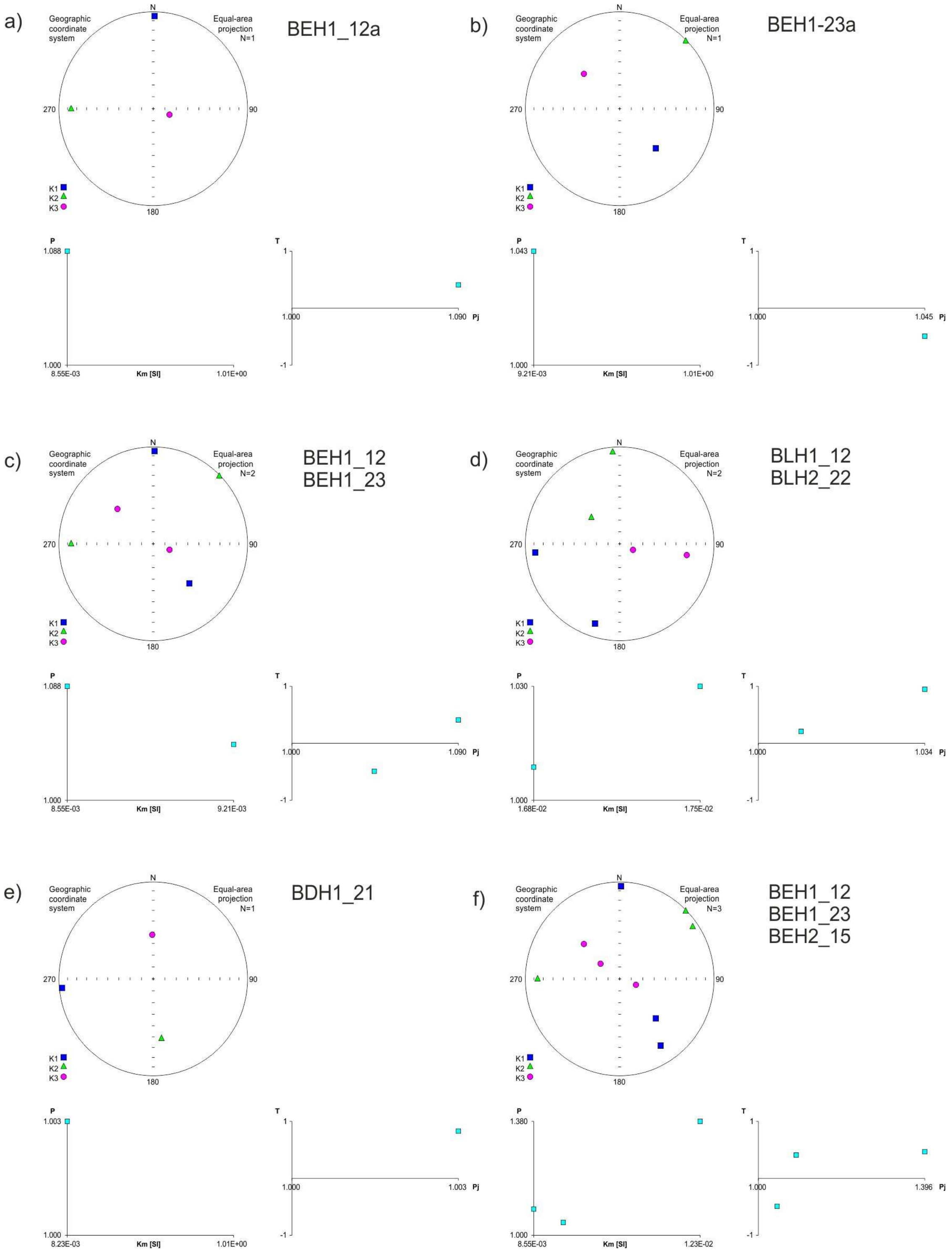

Figure 18: Stereoprojection of AMS data. The upper graphic shows the stereographic projection of the AMS ellipsoid: the maximum (k_1), the intermediate (k_2) and the minimum principal axes, respectively. The two lower diagrams display the P-parameter versus the mean susceptibility on the left and the shape parameter plotted against the corrected degree of anisotropy on the right-hand side. The figure displays (a) the plotted anisotropy data of site BEH1_1 and (b) the AMS data of site BEH1_2. The combined data of BEH1_1 and BEH1_2 are plotted in (c). (d) stereoprojection of site BLH1 and BLH2, (e) stereoprojection of site BDH1, and (f) plotted AMS data of site BEH reveal the difficulty of orientations due to block rotation of site BEH2.

Klifhraun – KLH

The means susceptibility ranges from 1.04E-02[SI] to 8.21E-03[SI]. Both samples show a degree of anisotropy with 0.7 and 0.8%.

Neshraun – NSH

The mean susceptibility ranges from 1.25E-02[SI] to 9.84E-03[SI]. The main axes of the reviewed samples are scattered; this is caused by their degree of anisotropy that ranges only from 1.5 to 0.7%.

4.1.3 Thermomagnetic Stability

Thermomagnetic stability describes the resistance of samples to magnetomineralogical changes during heating experiments. It is of importance for a quantification of possible alteration mechanisms that are not required for further Thellier experiments.

To analyze the thermomagnetic stability of the given samples, two complementary techniques were used: (1) ARM, measurements were carried out dependent on the heating step. (2) High temperature measurements were conducted in a stepwise manner with increasing maximum temperature.

4.1.3.1 Analysis of Thermomagnetic Stability by ARM Measurements

The magnetic susceptibility was measured in a low field after every thermal demagnetization step. Twenty-eight specimens were subjected to an AF demagnetization of an ARM (50 µT) before and after heating to 200C°, 400C°, 500C° and 600°C. These measurements allow a quantification of possible alteration mechanisms (Leonhardt et al., 2003). The measurements were conducted in Gams, in the paleomagnetic laboratory of the University of Leoben (Fig. 19).

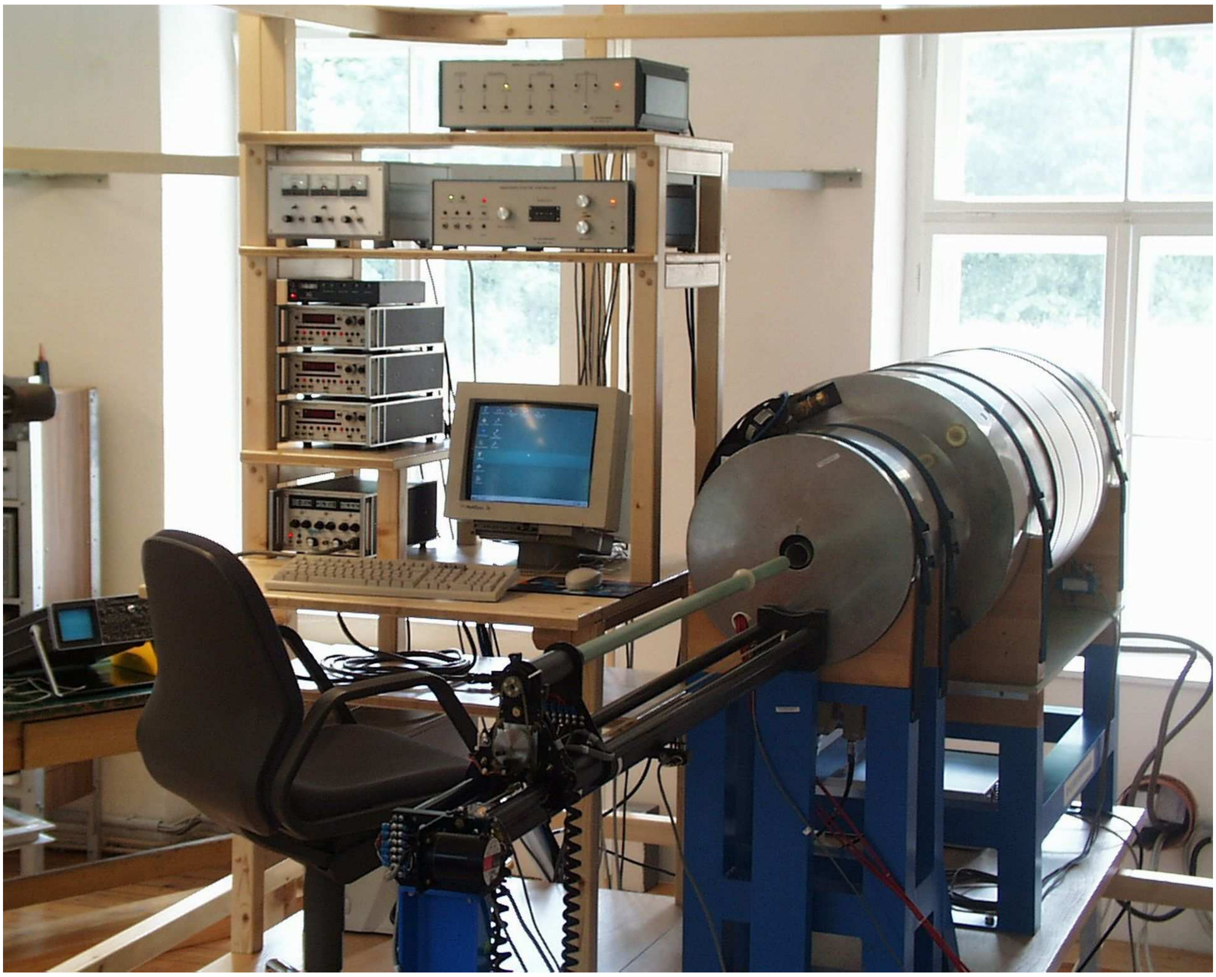

Figure 19: Cryogenic magnetometer in the laboratory in Gams.

The samples were heated and measured in several steps:

T0	room temperature	0 mT, 30 mT, 60 mT, 100 mT
T200	200°C	0 mT, 30 mT, 60 mT, 100 mT
T400	400°C	0 mT, 30 mT, 60 mT, 100 mT
T500	500°C	0 mT, 30 mT, 60 mT, 100 mT
T600	600°C	0 mT, 30 mT, 60 mT, 100 mT

A computer program, based on Mathematica (Wolfram Research) and written by Roman Leonhardt, was used for the analysis of the ARM measurements. The output of this program displays a diagram and the heating steps in several colors. The AF demagnetization of an ARM at room temperature is plotted against the AF demagnetization of an ARM after each heating step (Fig. 20).

PV1_11a

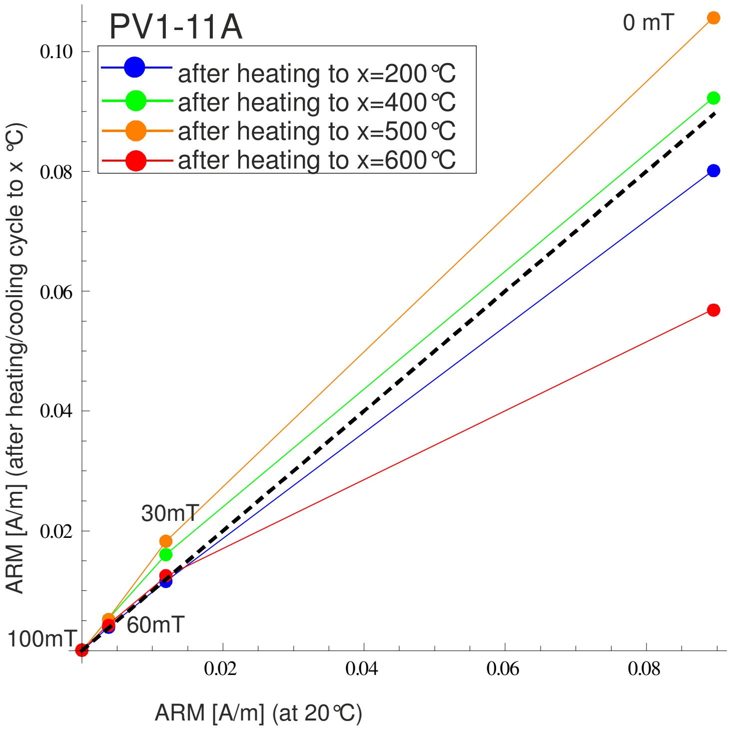

Figure 20: Sample PV1_11a as an example for ARM treatment.

Black dashed line: ideal line, with a slope of one

The AF demagnetization of an ARM at room temperature is plotted against the AF demagnetization of an ARM after each heating step. If the demagnetization steps linearly follow the ideal line, it can be determined that no alteration occurred. Samples that show no alterations during the ARM are related to alteration type one.

4.1.3.2 Incremental Susceptibility Measurements

These measurements were conducted within stepwise heating and an increasing maximum temperature. The heating cycles start with (a) maximum temperature 200°C (b) maximum temperature 400°C (c) maximum temperature 700°C.

(a) Samples BEH and HK show an almost perfect reversible heating and cooling curve up to a maximum temperature of 200°C. A Curie point at 150°C is interpreted as titanomagnetite (TM60). Sample BEH begins with a susceptibility of 230E-06[SI], which increases up to a temperature of about 50°C and decreases in susceptibility from this point on. HK starts with K_m of 610E-06[SI], increases up to 60°C and decreases from this point on. However, sample SV has an initial susceptibility of 85E-06[SI] and increases constant to maximum temperature. Sample HAH shows the same behavior as the susceptibility curve: It begins with 720E-06 [SI] and increases constantly up to a value of 920E-06 [SI]. Samples of site DRH and PV show increasing susceptibility up to a temperature of about 50°C and a steep decrease from this point on. The heating and cooling curves are reversible, respectively and display a T_c at 110°C. The susceptibility of sample DRH is 460E-06 [SI], yet PV shows a significantly higher susceptibility of 1850E-06 [SI]. Also sample HNH is characterized by increasing susceptibility up to 70°C. However, two Curie temperatures are identified at 130°C and 170°C. The mineral phase with T_c 170°C is identified as titanomagnetite (TM 60); the second mineral phase is most likely exsoluted from the original TM60. Measurements of sample SAH and BSH (K_m 240E-06 [SI]) display a constant increase of susceptibility up to a temperature of 90-100°C and increases from this temperature on. The graphs display T_c at 190°C and 170°C respectively, which are interpreted as titanomagnetite. Sample BUH (see Figure 21) shows at least two mineral phases. The first Curie point is determined at 90°C and reflects a mineral phase that exsoluted from the original TM60. The second phase starts with an increase of susceptibility to 200°C and is assumed to have a Curie point at the maximum temperature. Site BDH has an initial susceptibility of 215E-06[SI], and increases in susceptibility after a Curie temperature of 90°C. The heating and cooling curves are reversible. Samples BLH and KLH display reversible graphs and a Curie temperature of 90°C, which is interpreted as a mineral phase of magnetite. The susceptibility of KLH starts with an initial susceptibility of 330E-06 [SI] and ends with 200E-06 [SI] at 200°C. The initial susceptibility of BLH is 620E-06 [SI]. However, sample NSH reveals a susceptibility of 635E-06 [SI] and a Curie point of 150°C, and is taken as TM60. The heating and cooling curves differ slightly.

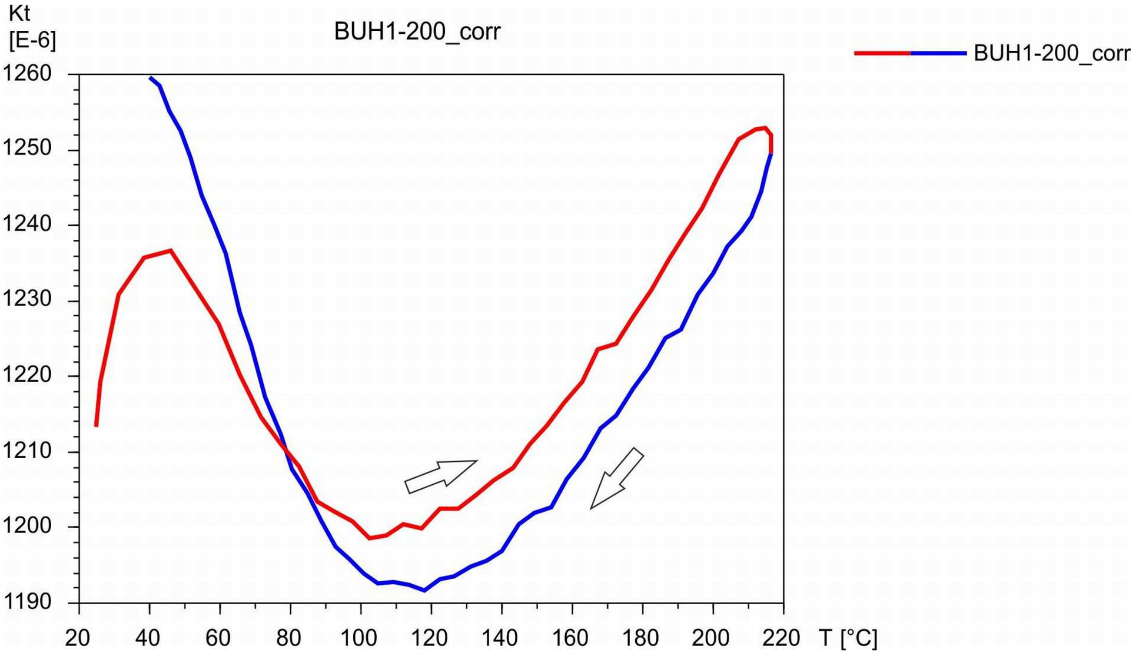

Figure 21: Susceptibility measurement of BUH up to a maximum temperature of 200°C.

(b) Samples BEH, BSH and HK do not show changes in susceptibility to the maximum temperature of 400°C. The heating and cooling curves remain reversible. The susceptibility of BSH increases slightly to 265E-06 [SI]. The samples of sites SV, PV and HAH show a constant decrease in susceptibility from 200°C to maximum temperature. The identification of a Curie point is not possible in this heating step. However, sample PV begins with increased K_m of 2100E-06 [SI] compared to heating step (a). HNH also increases slightly in susceptibility from 370E-06 to 440E-06 [SI]. Site DRH shows a second stable mineral phase with a T_c of 370°C and is assumed to be an exsolution mineral of TM60. The susceptibility remains at a value of 460E-06 [SI]. Sample SAH is characterized by a non identified mineral phase with T_c 260°C; the heating and cooling curve is reversible, but the initial susceptibility increases from 790E-06 [SI] in heating step (a) to 900E-06 [SI]. Sample NSH displays a slight increase in K_m to 660E-06 [SI], but this decreases from 50C° to 200°C and increases again to 370°C. A Curie point at 400°C is assumed, but not clearly definable. The heating and cooling curves of BLH differ significantly, thus the cooling curve shows higher susceptibility than the heating curve. Another mineral phase is identified at 390°C. Site BUH (see Figure 22) displays irreversible changes in the heating and cooling curve. The susceptibility increases to 300°C, remains stable to 400°C, and increases significantly during cooling. Sample KLH shows a T_c at 390 °C and remains with decreasing susceptibility up to the maximum temperature. BDH's susceptibility is 230E-06 [SI], then it decreases to a temperature of 100°C and increases significantly to 380°C.

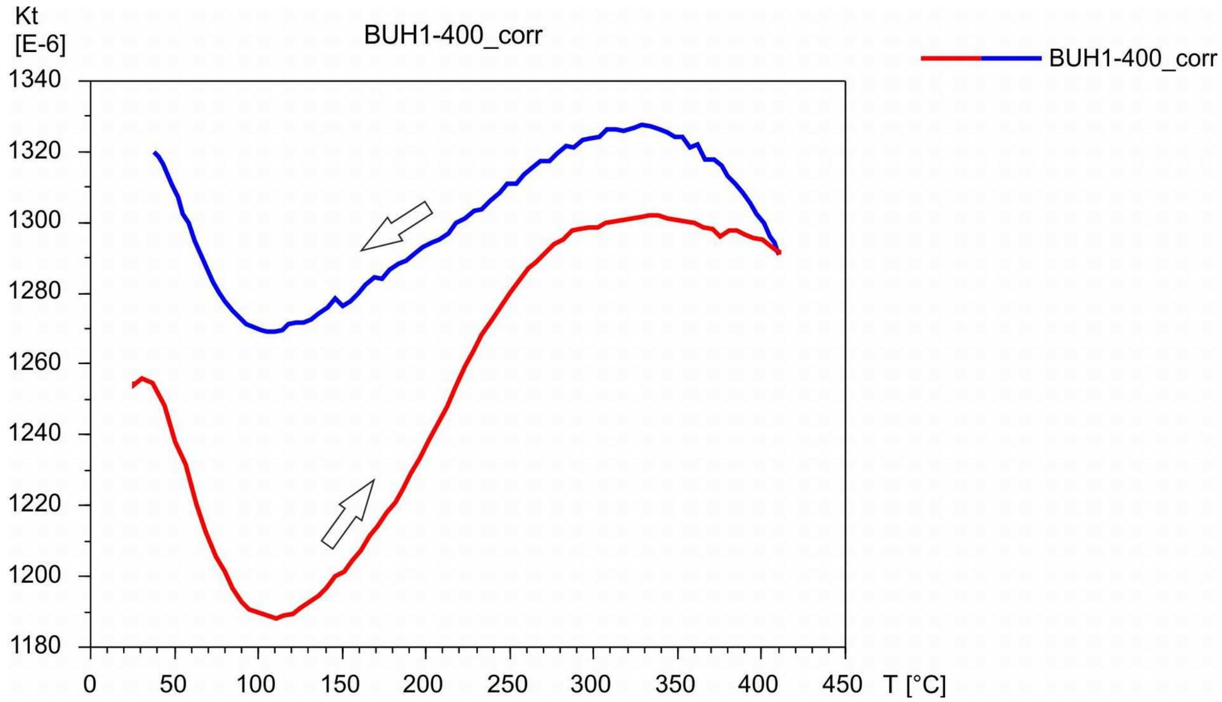

Figure 22: Susceptibility measurement of BUH to a maximum temperature of 400°C.

(c) The susceptibility of samples BEH and PV does not show changes to a maximum temperature of 700°C. The initial susceptibility of PV has increased in the previous heating steps and starts with 2200E-06 [SI] in the heating step to 700°C. Samples HK, HNH and SV display Curie temperatures of 580°C, which is characteristic for magnetite; however, the heating and cooling curves, respectively, are reversible. The susceptibility curve of sample HK begins and ends with 650E-06 [SI] and HNH shows an increased K_m of 480E-06 [SI]. In addition, sample DRH has a T_c at 580°C but the heating and cooling curves vary slightly. The susceptibility shows an increase to 500E-06 [SI] compared to the previous heating steps. In addition to a T_c of 580°C, other exsolution mineral phases at 350°C and 110°C are observed. These phases remain stable during heating and cooling, and are assumed as exsolution phases of TM60. Sample HAH displays the significant Curie point for magnetite at 580°C, while the heating and cooling curves drift in a range from 600°C to 150°C, but end at the same point and a susceptibility of 750E-06[SI]. Another exsolution mineral phase shows a Curie point at 400°C. Sample SAH shows the T_c for magnetite and another mineral phase that has its Curie point at 510°C. In addition, the heating and cooling curves vary below 580°C. Sample BUH (Fig. 23) is characterized by significant changes in the heating and cooling cycle. The cooling curve is irreversible below 600°C, and the value of susceptibility is also significantly lower than at the beginning of the heating curve. Another exsolution mineral is detected with T_c 600°C, but is not clearly definable. The heating and cooling curves of samples BSH, KLH, NSH and BDH also differ irreversibly below 600°C. Magnetite is identified at 580°C, and another mineral, resulting from maghemization, at a temperature of 540°C. The susceptibility differs significantly in sample NSH, thus K_m is 650E-06 [SI] at the beginning and 320E-06 [SI] after cooling. Sample BLH shows the same characteristic behavior as the samples mentioned before; hence, the Curie temperature at 400°C is identified as maghemite. In contrast to the second heating step (b), the cooling curve does not follow the heating curve and experienced a significant decrease of susceptibility. The heating curve of BLH starts with a K_m of 820E-06 [SI] and is irreversible in cooling below 580°C, and ending with 300E-06 [SI]. The mineral phase with T_c of 400°C no longer exists in cooling, just like in sample NSH. The susceptibility of sample KLH is increased to 400E-06 [SI], and displays T_c at 250°C, 520°C and 580°C. The cooling curve is irreversible and lower below 580°C, no longer reflects the mineral phase at 520°C, and increases again at 150°C.

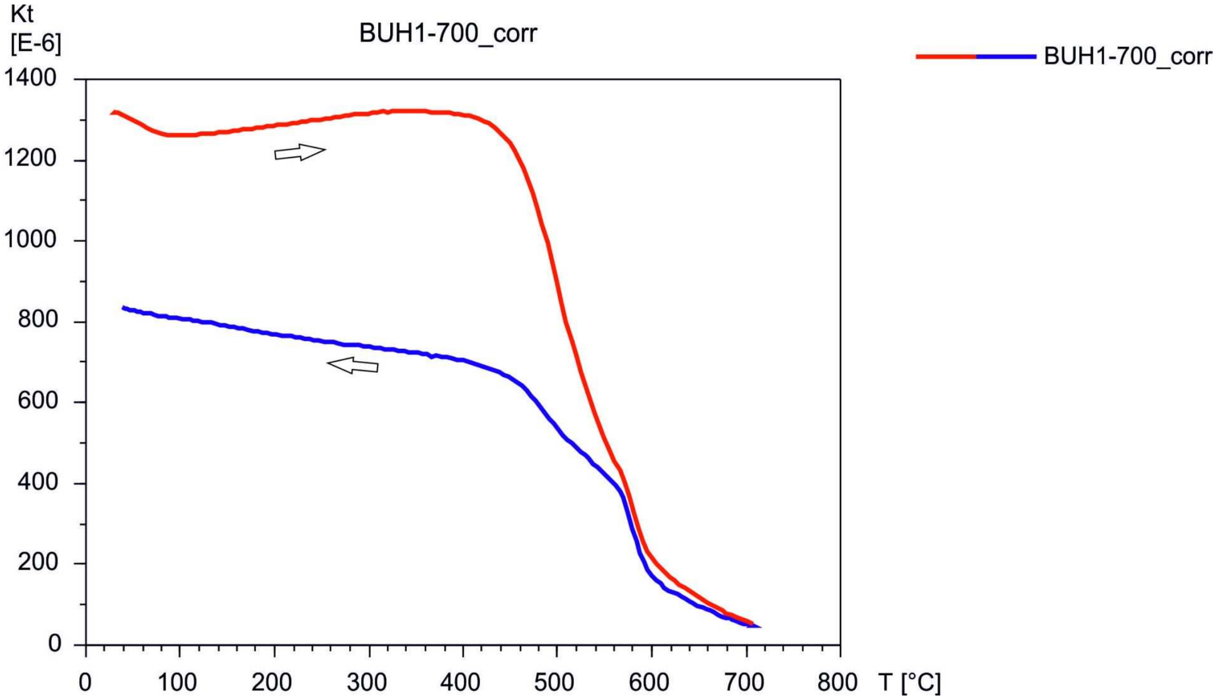

Figure 23: Susceptibility measurement of BUH up to a maximum temperature of 700°C.

4.1.3.3 Results of Thermomagnetic Stability

According to these measurements and results, the samples were separated into four different alteration types:

Alteration type 1: BEH, SV, HK
Alteration type 2: HNH, PV, DRH, HAH
Alteration type 3: SAH2, (BUH)
Alteration type 4: BDH, (BLH), (KLH), (NSH), (BSH)

Alteration type 1:

Samples from sites BEH, SV and HK are related to alteration type 1. If the ARM demagnetizations following the subsequent heating step are linearly related with a slope of one, this is an indicator for no alteration during the measurements. Samples of type 1, represented by sample BEH2_15a (Fig. 24a), are characterized by no alteration throughout the temperature range of the ARM experiments. Susceptibility heating and cooling cycles are reversible for all heating steps. 21% of the collection belongs to this group.

Alteration type 2

Samples of alteration type 2 indicate thermomagnetic stability below 400°C. Above 400°C they show changes in their behavior and stability. Due to the demagnetization steps, samples of alteration type 2 show a higher ARM, caused by the changing of less stable particles. The red line (600°C) differs from the black-dashed ideal line, hence it can be observed that at this point the total intensity is lower, and the fraction of more stable particles increases due to the decrease of the fraction of less stable particles. Thus, the grains change from multi-domain behavior to single-domain behavior with a higher content of stable particles. 28% of the samples belong to alteration type 2, which is represented from sample HNH1_23 (Fig. 24b).

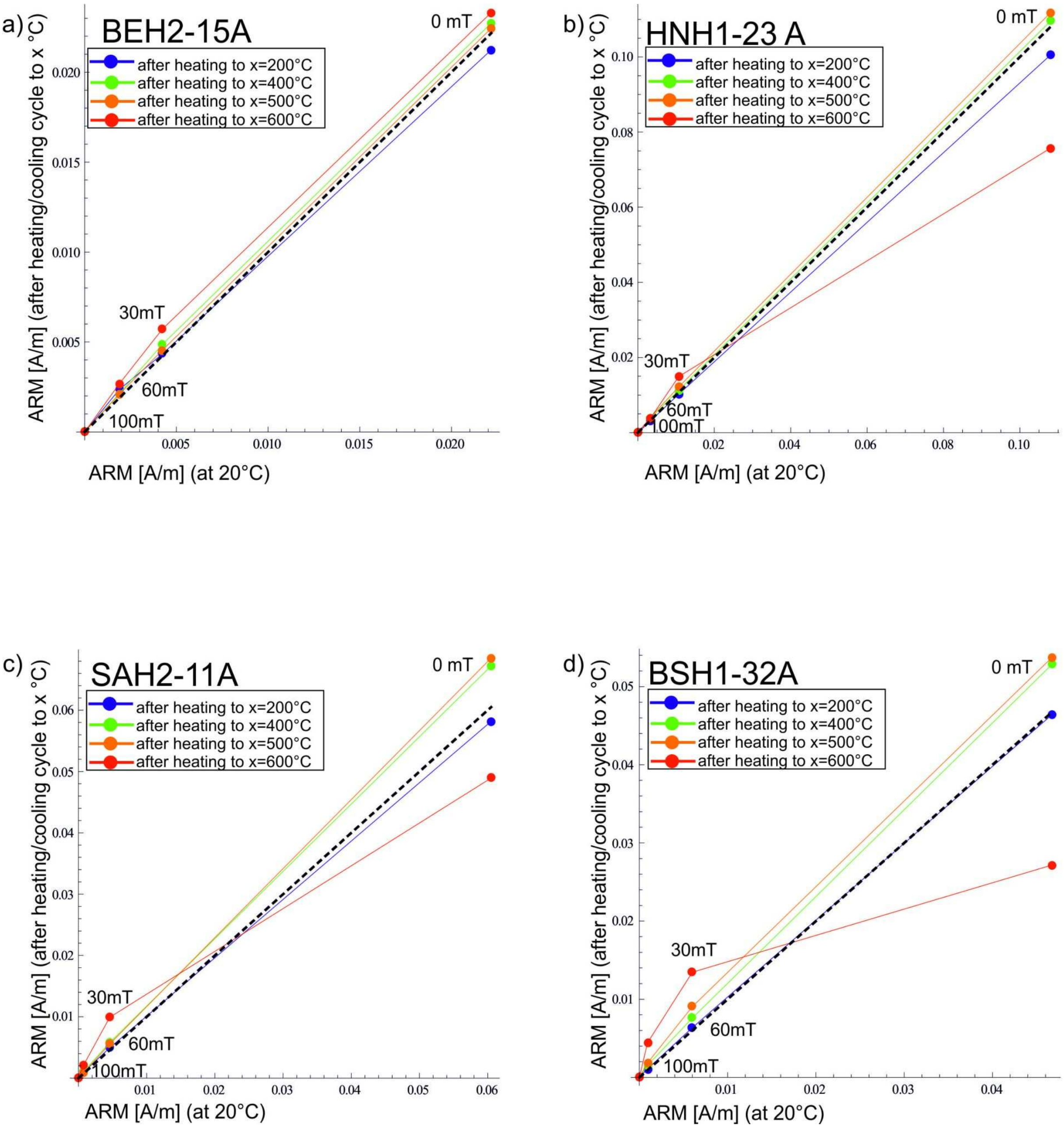

Figure 24: (a) ARM of sample BEH2_15a represents alteration type 1; (b) ARM of sample HNH1_23a, which is characteristic for alteration type 2; (c) shows the ARM of sample SAH2_11a, which represents alteration type 3; (d) ARM of sample BSH1_32a to characterize alteration type 4.

Alteration type 3

21 % of determined samples are identified as alteration type 3. Sample SAH2_11a (Fig. 24c) is representative for alteration type 3, which is characterized by an ideal alternating behavior up to 200°C. Above this temperature, a significant change in the thermomagnetic stability can be observed. From 200°C to 500°C, the proportion of low and higher stable particles increase. At 600°C (red line), the fraction of single-domain particles increases significantly, as does the fraction of low-coercivity particles.

Alteration type 4

Figure 24(d) shows a gradual alteration of sample BSH1_32a during the measurements above 200°C (blue line). At 400°C (green line), the genesis of remanence-bearing, low-coercivity particles and iron-oxides can be observed during heating, though the fraction of high-coercivity particles remains stable. It can be observed that at 500°C (orange line) the low-coercivity fraction is constant with the heating step before; these particles do not change during further treatment. However, the high-coercivity particles almost doubled; a phase separation of a stronger, high-coercivity fraction then occurs. With the further heating step, the content of high-coercivity particles remains with the same as at 500°C, but the decrease of lower-coercivity particles is significant. 28 % of collected samples belong to alteration type 4. Irreversible changes of the magnetic behavior at lower and higher temperatures can be detected (Kosterov and Prévot, 1998; Leonhardt et al., 2003).

The selection for further dating measurements and analyses was carried out according to mineralogy type and alteration behavior. Preference was gives to samples with mineralogy and alteration type one and two that display a very good thermal stability. Samples of alteration type 3 and alteration type 4 are not adequate for paleointensity determinations. Alteration at low temperatures, which could lead to incorrect paleointensity calculations, are usually not detected with standard checks during the Thellier experiment, as only a small percentage of the NRM is lost below 300°C. To compare the quality of the data, samples of mineralogy and alteration type three and four were additionally measured.

Summary

A pre-selection for the Thellier measurements was made from samples with minor changes in their thermomagnetic stability. Attention was given to samples that show perfect stability and reversibility at least up to 400°C in the high temperature measurements, and samples with a thermomagnetic stability of alteration type one and two.

ARM

Mineralogy

BEH1, 2

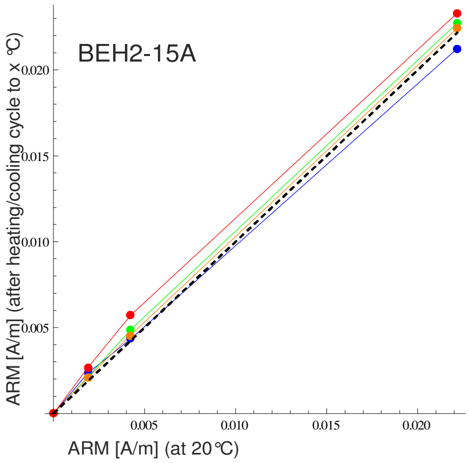

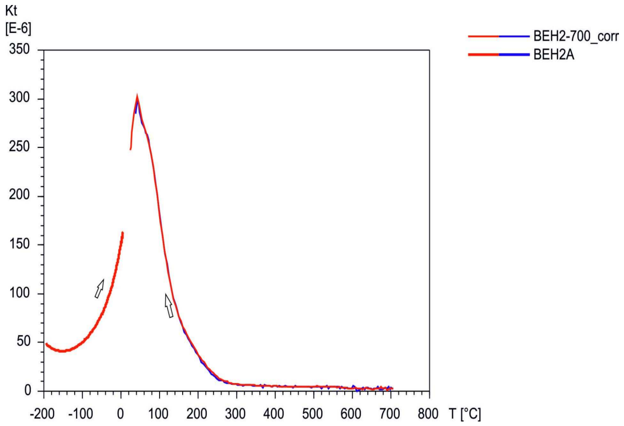

Alttype 1

Mintype1

HK1

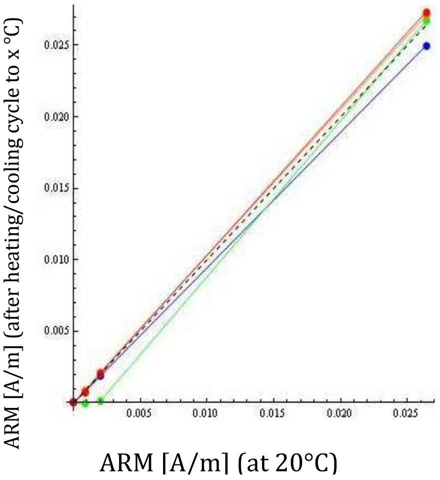

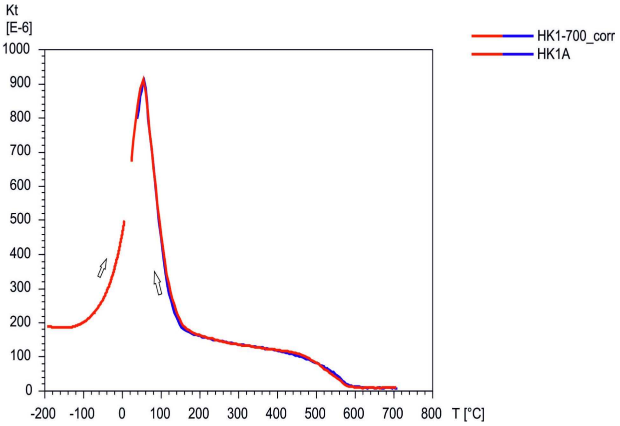

Alttype 1

Mintype 2

SV

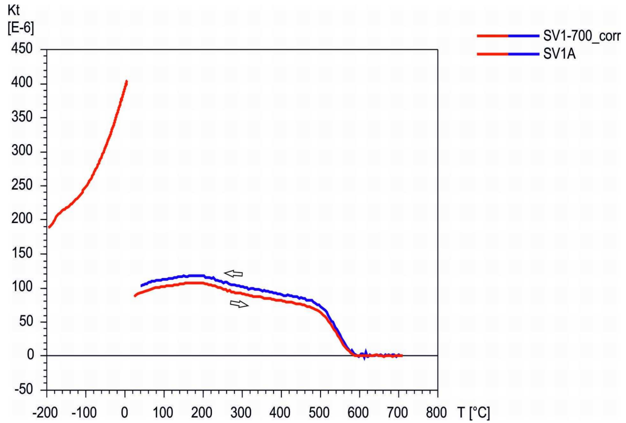

Mintype 2

HNH

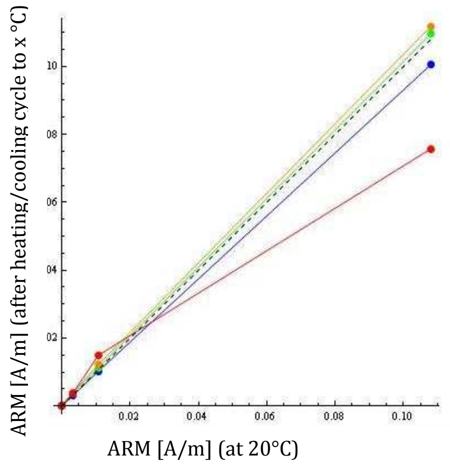

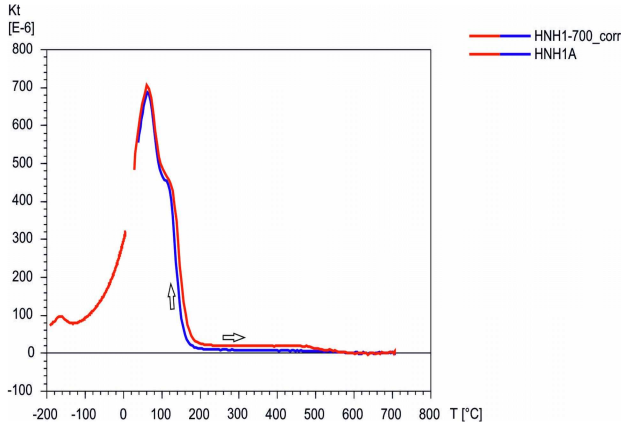

Alttype 2

Mintype 1or 2

PV

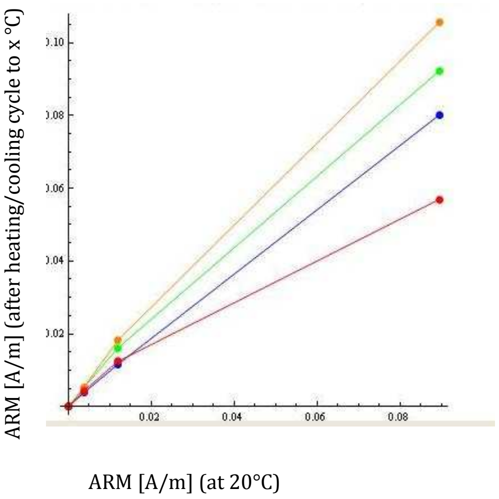

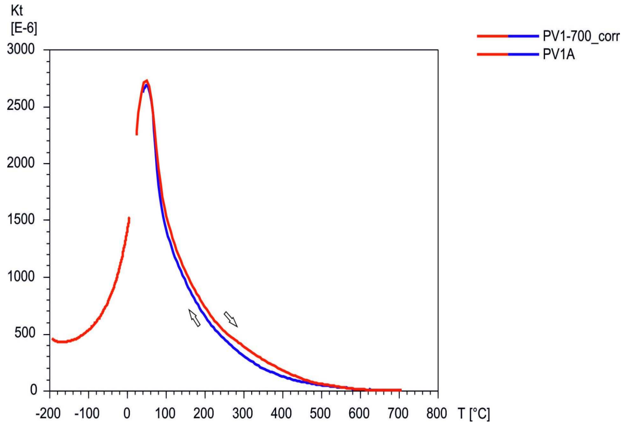

Alttype 2

Mintype 1

DRH

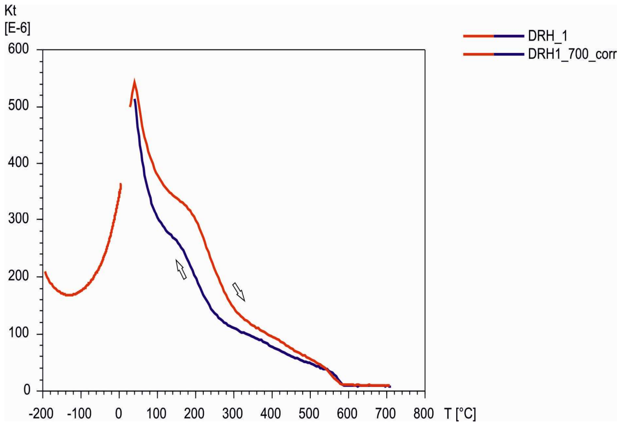

Mintype 2

HAH

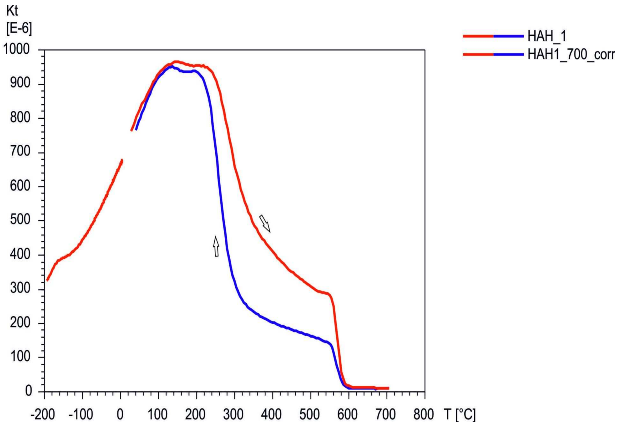

Mintype 3

SAH

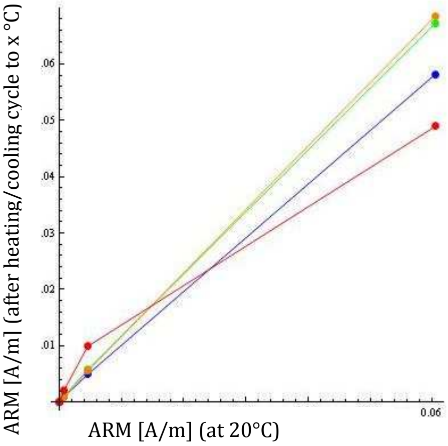

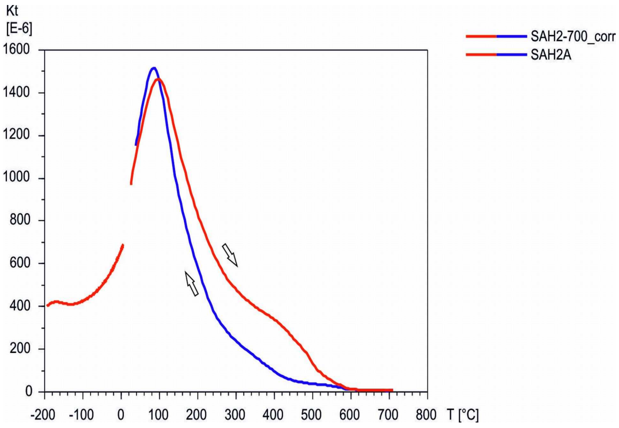

Alttype 3

Mintype 2

BDH

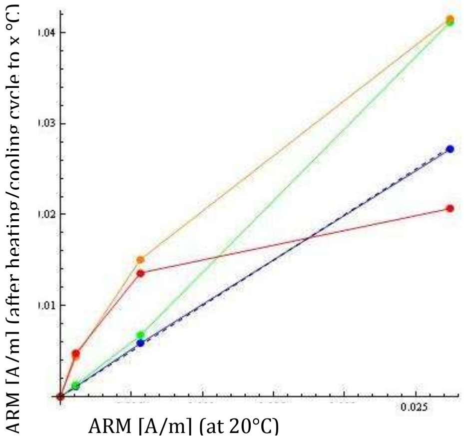

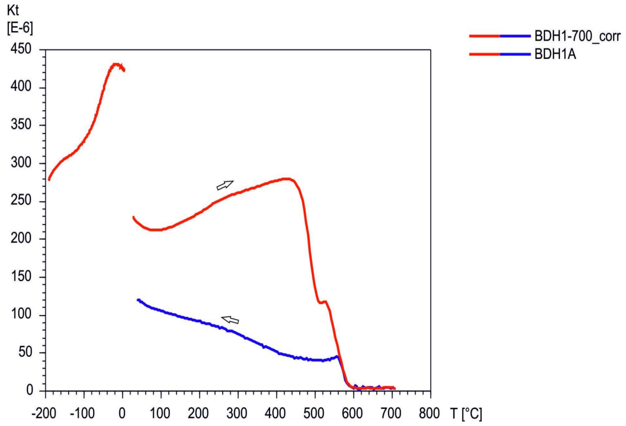

Alttype 4

Mintype 4

BLH

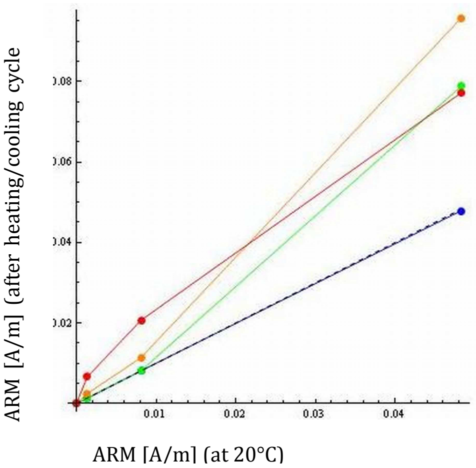

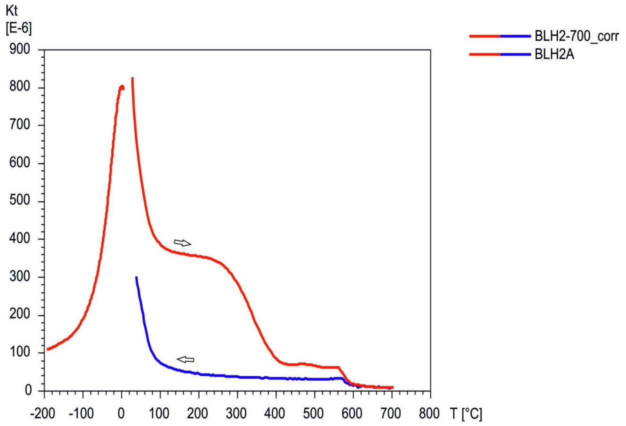

BSH

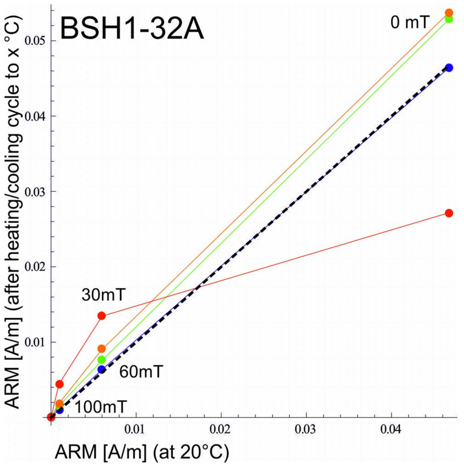

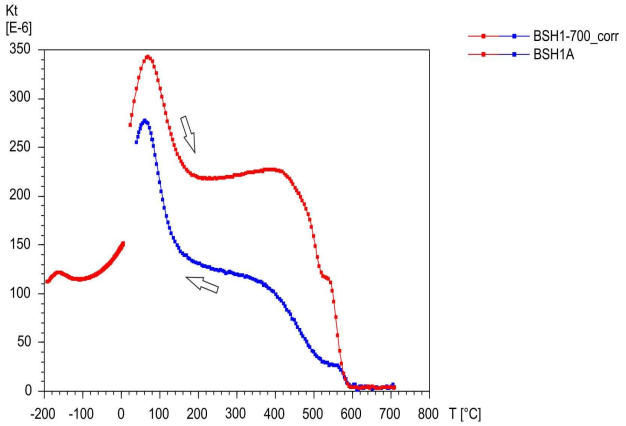

NSH

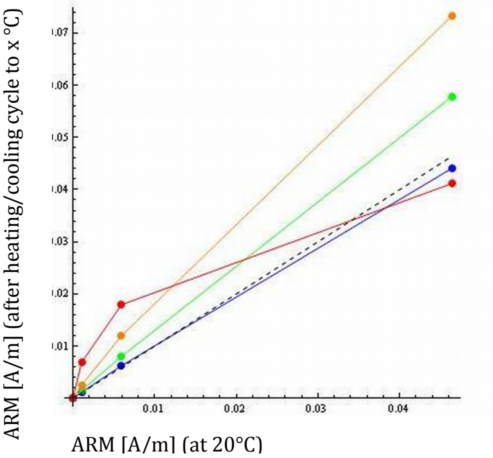
ARM [A/m] (after heating/cooling cycle to x °C)
.07
.06
.05
.04
.03
.02
.01
0.01
0.02
0.03
0.04
ARM [A/m] (at 20°C)

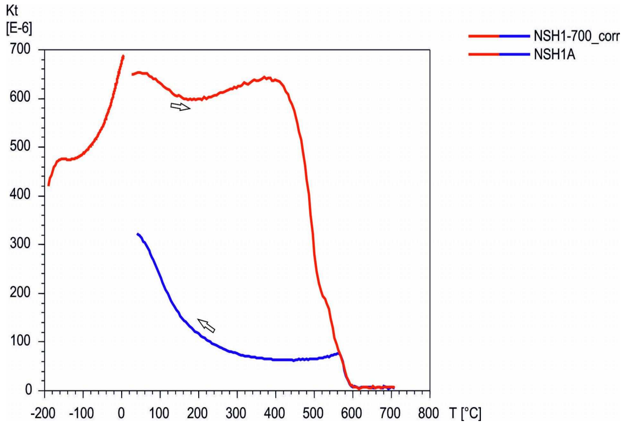
Kt
[E-6]
700
600
500
400
300
200
100
0
-200
-100
0
100
200
300
400
500
600
700
800
T [°C]
NSH1-700_corr
NSH1A

KLH

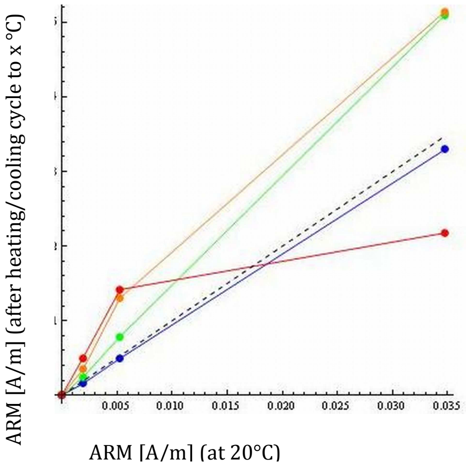
ARM [A/m] (after heating/cooling cycle to x °C)
0.005
0.010
0.015
0.020
0.025
0.030
0.035
ARM [A/m] (at 20°C)

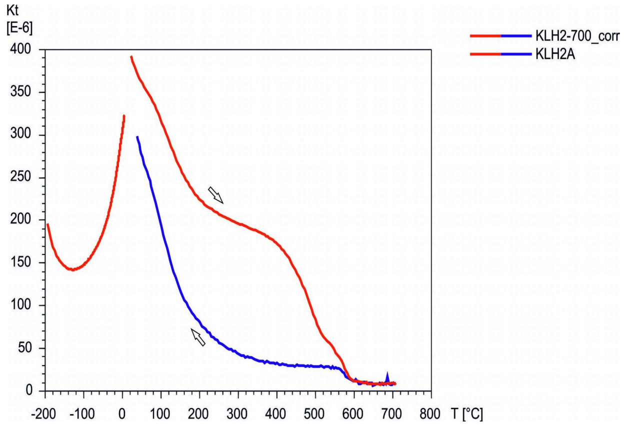
Kt
[E-6]
400
350
300
250
200
150
100
50
0
-200
-100
0
100
200
300
400
500
600
700
800
T [°C]
KLH2-700_corr
KLH2A

4.2 Paleodirections

For this determination, NRM measurements were conducted in the Paleomagnetic laboratory of the University of Leoben (Fig. 19), using the Cryogen Magnetometer 2G DC-SQUID. The Cryogenic magnetometer of 2G Enterprises was used for the measurements of the remanent magnetization. The DC-SQUID (Superconducting Quantum Interference Device) magnetometer consists of a superconductor Niobium and two Josephson junctions. These thin junctions divide the superconductor into two parts. For the superconduction, which needs a temperature of -269°C, the apparatus is surrounded by Helium. Putting the sample into the Cryogenic magnetometer causes a decrease in the electrical voltage and depends on the strength of the current, induced via Joseph Junctions, and also the compensating flux evident in the superconductor. The variation in the magnetic field caused by sample properties changes the current in the superconductor and thus the electrical voltage. To measure the variation of the Earth's magnetic field, a background magnetization was measured before every single measurement. Hence, the background can be compared to the variation due to the sample and conclude the magnetic field intensity of the given specimen (Schell, 2006).

A register of measured samples is given in the appendix, chapter 6. Data from ARM measurements and NRM measurements were analyzed with Remasoft 3.0 from AGICO Geoscience Instruments.

Twenty-eight specimens were treated by stepwise AF-demagnetization. The natural remanent magnetization was measured for 82 samples. A table of all measured samples is given in the appendix.

Analysis of Paleodirections

Remasoft 3.0 and the Principal Component Analysis PCA

The PCA analysis was used for the statistical determination of the mean directions of every lava flow. The appropriate software is Remasoft 3.0 from AGICO Instruments. The program provides the possibility to analyze demagnetization plots and the medium destructive field. In addition it provides plots in x-, y- and z-direction, a great circle plot and a function of group statistics to determine several samples from one site and calculate the mean direction for groups of samples. The orientation was inserted into Trend and Plunge and corrected for the local declination of 17° (NSH 18°).

The selected functions for the principal component analysis are the inclusion of the origin point and the anchoring of the linear to the last point. The PCA can be saved and appended to the data file as extension Cpca. This function is needed for further determination of the paleoflow mean direction. The medium destructive field was calculated by the program Remasoft 3.0. In general, the higher the value of MDF, the higher is the stability of the determined material.

The selected criteria for the determination were $k > 50$ and $\propto_{95} < 10$.

Examples for analyses with Remasoft 3.0: Sample BEH1_12 (Fig. 25 (a)) is characteristic for samples without superimposing and PV1_25a (Fig. 25(b)) characterizes samples with superimposing. Samples that show superimposing have to be corrected for the PCA.

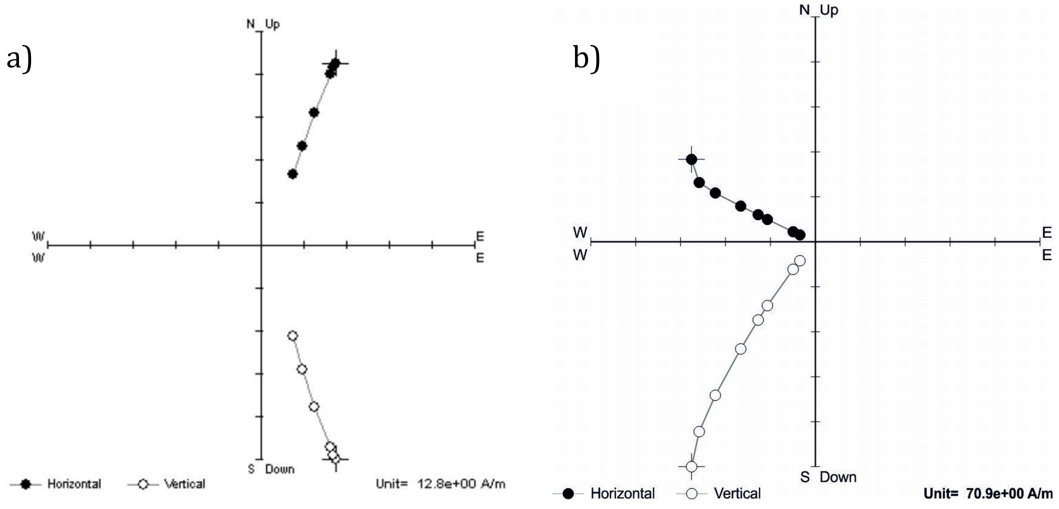

Figure 25: (a) Orthogonal projection of specimen BEH1_12a that characterized samples without superimposing and (b) sample PV1_25a is characteristic for samples with superimposing. Both samples are analyzed with Remasoft 3.0.

Results of Paleodirection and Mean Direction

The NRM was measured for 82 specimens (appendix, chapter 6) and 28 specimens were treated by stepwise AF-demagnetization.

The evaluation of measured data was conducted with Remasoft 3.0 from AGICO Geoscience Instruments. The program provides principal component analyses, demagnetization diagrams and the medium destructed field. The orientation has to be inserted into Trend and Plunge. In addition, a correction of the local declination of 17°, except for NSH with 18°, was carried out.

Remasoft 3.0 provides a statistical calculation to determine mean directions (Fisher statistic; Fisher, 1953) of measured samples. The PCA was performed for all samples and appended to the respective files. The function 'group statistics' allows all files to be opened from a site and the mean direction of all PCA's including statistical parameters α_{95} and k, as the best estimate of precision parameter, to be calculated (Remasoft, Usermanual).

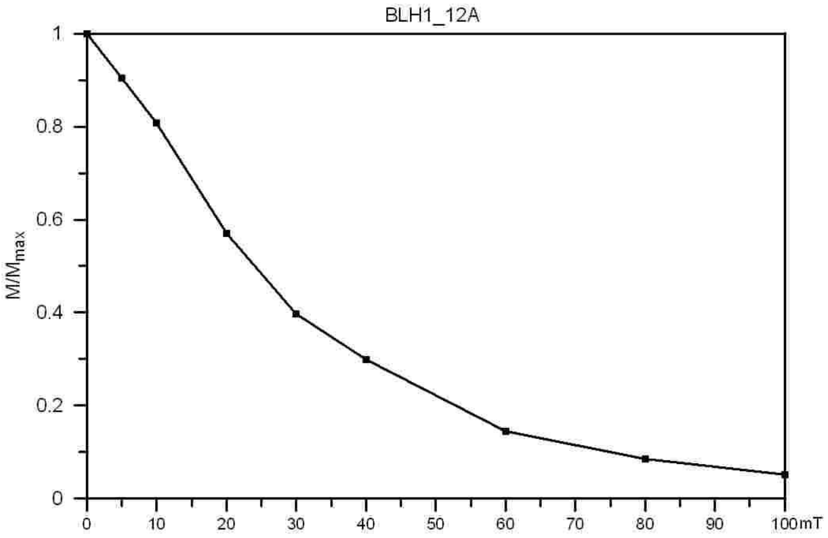

Figure 26: Demagnetization plot of sample BLH1_12a with Remasoft 3.0.

The medium destructive field (MDF) is the point which the alternating field reduces the NRM to 50%. The MDF is 24.1 mT for sample BLH1_12a (Fig. 26) that is characteristic for titanomagnetite. The MDF of sample BEH1_12a is 88.2 mT (Fig. 27) which is comparatively high. The reason for the high MDF-value can be explained due to a high-coercivity component that also shows a thermal stability e.g. hematite. Another reason for this MDF-value can be a high value of the anisotropy of magnetic susceptibility e.g. for magnetite. Indeed, sample BEH1_12a has a corrected value of magnetic anisotropy, P_j, of 9%.

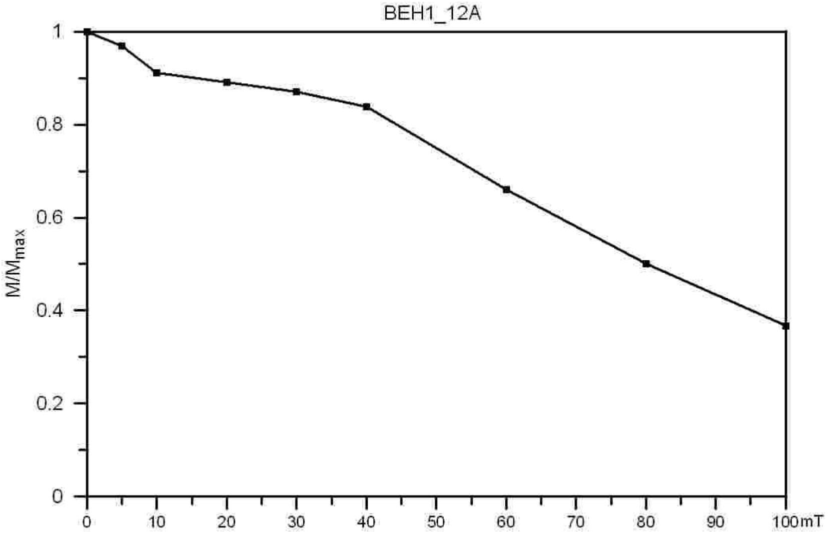

Figure 27: Demagnetization plot of BEH1_12a

Beruvikurhraun - BEH

The analyses of samples of site BEH do not show a superimposing. Samples of BEH1_1 (Fig. 28b) and BEH1_2 are characterized by a respective satisfying consistence in directions. The combination of BEH1_1 and BEH1_2 (see Fig. 29a, 29b 29c) also correlate in terms of orientation, which is expected for Iceland. The orientation results are 65.5° inclination and 18.9° declination with k of 87.75 and α_{95} of 5.6°. All samples of site BEH1 were accepted for further analysis. Whereas site BEH2_1 (Fig. 29f) is characterized by a declination of 310.4° and an inclination of 6.3°, k is 173.18 and α_{95} is 4.6°. The values of BEH2 compared to BEH1 lead to significant changes and inconsistency in orientation. The deviations can be caused by a block rotation that only occurred in site BEH2 and not BEH1. According to these data, a separation within site BEH is indispensable.

Berserkjahraun - BSH

Site BSH is also characterized by significant changes in orientation between BSH1_1,-1_2 compared to BSH1_3. BSH1_1 and also BSH1_3 are marked by a small overprint that is considered in the principal component analysis. The data of BSH1_1 and BSH1_2 show good conformity and the results of the group statistics are: 62.4° inclination and 45.7° declination ($k= 7.91$ and $\alpha_{95} = 6.2°$). The mean direction of site BSH1_3 differs with an inclination of 6.0° and declination of 176.1° ($k= 179.45$ and $\alpha_{95} = 5.7°$).

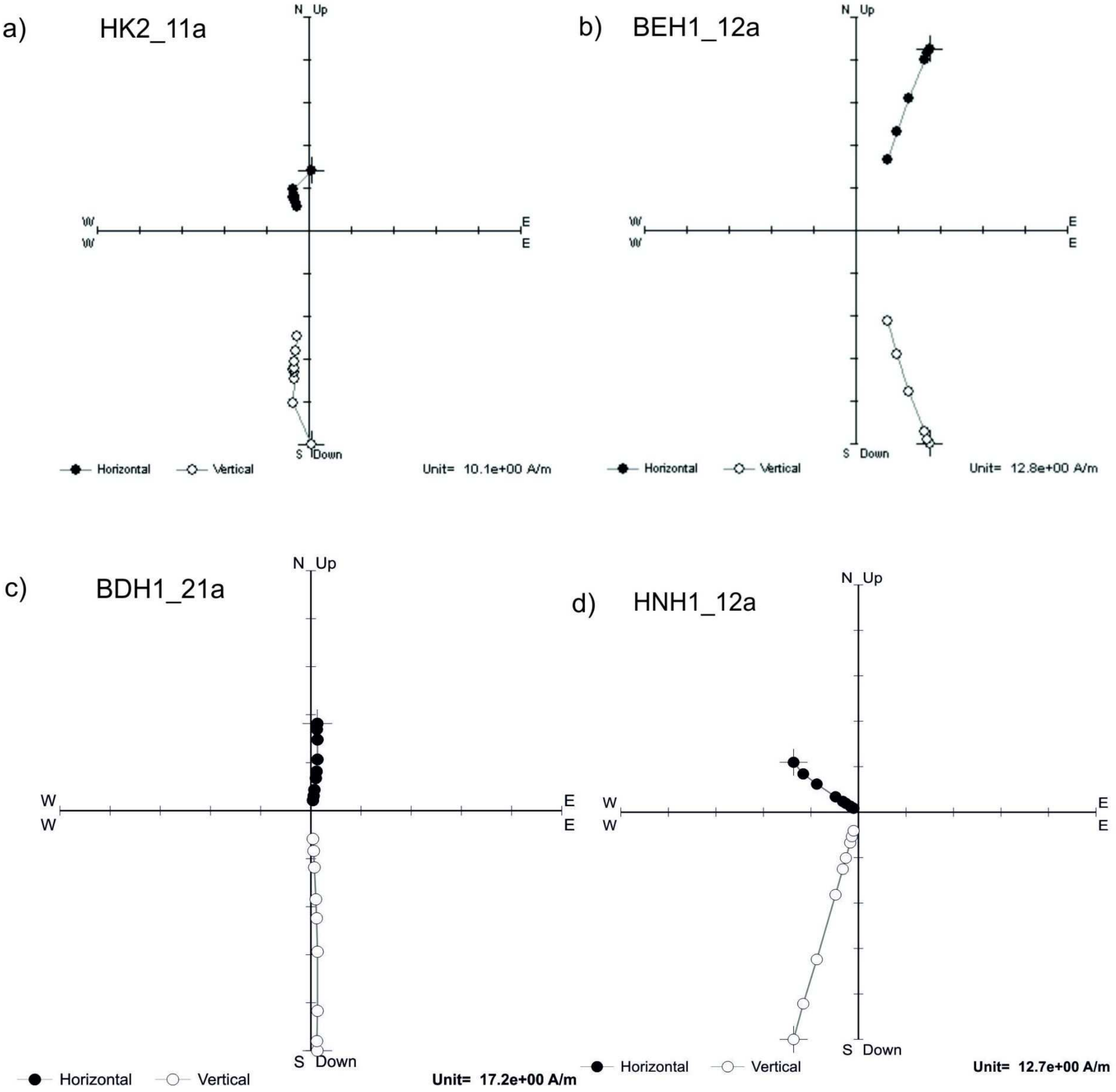

Figure 28: Results of paleodirectional analyses (a) orthogonal projection of sample HK2_11a, which displays superimposing. (b) Sample BEH1_12a shows no superimposing. (c) Sample BDH1_21a is also characterized by no superimposing and (d) orthogonal projection of sample HNH1_12a. All samples were analyzed with Remasoft 3.0.

Hnaushraun - HNH

Measured samples of site HNH are characterized by a good consistency in direction. The specimens are also marked by the absence of superimposing (Fig. 28d). The group statistic of HNH shows an inclination of 69.6° and a declination of 298.0° with k of 290.97 and α_{95} of 4.5°.

Prestahraun/Væjuhraun - PV

Samples of site PV are characterized by a superimposing. Figure 25 (b) displays the overprint compared to BEH1_12 (Fig. 28(b)), which has to be considered in the principal component analysis. Inconsistency in orientation can be observed, where PV1_1 shows an inclination of 82.6° and a declination of 157.5°; PV1_2 has an inclination of 52.2° and a declination of 305.1°, and PV1_3 displays an inclination of 71.4° and a declination of 9.6°. Reasons for these deviations could be block rotations or failures in orientation during the drilling of the inch cores.

Hellnahraun/Kalfatrađahraun - HK

Figure 28(a) shows the orthogonal projection in z-direction of sample HK2_11a, which Remasoft 3.0 provides. Sample HK2_11a is marked by an overprint that has to be considered for the principal component analysis. Except for two specimens, HK1_11 and HK1_21, the site shows a very good consistency in orientation. The group statistic of site HK is calculated with 69.7° inclination and 356.7° declination; k is 140.28 and α_{95} is 5.7°.

Sandarhraun - SAH

Samples of site SAH are also marked by significant superimposing. The medium destructive field varies from 54.2 mT in site SAH1_1 and 68.9 mT in site SAH1_2 to 15.1 mT in site SAH2_1. Thus, the orientation in group statistic is inconsistent where SAH1_1 and SAH1_2 show an inclination of -39.7° and a declination of 250.2° (k= 27.31, α_{95} = 17.9°), while SAH_2 has an inclination of 83.7° and a declination of 172.7° (k = 834.52, α_{95} = 8.7°).

Budahraun – BDH

Analyses from site BDH (see Fig. 28c) show a gradual demagnetization for BDH1-21a. The medium destructive field is low with 26.3 mT. Due to the overprint, the PCA range is selected from 10 mT to 100 mT with geo-declination of 6.7°, geo-inclination of 70.1°, and M of 76.1[A/m]. The maximum angular deviation is 0.6°. The NRM was measured for specimen BDH2-11a. For further group statistics, a PCA was also determined for BDH2-11a with geo-declination 313.5°, geo-inclination 82.3° and M of 43.75 [A/m] (Fig. 28 c). The results of the group statistics are 77.3° inclination and 352.4° declination (see Fig. 29e).

Blafeldarhraun - BLH

The group statistics of site BLH1_1 are homogenous and display an inclination of 65.3° and declination of 42.1° (k= 278.13, α_{95} = 4.0°) (Fig. 29d). Hence, BLH2_2 has an inclination of 74.0° and declination of 151.2°.

Burstahraun - BUH

The group statistic results of BUH leads to a separation of BUH1_1 from BUH1_2 and BUH1_3. Sample BUH1_13 presents an overprint and a medium destructive field of 27.6 mT. The mean direction of site BUH1_1 is 15.5° inclination and 139.8° declination with k of 233.62 and α_{95} of 3.4°. Specimen BUH1_21 is also characterized by an overprint and displays a medium destructive field of 24.9 mT; this is the same as specimen BUH1_31, which shows a MDF of 19.3 mT. The mean direction of the combination of BUH1_2 and BUH1_3 shows an inclination of 70.9° and declination of 351.3° (k= 308 and α_{95} = 7.0°). Specimen BUH1_32a was disregarded due to an assumed fault during the measurements.

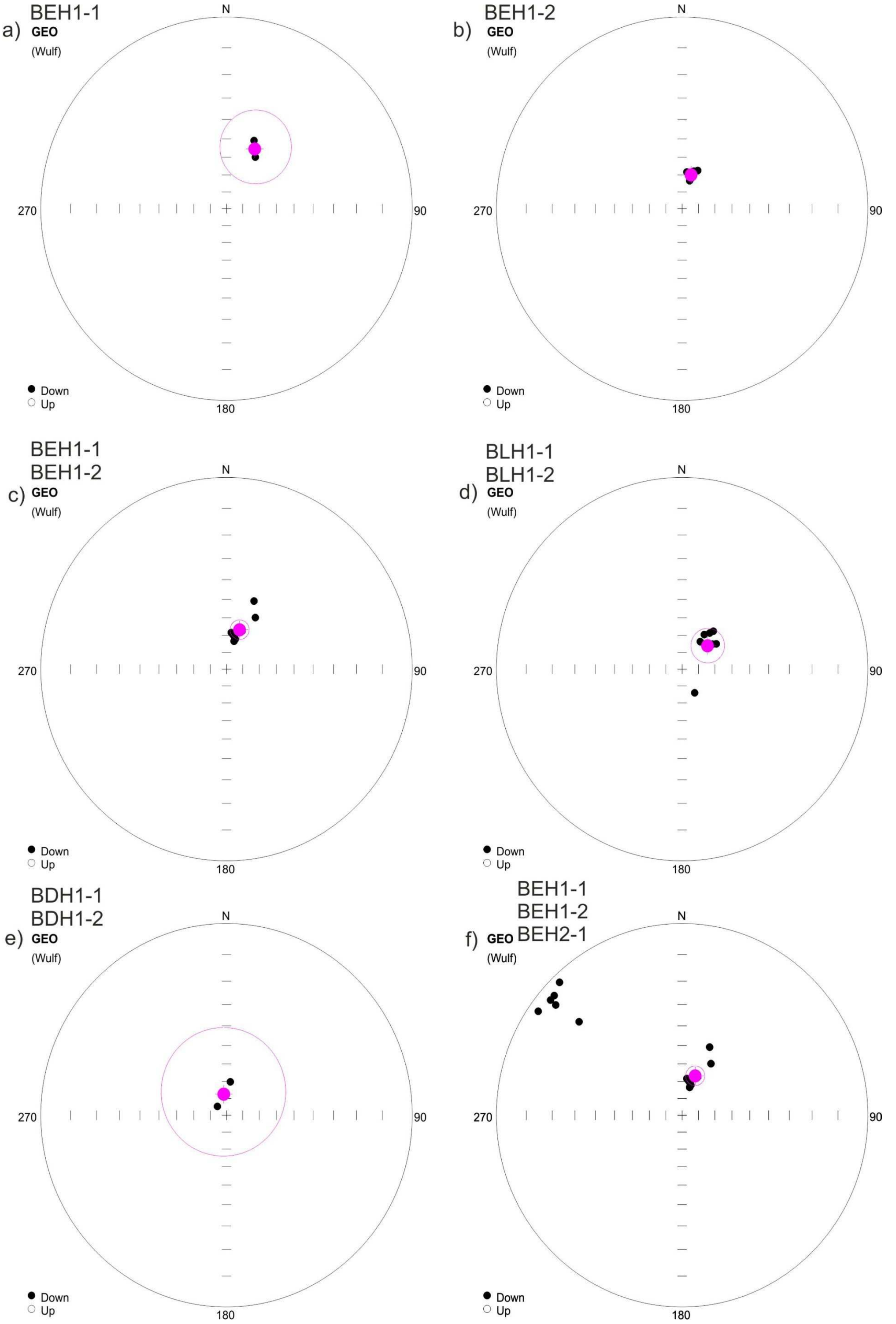

Figure 29: (a) group statistic results of site BEH1_1, calculated with Remasoft 3.0. The mean directions of BEH1-1 flow are 26.0° declination and 51.8° inclination; k is 167.15 and α_{95} is 19.4°. (b) displays the group statistic of BEH1_2 with 69.3° inclination and 15.3° declination; k is 665.97 and α_{95} is 2.3°. (c) shows the combination of BEH1_1 and BEH1_2 with 65.5° inclination, 18.9° declination, k of 87.75 and α_{95} of 5.6°. (d) mean direction of site BLH 1_1with: Dec 42.1°, Inc 65.3°, k: 278.13, α_{95}: 4.0° and BLH1_2: 74.0° inclination, 151.2° declination (e) mean direction of site BDH, which shows an inclination of 77.3° and declination of 352.4° (f) shows the orientation of the whole site BEH and indicates the significant deviation between BEH1 and BEH2 due to a block rotation of BEH2.

Neshraun - NSH

Measured samples of site NSH show a medium destructive field that ranges from 31.2 mT to 26.5 mT. The group statistics shows a mean direction of 74.1° inclination and 347.8° declination with k of 16.46 and α_{95} of 9.1°.

Klifhraun - KLH

Samples of site KLH are characterized by a medium destructive field ranging from 27.5 mT to 25.8 mT. Specimen KLH1_11 varies from other samples and is disregarded because of an assumed mistake during measurement. The main direction of KLH is 77.2° inclination, 27.3° declination with k of 95.97 and α_{95} 6.2°.

Paleodirectional results from Snaefellsjökull

Site	***Site lat (°)***	***Site long (°)***	***n/N***	***Declination (°)***	***Inclination (°)***	***k***	***α_{95} (°)***
BDH	64.82615	336.60411	2/2	352.4	77.3	48.68	36.6
BEH	64.75925	336.11789	9/16	18.9	65.5	85.75	5.6
BLH	64.83649	336.73669	6/7	42.1	65.3	278.13	4
BSH	64.94895	337.01876	8/14	45.7	62.4	80.56	6.2
BUH	64.81317	336.03704	3/14	351.3	70.9	308.08	7
DRH	64.73328	336.19683					
HAH	64.74484	336.26271					
HK	64.76333	336.31895	6/8	356.7	69.7	140.28	5.7
HNH	64.8075	336.38448	5/8	298	69.6	290.97	4.5
KLH	64.78084	336.35609	7/8	27.3	77.2	95.97	6.2
NSH	64.86348	335.96253	17/17	347.8	74.1	16.46	9.1
PV	64.83916	336.14121	10/13	320.4	62.9	19.34	11.3
SAH	64.91297	336.11423	0/6				

Table 3: Accepted paleodirection results from Snæfellsjökull. The longitude and latitude coordinates, determined by GPS, are given in the first columns. The mean inclinations and declinations of the sites are presented, as well as the precision parameter k and α 95 for directional site groups. Column (n/N) denotes the number of samples treated (N) versus the number of samples used (n) for calculating the site mean direction.

4.3 Paleointensities

The Cryogenic magnetometer of 2G Enterprises, in the laboratory of Gams (Fig. 19), University of Leoben, was used for the paleointensity measurements of selected specimens. For the determination of the intensities of the paleomagnetic earth field several procedures are known. The Thellier method (Thellier and Thellier, 1959) and several modifications (Coe, 1967a) of this measurement are the most common procedure. For this thesis, a modified Thellier method according to Leonhardt et al. (2004) was conducted.

4.3.1 Thellier-Experiments

The Thellier method (Thellier and Thellier, 1959) and later modifications are the most commonly used paleointensity determination techniques. The procedure used in this study is based on modifications of Coe (1967a, 1967b) and Leonhardt et al., (2004). It consists of stepwise demagnetization of NRM under zero-field conditions and stepwise partial thermoremanent magnetization under in-field conditions with the same temperature. The partial thermoremanent magnetism that is used for the Thellier experiments is not a classical pTRM. The so-called pTRMa or pTRM* is different, as the samples gain the partial thermoremanent magnetization to defined heating steps. During the Thellier-type measurements, the pTRM* is gained by heating the specimen to a heating step (T_i) and applying a field (H_{lab}) while it is cooled to room temperature (T_0). The results of pTRM and pTRM* can differ for samples that contain MD particles (Shcherbakov et al., 1993 and Shcherbakova et al., 2000), which can lead to incorrect results of paleointensity (Fabian, 2001; Leonhardt et al., 2004). Another reason can be chemical alteration during the heating and cooling cycles (Perrin, 1998; Goguitchaichvili et al., 1999) (see chapter 2, Fundamentals). Different checks suggest the determination of magnetomineralogical changes and the presence of biasing MD effects. The pTRM checks (Coe, 1976a), conducted to $T_k<T_i$ in a H_{lab} after demagnetization to T_i (in-field check), or zero-field checks conducted after previous pTRM* acquisition to $T_{i,}$ reveal the alteration processes (Leonhardt et al., 2004). Two different methods evaluate the influence of MD remanences in order to obtain better paleointensity information. (a) pTRM*-tail checks: repeated demagnetization to T_i after previous pTRM* acquisition to $T_{i,}$ which tests the independence of different pTRM*s (Leonhardt el al., 2004; Riisager and Riisager, 2001). (b) Additivity checks: outrange of the law of additivity of pTRM*s (Krása et al., 2003), which is essentially the same as the zero-field alteration check. A comparison of in-field and zero-field checks indicates feasible failures of Thellier's law of additivity (Leonhardt et al., 2004) (see Fig.30).

The differences between the applied field and the NRM of the pTRM*-tail check are considered based on Leonhardt et al. (2004b). The pTRM* checks were measured under in-field conditions during heating and cooling; the applied field intensity in the laboratory was 65 mT ± 0.5 mT.

For Thellier measurements, samples were heated in defined heating and demagnetizations steps:

1. Demagnetization: Sample is demagnetized in zero field to T1.
2. pTRM acquisition: pTRM is acquired while heating and cooling in field H_{lab} to T1.
3. Demagnetization: Sample is demagnetized in zero field to T2.
4. Alteration check (every second heating step): pTRM is acquired while heating and cooling in field H_{lab} to T1.

5. pTRM acquisition: pTRM is acquired while heating and cooling in field H_{lab} to T1.
6. Additivity check: Sample is demagnetized in zero field to T1.
7. Tail check: Sample is again demagnetized in zero field to T2.
8. Measurement steps are repeated up to T_c

For the experiments conducted, the following nomenclature was defined.

Type:		**Code:**
Zero-field:	TH – Thermal demagnetization	same as temperature
	AC – Additivity check	-3
	TL –	-4
In-field:	PT – Partial thermal demagnetization	-1
	CK – pTRM*-check	-2

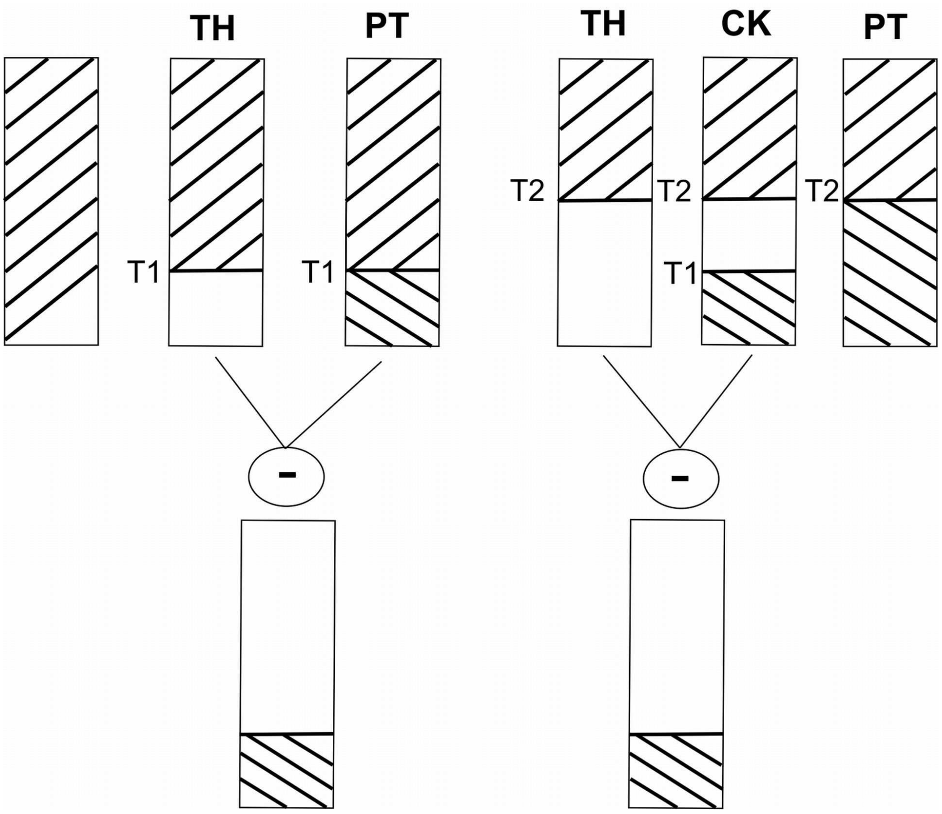

Figure 30: Main overview of the modified Thellier method, according to Leonhardt (2004).

Analysis of Thellier Measurements

Thellier Tool4.22

The first processing step was carried out with Thellier Tool4.22, written by Roman Leonhardt (2005-2009). The program provides analyses of the Thellier experiments and their modifications. The Thellier Tool shows an Arai (Arai, 1963) plot, which displays the NRM/TRM and provides the possibility to plot additivity checks and to display the plot in x, y and z-direction, or just in z-direction. The decay diagram plots the intensity during demagnetization, and also in addition the orthogonal projection of demagnetization is given by a Zijderveld (Zijderveld, 1967) diagram. The input window gives the possibility to select and vary the temperature range for the calculation of the linear fit. The results are divided into three classes, starting with class A for the best quality, to class C if class A or B do not match (see Table 4). The criteria for class A and B are defined with:

Linear fit criteria	Class A	Class B
Number of points (N):	= 5	≥ 5
Standard deviation (Std):	≥ 0.1	≥ 0.15
Fraction of NRM (f):	≥ 0.5	≥ 0.3
Quality factor (q):	≥ 5	≥ 0
Directional criteria		
MAD (anchored):	≤6	≤ 15
MAD’ (not-anchored):	≤999	≤ 999
Alpha:	≤15	≤ 15
Alteration criteria		
Relative check error (d(CK)):	≤999	≤ 999
Cumulative check diff (d(pal)):	≤5	≤ 10
Difference ratio (Drat):	≤7	≤ 10
Repeated demagnetization steps		
Normalized tail of pTRM (d(t*)):	≤3	≤ 99
Relative intensity diff:	≤10	≤ 15
Additivity checks		
Relative AC error (d(AC)):	≤5	≤ 10

Table 4: Criteria classes A and B for analysis with Thellier Tool.

Results of Analyses with Thellier Tool

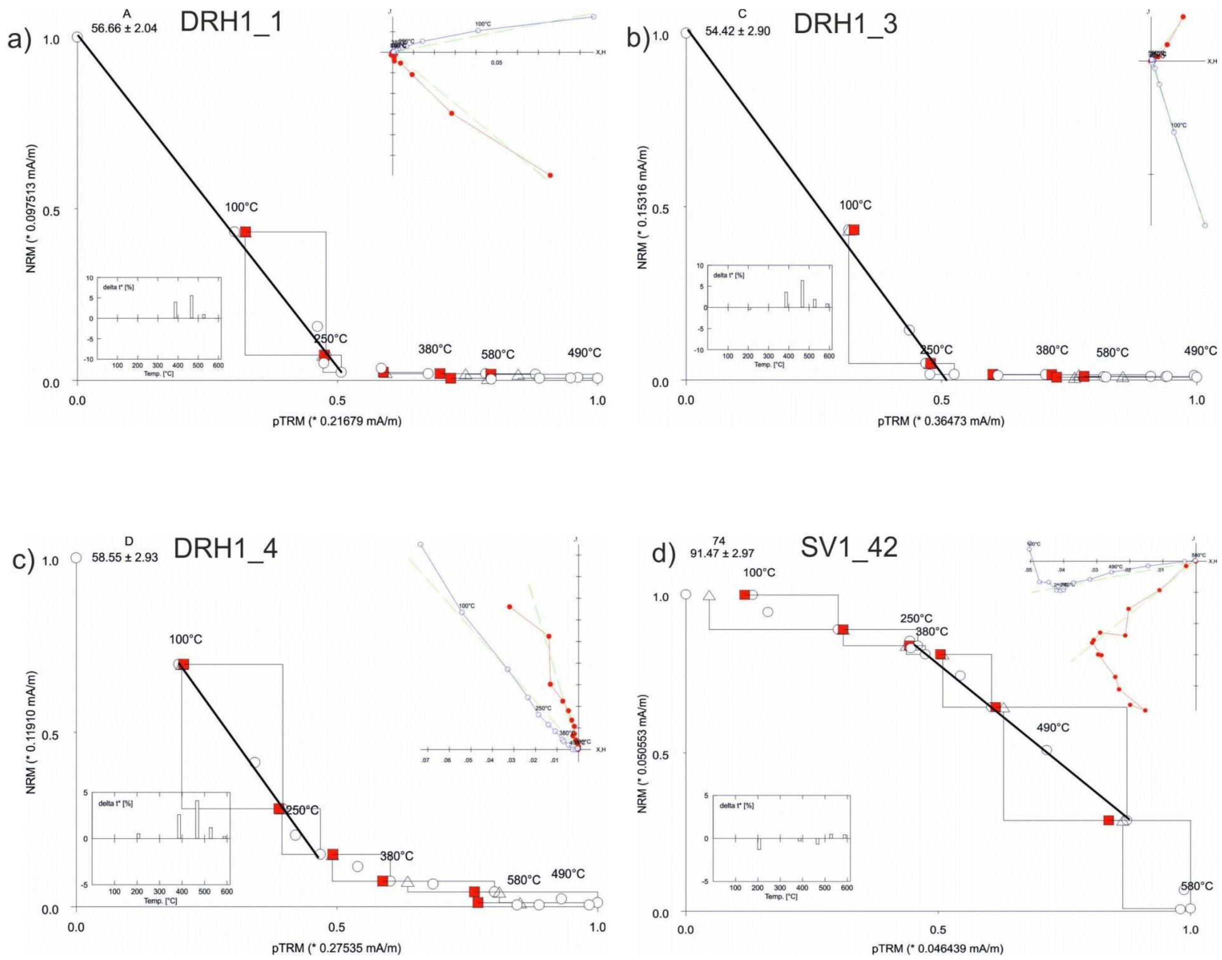

Figure 31: Four representative examples of accepted MT4 paleointensity determinations. The Arai plots (circles: pTRM/NRM values; triangles: alteration checks; squares: additivity checks) and orthogonal projections (vertical component and horizontal component) are shown, and the paleointensity determined from the slope of the straight line is displayed. (a) shows specimen DRH1_1, (b) sample DRH1_3, and (c) DRH1_4 (d) SV1_42.

The results of the Thellier experiments (see Fig. 31) are analyzed and interpreted on the basis of the criteria defined in Table 4 and analyzed in the z-direction.

Site BEH

Sample BEH1_12 (O) has an original intensity of 70.99 ± 3.64 µT. The selected temperature range starts at 0-300°C, since the sample is completely demagnetized at 250°C. Sample BEH1_12 is classified as class B with 70.75 ± 3.55 µT. BEH1-22 (P) shows an original intensity of 86.55 ± 5.59 µT. Due to a significant superimposing, the selected temperature range starts from 100°C and ends, due to complete demagnetization, at 420°C. Sample BEH1_22 belongs to class B with 86.47 ± 5.7 µT. BEH1_21 (Q) displays an original intensity of 72.53 ± 4.63 µT, and is also marked by a superimposing. The selected temperature ranges from 100 to 340°C with 71.38 ± 4.44 µT and is accepted as an exceptional case, although it belongs to class C.

Sample BEH1_12 (X) has an original intensity of 45.47 ± 4.28 µT and does not meet the criteria for the quality factor, and thus is rejected in further analyses. Samples of site BEH2_1 (T and U) start with an original intensity of 108.07 ± 4.19 µT and 89.53 ± 9.61 µT. Sample BEH2_18 (T) displays a significant overprint to a temperature of 200°C. The graph is anchored in line through origin and is unfeasible for further determination. This is also the case for sample BEH2_1, which reaches its unblocking temperature at 300°C and is disregarded due to its poor determination class.

Site HNH:

Sample HNH1_12 (11) has an original intensity of 78.45 ± 5.24 µT and reaches its unblocking temperature at 420°C. Thus, the selected temperature range is from 150 to 420°C. The sample belongs to class B. Sample HNH1_22 (12) has an intensity of 61.81 ± 2.09 µT and shows a significant overprint. It is disregarded in further analyses. Sample HNH1_31 (13) has an original intensity of 74.97 ± 9.90 µT and is completely demagnetized at 340°C. The selected temperature range is from 100 to 340°C and is determined with 75.22 ± 9.94 µT. Sample HNH1_12 (14) starts with 78.38 ± 3.45 µT and the selected temperature ranges from 0 to 380°C. The sample is categorized as class B with 75.22 ± 9.94 µT.

Site PV:

The mean paleointensity of sample PV1_11 (21) is 52.19 ± 9.58 µT. The sample shows a two-component system, but it is disregarded for further determination. Sample PV1_23 (22) has a mean paleointensity of 47.70 ± 4.34 µT and shows higher intensities at 100°C. It is suggested that, due to alteration, a new mineral phase is formed that has its unblocking temperature at 250°C. Sample PV1_31 (23) shows a low unblocking temperature and has a mean paleointensity of 47.02 ± 4.22 µT. Although site PV is determined as mineralogy type one, all samples are excluded from further measurements. The susceptibility curves in the high temperature measurements show very good properties and stability in susceptibility, but the remanence-bearing particles alternate and make the samples inoperative for the Thellier measurements.

Min type 2:

Site HK:

Specimen HK1_1 (5) displays a broadly thermal stability. The alteration test and additivity check show a slight variation. The factors d(AC) and d(CK) are very similar, which leads to SD-particles, but an alteration and mineralogical changes at 580°C can be observed. The mean that paleointensity is 49.40 ± 1.91 µT. Specimen HK1_23 also displays a broad thermal stability; the factor d(t*), which displays the fraction of MD grains, has its maximum at 520°C, and it is likely that the grains are pseudo-SD. The mean paleointensity is 59.49 ± 0.76 µT. The mean paleointensity of sample HK1_1 (7) is 56.77 ± 5.56 µT. Sample HK2_13 (8) shows only one primary direction and its mean intensity is 57.86 ± 3.56 µT. Sample HK1_1 (5) differs from other samples of this site and is removed in further analyses.

Site DRH

DRH1_1 (A) (Fig. 31a) has an intensity of 29.59 µT. The selected temperature range is from 0 to 300°C, where the sample reaches its unblocking temperature. The sample belongs to class B with 56.66 ± 2.04 µT. Sample DRH1_2 (B) displays an original value of 17.59 µT and is completely demagnetized at 300°C. The selected range is from 100 to 300°C, with 52.06 ± 6.64 µT. Specimen DRH1_3 (C) (Fig. 31b) has an original intensity of 24.66 µT. The temperature is selected from 0 to 300°C where the specimen is demagnetized. The intensity of the sample is determined with 54.42 ± 2.90 µT and it belongs to class B. The original intensity of DRH1_4 (D) (Fig. 31c) is measured with 52.67 µT. The selected temperature is from 100 to 300°C and displays 58.55 ± 2.93 µT. The intensity of DRH1_5 (E) was determined with 65.59 ± 1.93 µT in the range of 0 to 300°C, and it belongs to class B. The sample is characterized by a higher value of intensity than to the other samples of the same site. However, the fact that the sample shows a higher value of intensity but the same characteristics as other samples of this site is sufficient reason to accept the sample for further determination.

Site SAH

SAH2_11 (33) displays a more component system, has a mean paleointensity of 46.17 ± 5.72 µT and is characterized by significant alteration during treatment. SAH2_11 (34) displays an intensity of 50.67 ± 8.95 µT. Sample SAH2 _1 (35) displays intensity values of 59.65 ± 6.64 µT. According to the alteration during the measurement and significant differences in intensity in one site, all samples of SAH are disregarded in further determinations, although the site was classified as mineralogy type two.

Min type 3

Site SV

Sample SV1_13 (71) has an intensity of 40.85 ± 2.43 µT. The selected temperature range was 380 - 610°C, but criteria f (fraction of NRM) is too low for further analyses and leads to the disqualification of the sample. Specimens SV1_23 (72) and SV1_32 (73) show significant instability in their directions and a massive superimposing, so the samples are neglected in further analyses. In addition, sample SV1_32 (73) has an achievable higher intensity of 113.55 ± 6.98 µT, compared to other samples of the same site. Only samples SV1_42 (74) (Fig. 31d) and SV1_52 (75) of this site are accepted for further determinations. The selected temperature range for SV1_52 is from 380 to 610°C, and displays 87.01 ± 1.01 µT. Sample SV1_42 is determined from 340 to 520°C with 91.81 ± 2.89 µT and is classified as class C. The sample is accepted as an exceptional case because the measured graph is satisfactory in terms of intensity and orientation, and all other criteria are achieved. Moreover, the value of intensity matches the site.

Site HAH

Sample HAH1_1 (F) has an original intensity of 75.38 ± 3.07 µT. The temperature is selected for 380 to 520°C due to a massive overprint or second component in the sample. HAH1_1 displays an intensity of 84.26 ± 3.44 µT. Sample HAH1_2 (G) is also characterized by a significant superimposing or a second component, so the selected temperature ranges from 200 to 610°C. The sample HAH1_2 (G) has an intensity of 77.3 ± 1.38 µT. The overprint of sample HAH1_3 (H) is considerable, so the selected temperature is from 420 to 580°C. The determined intensity of the sample is 69.37 ± 1.28 µT. The original intensity of sample HAH1_4 (I) is 109.92 ± 6.31 µT, but the criteria data differ too much and thus the sample is neglected for further treatment. Equally, sample HAH1_5 (J) shows an intensity of 80.75 ± 8.36 µT, but the MD behavior makes it useless for further analyses.

Min type 4:

Site BDH

Specimen BDH1_1 (K) shows an original intensity of 55.41 ± 1.40 µT. The selected temperature ranges from 0 to 250°C with 54.22 ± 0.84 µT. The selected temperature for BDH1_21 (L) is from 0 to 250°C and the sample shows an intensity of 44.09 ± 4 µT. Due to the domain behavior, sample BDH2_1 (M) has not been selected for further dating analyses.

Paleointensity results from Snaefellsjökull

Site	***n/N***	***Specimen***	T_{min} *(C°)*	T_{max} *(C°)*	***Np***	***f***	***g***	***q***	***w***	***C***	***H ± S.D*** *(µT)*	F_w ***± S.D.***$_w$ *(µT)*
BDH	2/3	BDH1_1-K	0	250	5	0.54	0.74	25.9	15	B	54.2 ± 0.8	49.1 ± 7.1
		BDH1_21-L	0	250	5	0.56	0.74	4.6	2.7	B	44.1 ± 4.0	
BEH	3/6	BEH1_12-O	0	300	6	0.87	0.78	13.5	6.7	B	70.7 ± 3.5	76.2 ± 8.9
		BEH1_21-Q	100	340	6	0.88	0.71	10	5	C	71.3 ± 4.4	
		BEH1_22-P	100	420	8	0.77	0.7	8.2	3.3	B	86.4 ± 5.7	
DRH	5/5	DRH1_1-A	0	300	6	0.97	0.56	15.4	7.7	B	56.9 ± 2.0	57.3 ± 5.1
		DRH1_2-B	100	300	5	0.35	0.41	1.1	0.6	B	52.1 ± 6.6	
		DRH1_3-C	0	300	6	0.99	0.57	10.6	5.3	B	54.4 ± 2.9	
		DRH1_4-D	100	300	5	0.51	0.64	6.3	3.6	B	57.6 ± 2.9	
		DRH1_5-E	0	300	6	0.91	0.72	22.2	11.1	B	65.6 ± 1.9	
HAH	3/5	HAH1_1-F	380	520	5	0.34	0.63	5.3	3.1	B	84.5 ± 3.4	77.1 ± 7.5
		HAH1_2-G	200	610	12	0.86	0.84	40.8	12.9	B	77.3 ± 1.3	
		HAH1_3-H	420	580	6	0.58	0.74	23.4	11.7	B	69.3 ± 1.2	
HK	3/4	HK1_1-7	100	380	7	0.61	0.74	5.1	2.3	B	54.3 ± 4.8	57.1 ± 2.4
		HK1_23-6	100	420	8	0.61	0.8	36.8	15	B	59.0 ± 0.7	
		HK2_13-8	100	380	7	0.69	0.71	7.8	3.5	B	57.9 ± 3.6	
HNH	3/4	HNH1_11-14	0	380	8	0.91	0.7	17.1	7	B	76.3 ± 2.8	75.8 ± 0.5
		HNH1_12-11	150	420	7	0.91	0.64	8.8	4	B	75.9 ± 5.1	
		HNH1_31-13	100	340	7	0.57	0.63	2.7	1.2	B	75.2 ± 9.9	
PV	0/3											
SAH	0/3											
SV	2/5	SV1_42-74	340	520	6	0.38	0.73	9	4.5	C	91.8 ± 2.9	89.4 ± 3.3
		SV1_52-75	380	610	8	0.9	0.74	56.9	23.2	B	87.0 ± 1.0	

Table 5: Paleointensity results from Snæfellsjökull. Column (n/N) denotes the number of samples treated (N) versus the number of samples used (n). Columns T_{min} and T_{max} define the selected temperature ranges. Segment calculated over Np successive points. The fraction of the NRM (f), the gap factor (g) and the quality factor (q) were calculated according to Coe et al. (1978). Factor w denotes the weighting factor of Prévot et al. (1985). Factor C defines the class as described in the criteria section. Factors H and F_w are the paleointensity values with associated standard deviation (S.D.) for the individual determination and the weighted site mean (Leonhardt et al., 2003).

4.4 Dating

Selected samples which satisfactorily fulfill criteria from the processing steps with Thellier Tool4.22 are taken for further analyses with RenDate Version 1.0.5.7, developed by Lanos and Dufresne (Lanos et al., 1999). The method is based on the assumption that the thermoremanent magnetization, which is parallel and proportional to the geomagnetic field existing at the time and place where the cooling of the magnetic particles occurred. During cooling below the Curie temperature, the samples fix the direction of the magnetic field in the form of stable magnetization as inclination and declination. For a confidential orientation, in-situ conditions have to be taken into account. The parallelism between the attained magnetization and the magnetic field, and the consideration of the variance of intensity and of direction over time builds the basis of archeomagnetic dating. By means of these fundamentals and statistic parameters, the samples were calculated by means of a cumulative probability curve with a confidence of 95% (Lanos et al., 1999). The results allow the estimation of the ages of the lava flows. For this purpose the paleomagnetic directions were compared to inclination, declination and also to field intensity by using a Bayesian archeomagnetic dating approach (see Fig. 32). The Bayesian inversion method reduces the divergent power at the core-mantle boundary under data constraints. Various spherical harmonic geomagnetic field models, based on archeomagnetic data and historic observations, are determined for the last 10000 years. For this thesis the hierarchical Bayesian model was applied for testing the data in inclination, declination and intensity (Leonhardt et al., 2010; Schnepp, 2009). Tables for inclination, declination and intensity - starting with 5000 BC and ending with 1900 AD, were prepared in advance.

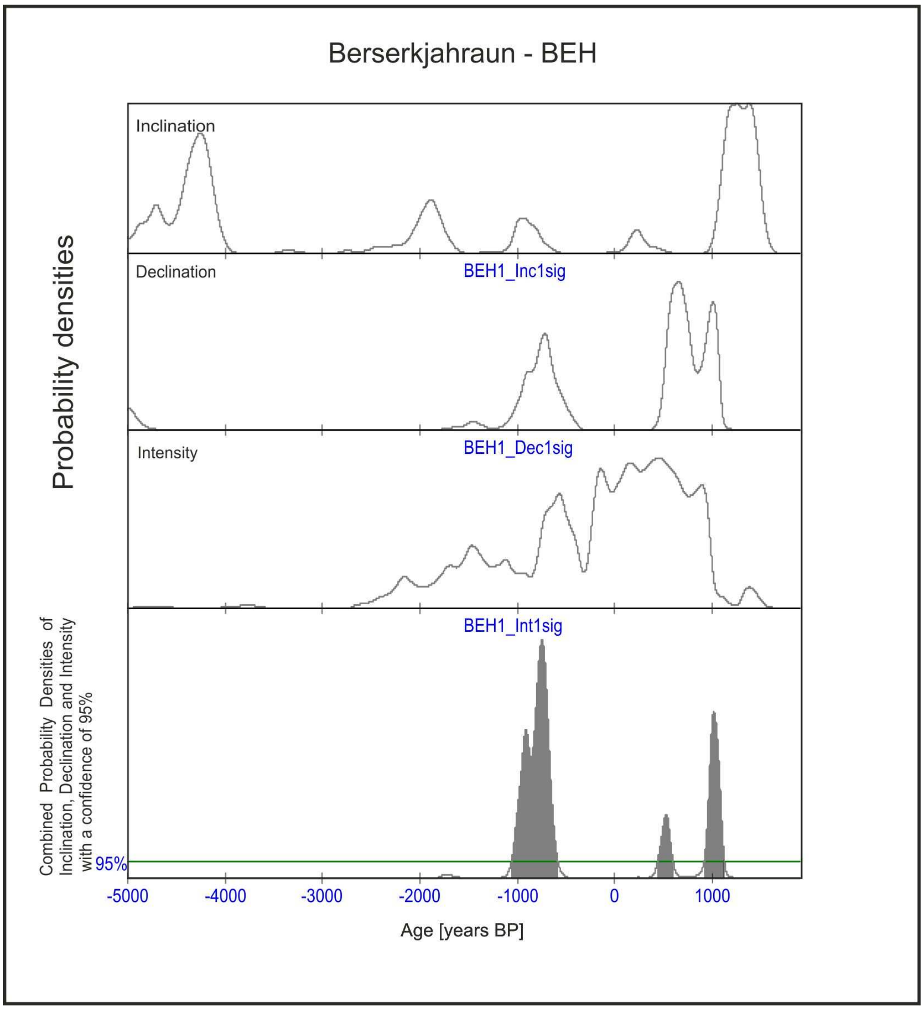

Figure 32: Example for calculation with RenDate. Sample BEH. The first graph displays the match probability in inclination and the graph below it shows the match probability in declination. The third curve presents the correlation of the field intensity. The last diagram demonstrates the probability density in combination with inclination, declination and field intensity, and indicates the confidence limit of 95%.

4.4.1 Archeomagnetic Dating

Results of RenDate

Beruvikurhraun – BEH

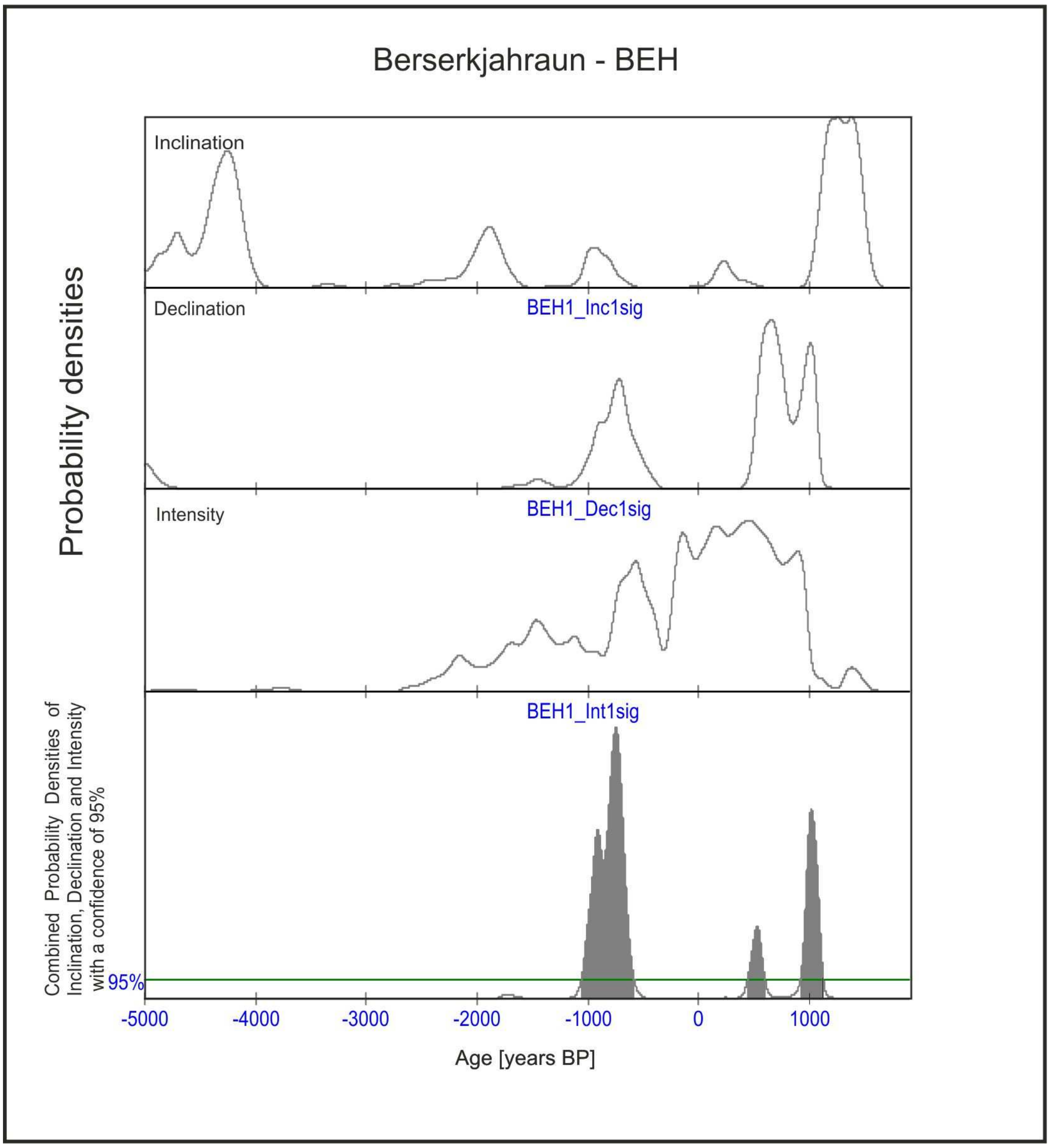

Figure 33: Age determination of Beruvikurhraun. The first graph displays the match probability in inclination and the graph below it shows the match probability in declination. The third curve presents the correlation of the field intensity. The last diagram demonstrates the probability density in combination with inclination, declination and field intensity, and indicates the confidence limit of 95%.

Dating results of Beruvikurhraun are illustrated in Figure 33 above. The first section displays the conformities in inclination with a confidence of 95%, correlated with the inclination curve. The correlation below it displays the analogy for the declination between 7000 years BP until the present. Compared to the inclination curve, the declination curve shows no conformities that are older than 1050 years BP. The correlation in field intensity is illustrated below the declination curve, and displays matches from 950 to 5450 years BP. The last section presents the combination of the inclination, declination and field intensity with a confidence of 95%. The magnetic consistencies in three different ranges exceed the 95% confidence limit. These conformities reveal three periods in which the lava flow could have gained its magnetization, according to the intensity model that compares the measured data to the adopted development of field intensity. One of these three periods ranges from 826 years to 1032 years BP. The second magnetic agreement is between 1508 and 1353 years BP. These periods are disregarded due to the assumption that the settlement of Iceland started in the late 9th and 10th centuries. When people first settled in Iceland, most of the volcanic eruptions were registered by wise men and no records exist from these time periods. The third accord is between 2535 and 3006 years BP (2770 ± 230), and is the most reasonable consistency for the age of Beruvikurhraun.

Budahraun – BDH

The dating results of BDH (Fig. 34) display similarities that reveal three totally different age ranges, which exceed the confidence limit of 95%. The inclination and declination curves display, respectively, a large amount of consistency in the period from 7000 years BP until the present. Thus, the correlation of field intensity data to the model agrees in more or less three periods. The youngest period calculated by the model that exceeds the 95% confidence limit (which is disregarded due to non-existent recent records) is from 51 to 430 years BP. Other periods that exceed the confidence limit are from 2753 to 2821 years BP; from 2890 to 3031 years BP; from 3132 to 3367 years BP, and from 4260 to 6950 years BP. The maximum likelihood is displayed with 4500 years BP (5600 ± 1300). Due to only slight variations in field intensity, a more precise classification within the limits of the accuracy of chronology is unfeasible.

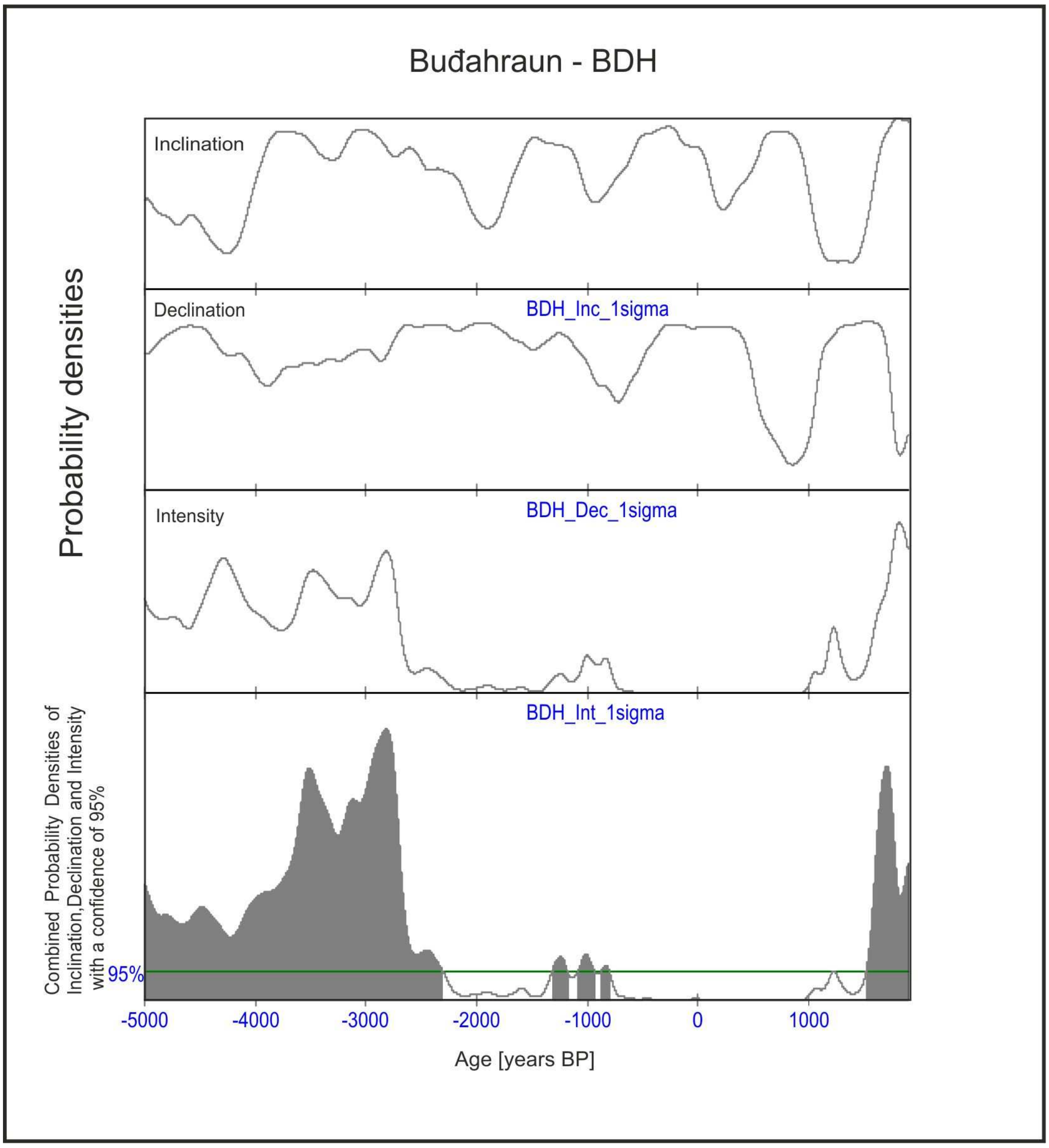

Figure 34: Age determination of BDH. The first graph displays the match probability in inclination and the graph below it shows the match probability in declination. The third curve presents the correlation of the field intensity. The last diagram demonstrates the probability density in combination with inclination, declination and field intensity, and indicates the confidence limit of 95%.

Haahraun – HAH

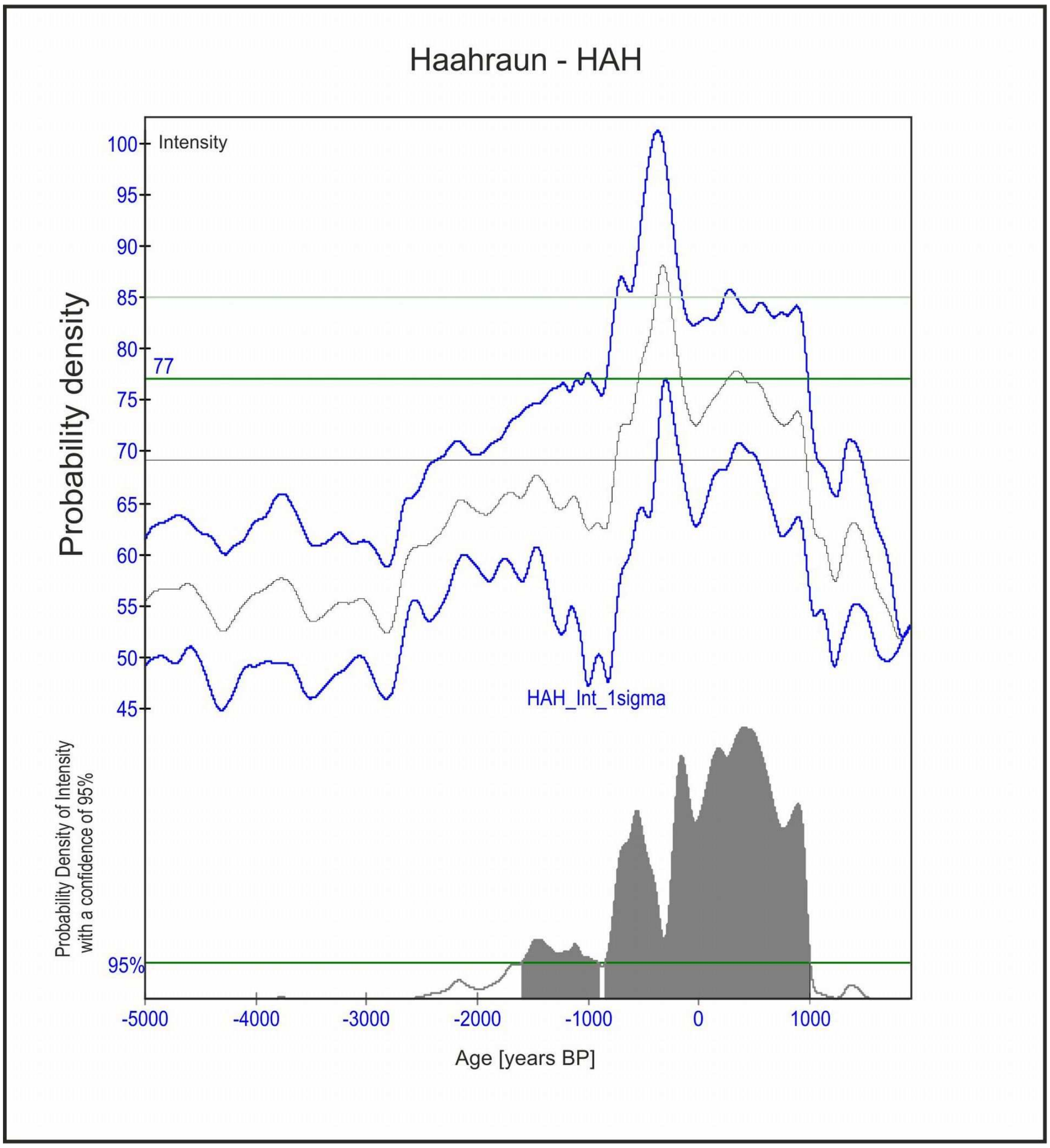

Figure 35: The figure displays the age determination of HAH, which is only calculated with data from field intensity. The confidence limit of 95% is indicated.

The results of the correlated data of HAH (Fig. 35) reveal only the field intensities. Due to the calculation with just one field component, the less precise results are apparent. The self-consistency of the measured data covers two periods ranging from 946 to 2798 years BP, and from 2856 to 3548 years BP. These two calculated periods cover an age range of 2000 years around the time of Christ’s birth. The maximum likelihood is given as 1872 ± 900 years BP.

Drangahraun – DRH

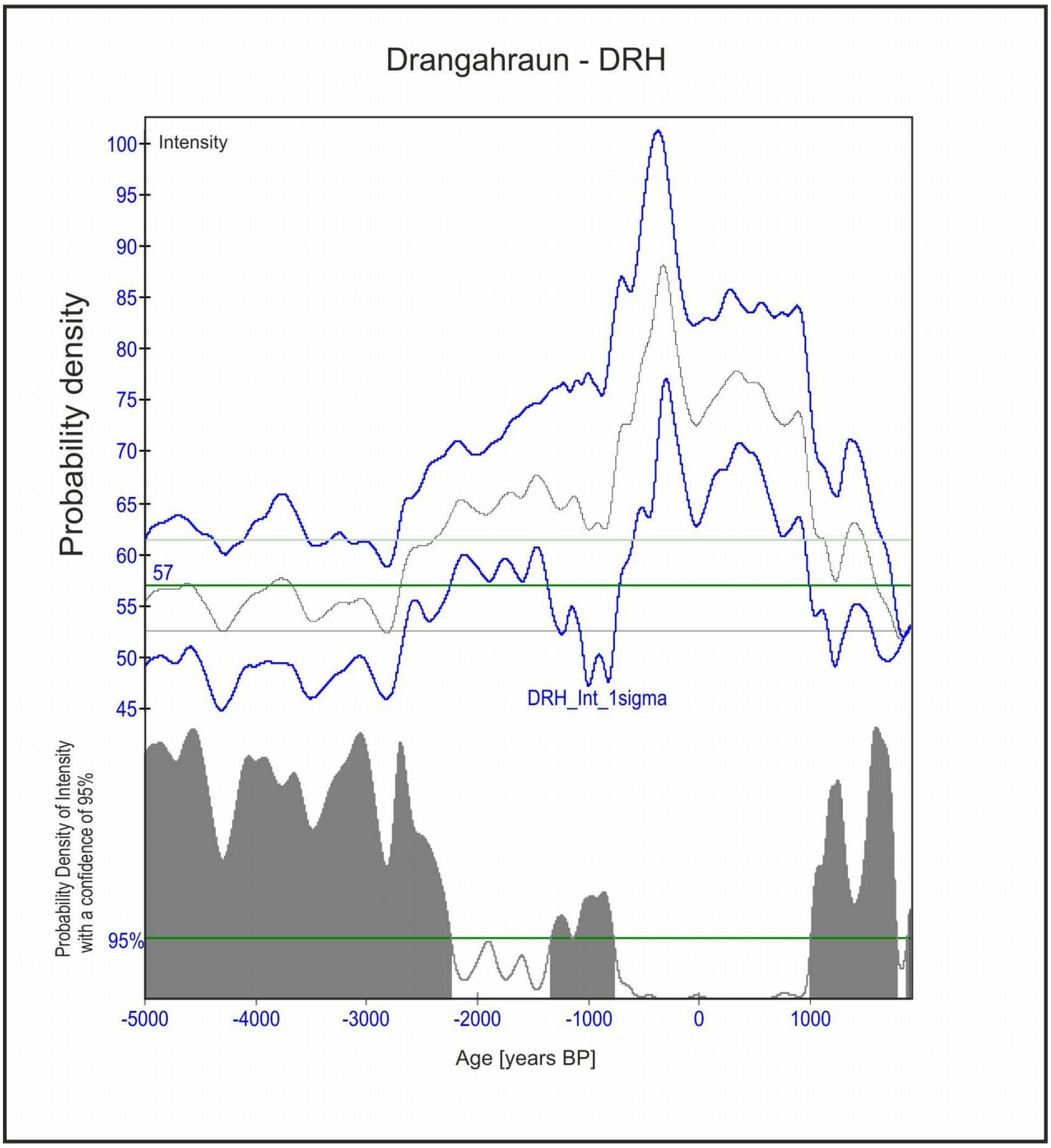

Figure 36: The graph illustrates the match probability of site DRH determined with field intensity. The confidence limit of 95% is indicated.

The results of site DRH (Fig. 36) also represent just one field component, as was the case for site HAH. Due to the measured field intensity of 57 µT, the ranges of conformities in the model are mostly not as precise as for calculations of 3 field components. The variations in field intensity cover three main periods that exceed the confidence limit of 95%. The first period ranges from 945 to 170 years BP and is disregarded due to the fact that there were no other reports in that time. The second period ranges from 2724 to 3385 years BP, and the third phase covers a period from 4191 to 6950 years. A more precise accuracy of chronology is not possible within the calculation for one field component. The maximum likelihood for the age of site DRH is given as more than 4500 years BP (5570 ± 1100).

Svartahraun / Valhraun – SV

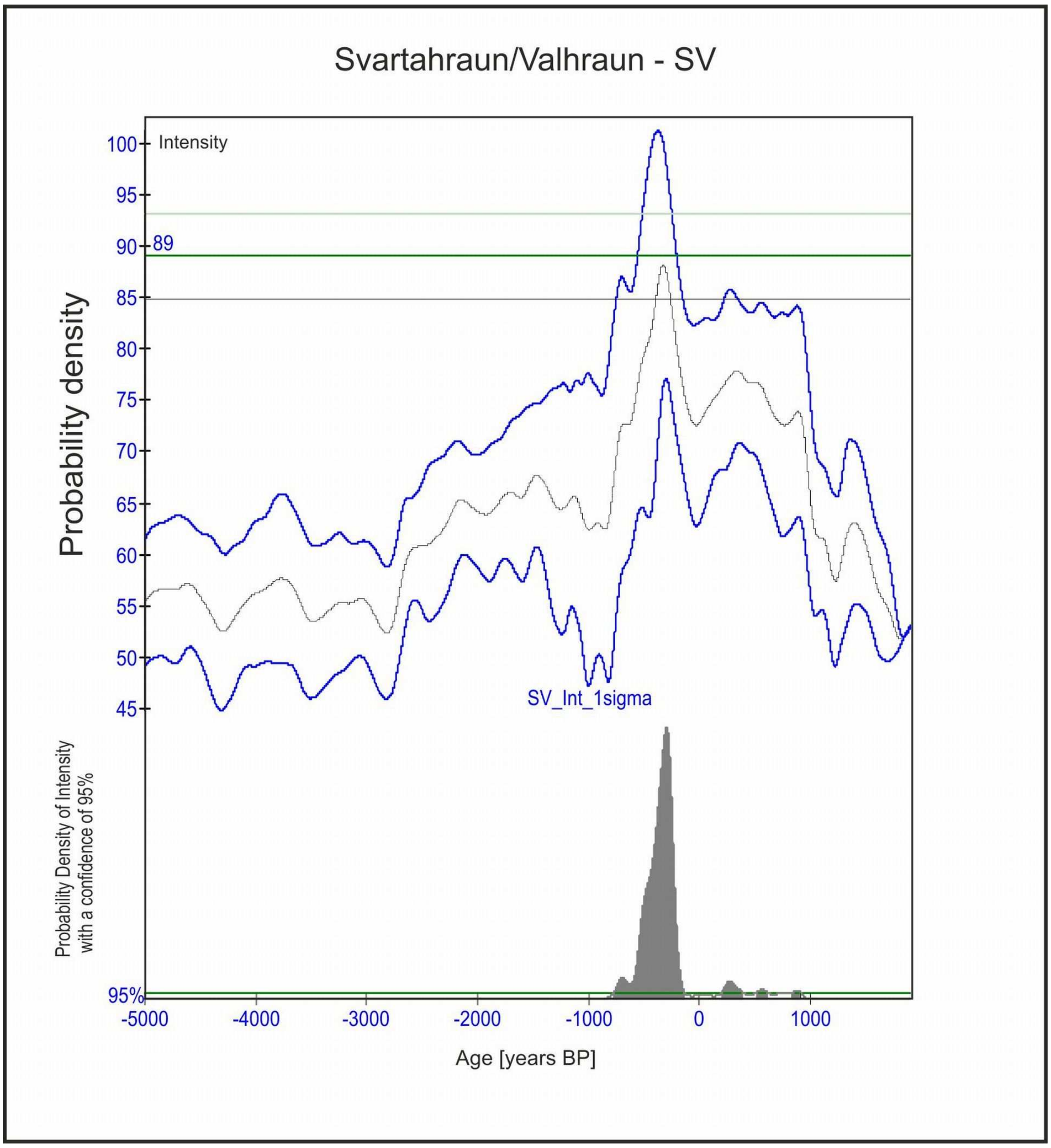

Figure 37: The age determination of site SV, which displays the probability density of 95%, calculated from field intensity. The confidence limit of 95% is indicated.

The results of site SV (Fig. 37) are only calculated within the field intensity. Within the framework of faults, the field intensity matches periods around Christ's birth. The youngest period, exceeding the confidence limit of 95%, ranges from 1111 to 1039 years BP. Other conformities are calculated for 1338 to 1433 years BP, for 1565 to 1751 years BP and for 2083 to 2721 years BP. The maximum likelihood is given to an age range of 1565 to 1751 years BP (1650 ± 100).

Hellnahraun / Kalfatrađahraun – HK

The dating for the site Hellnahraun/Kalfatrađahraun (Fig. 38) was determined for inclination, for declination and for field intensity. A magnetic conformity for six different periods that exceed the confidence limit of 95% was identified. Due to slight intensity variations in a period of 1000 to 2800 years BP, the confidence of 95% is given from 271 to 899 years BP, from 2767 to 3078 years BP, from 3148 to 3220 years BP, from 3757 to 3966 years BP, from 4163 to 4689 years BP and from 6046 to 6950 years BP. These periods represent the time within which the lava flow could have acquired its magnetization. The maximum likelihood is calculated in the youngest and the oldest periods. Due to the absence of records for the period after the birth of Christ (1950 years BP), the likelihood for the age of the period is more than 6046 years BP (6500 ± 450).

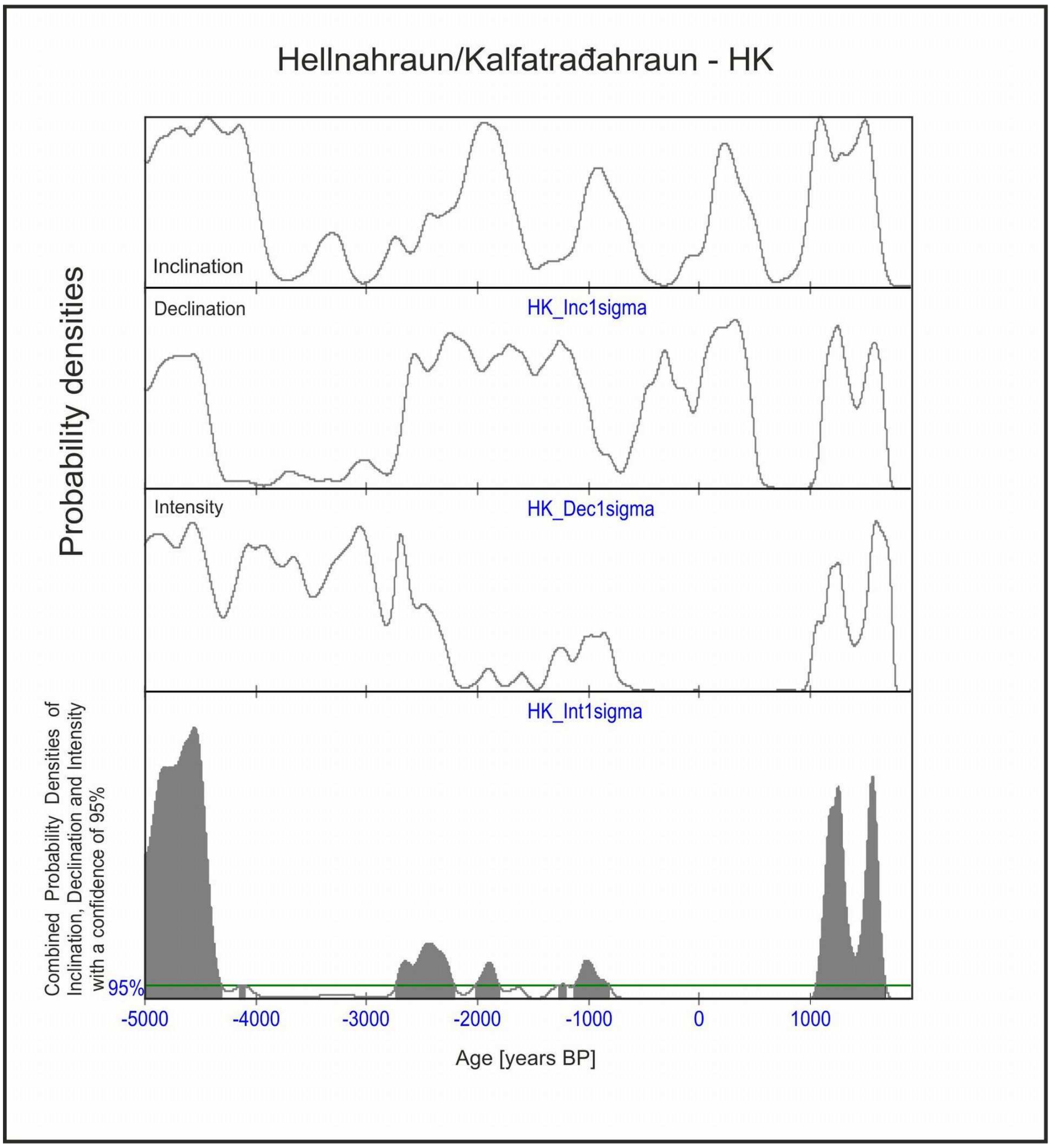

Figure 38: Age determination of HK. The first graph displays the match probability in inclination and the graph below it shows the match probability in declination. The third curve presents the correlation of the field intensity. The last diagram demonstrates the probability density in combination with inclination, declination and field intensity, and indicates the confidence limit of 95%.

Hnaushraun – HNH

The analysis for HNH (Fig. 39) with RenDate was determined for inclination, declination and field intensity. The inclination covers a broad time range; hence, the declination and intensity curves display only a slight variation and show peaks only for certain age periods. These combined results of inclination, declination and field intensity are illustrated. They exceed the confidence limit of 95% in the period from 1565 to 1543 years BP, from 1602 to 2200 years BP and in a third phase ranging from 2320 to 2417 years BP. The maximum likelihood for the period in which the lava flow acquired its magnetization is given as 1602 to 2200 years BP (1900 ± 300), which covers a range of 598 years around the birth of Christ (1950 years BP).

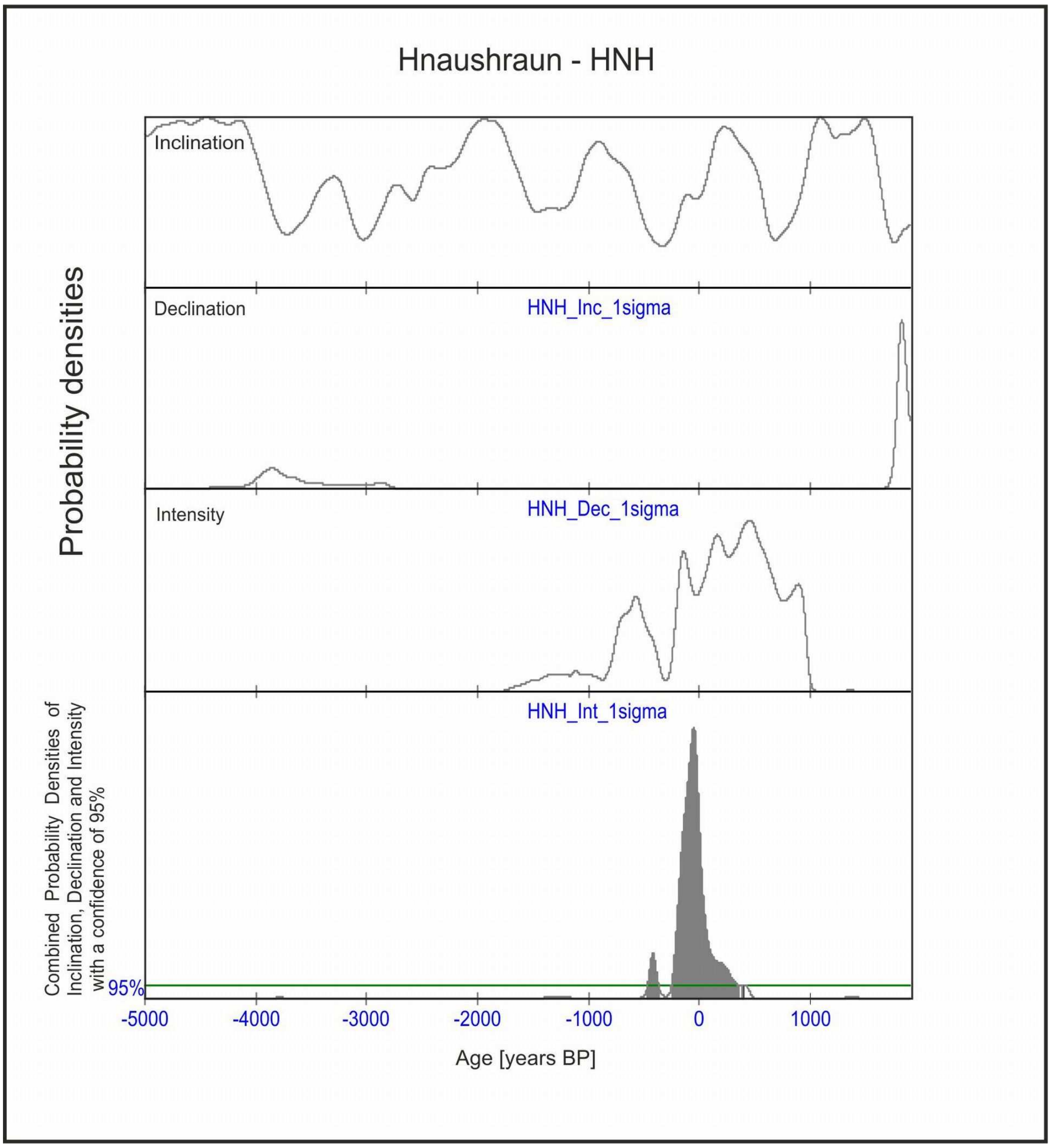

Figure 39: Age determination of HNH. The first graph displays the match probability in inclination and the graph below it shows the match probability in declination. The third curve presents the correlation of the field intensity. The last diagram demonstrates the probability density in combination with inclination, declination and field intensity, and indicates the confidence limit of 95%.

5 Discussion

Discussion

After the conduction of mineralogy and thermal alteration measurements, the samples were classified into four different groups, according to their mineral changes during high temperature measurements and alteration changes. A pre-selection was made according to their class of mineralogy and alteration. Preference was given to samples of mineralogy type one and two as well as to the alteration type one and two. For a comparison and to increase the trustiness of these classifications, a few representative samples of mineralogy type three and four were additionally selected. The reliability and precision of the maximum likelihood are much higher in samples of mineralogy type one or two compared to lower class samples. For example, the measurements of site BEH; site BEH is assigned to mineralogy type one and alteration type one. The precision of data that exceed the confidence limit of 95% is significant, and is illustrated in Figure 33 for site BEH. The qualities of the samples with mineralogy type three or four is illustrated in Figure 34, which displays site BDH as an example for mineralogy type four. In a comparison of these data and their qualities, the success of the pre-selection is indicated.

The anisotropy of magnetic susceptibility is an indicator for verifications about processes during formation of the rocks and further mechanical deformations, new mineral formations or metamorphoses (Soffel, 1991). For the dating procedure, samples with very low anisotropy were needed. Due to the minor anisotropy of magnetic susceptibility, it is assumed that the anisotropy of remanence is also very low; hence, a correction of the anisotropy was forgone. The factor P, the degree of anisotropy, and factor P_j, the corrected factor of anisotropy (see chapter 4, methods), were consulted for an evaluation of anisotropy. The corrected factor of anisotropy was 1.027 [SI] in average with extremum of 1.09 [SI] and was taken as negligible values of anisotropy. It also leads to the conclusion that samples in this range are not faulted.

Samples of BEH1 and BEH2 differ in their anisotropy (see Fig. 18f). The AMS of BEH2 is much higher (P_j is 1.396 [SI]) than that of BEH1 (P_j of BEH1_12a is 1.009 [SI] and for BEH1_23a 1.004 [SI]). This effect is also reflected in measured paleointensities, and gives sufficient reason to exclude BEH2 from further dating analyses. The higher anisotropy would make the dating analyses less reliable.

All samples were corrected according to their strike and dip direction, as measured by Roman Leonhardt during the field trip to Iceland in summer 2009. Only two samples are non-oriented, because they are fragments of bedrock (HAH and DRH). In addition, the measurements should indicate the orientation consistency throughout one site. Due to block rotations of some of the sites and problems of the orientation marking, the orientations of some samples could not be identified. Hence, 7 of all lava flows present reliable data in inclination, in declination and in field intensity, which are expected for the region of Iceland and are used for further analyses. The age dating analyses display inaccuracies as a function of the method. The determined lava flows are:

Beruvikurhraun – BEH: 2770 ± 230 BP

Budahraun – BDH: 5600 ± 1300 BP

Haahraun – HAH: 1872 ± 900 BP

Drangahraun – DRH: 5570 ± 1100 BP

Svartahraun/Valhraun – SV: 1650 ± 100 BP

Hellnahraun/Kalfatrađahraun – HK: 6500 ± 450 BP

Hnaushraun – HNH: 1900 ± 300 BP

The determination shows similarities within the calculated ages. The lava flows of Haahraun – HAH (Fig. 35) and Hnaushraun – HNH (Fig. 39) are determined with 1872 ± 900 BP and 1900 ± 300 BP, respectively. The age range of Hnaushraun is more precise according to analyses in inclination, declination and field intensity for HNH, in comparison to HAH where the determination was just for the field intensity. However, both lava flows display ages of around the birth of Christ, 1950 years BP. The determined age of Haahraun matches measured tephra markers, which are calculated with 1755 ± 45 years BP in contrast to site HNH, whose age, determined by means of paleomagnetics, is 1900 ± 300 years BP and is calculated with 3960 ± 130 BP from tephra chronology (Smith, K. T., Sigurðsson, F., Sturkell, E. 2008). It is unlikely that lava flow HNH belongs to the tephra event from 3960 years BP; the flow rather appears be related to the eruption of 1755 ± 45 years BP.

A further analogy is observed for the site Svartahraun/Valhraun – SV, whose age is calculated with 1650 ± 100 years BP (Fig. 37). This is contemporaneous with site HAH, although the determination displays only the field intensity; the range is very accurate. The tephra chronology for Svartahraun is given as 1755 ± 45 years BP, and correlates well to measured data in this thesis.

The dating of Beruvikurhraun – BEH displays 2770 ± 230 years BP (Fig. 33) in comparison to the tephra ages of BEH measured as 3960 ± 130 years BP. An interpretation of BEH data led to the result that this flow is connected neither to the event of 1755 ± 45 BP, nor the tephra from 3960 ±130 BP. It is more likely that this was an independent volcanic occurrence. The age of lava flow determined for BEH matches an eruption that occurred 2720 ± 600 years BP (see Table 2). Although the area of this eruption was reported as being at the north-west flank of Snæfells, it is more likely that this area has to be extended to the locality of BEH, according to the ages determined.

Another episode is determined for samples of BDH, DRH and HK. The age of Buđahraun (Fig. 34) is determined as 5600 ± 1300 years BP, for Drangahraun (Fig. 36) as 5570 ± 1100 years BP, and for Hellnahraun/Kalfatrađahraun (Fig. 38) as 6500 ± 450 years BP. These hrauns represent the oldest ages of measured samples. Unfortunately, there is no exact equivalent dating of tephra for Buđahraun to compare this with. Whereas Drangahraun is dated at 5570 ± 1100 years BP, it can be compared to the age of tephra with 3960 ± 130 years BP. This tephra layer is presented as Sn-2 (Snæfells 2) (Jóhannesson, 1981). Site Hellnahraun/Kalfatrađahraun also fits this episode and is dated as 6500 ± 450 BP. Measurements of tephra of Kalfatrađahraun reveal a period of 8590 ± 1100 years BP and are presented as Sn-3 (Snæfells 3) (Jóhannesson, 1981; Smith, K. T., Sigurðsson, F., Sturkell, E. 2008). The age determination of DRH and HK do not exactly fit with the ages of tephra; however the ages are dated in the same time period within the suitable threshold of failure. Imprecision occurring especially with the oldest of determined ages is probably due to the inaccuracy of the geomagnetic model. It has to be mentioned that the calculated ages, determined with radiocarbon analyses, are sampled from tephra layers and soil, and not from lava flows themselves. These data are related to volcanic events that may have produced the lava flows. But in fact, tephra falls cannot be extrapolated with lava flows. The volcanic eruption of Eyjafjallajökull in April 2010 was dominated by unusual amounts of fine-grained ash. The ash clouds transported the fine particles over a large area. A determination of these tephra in distant time would reflect the age of and not the origin of Eyjafjallajökull.

The determined ages can be roughly divided into three groups. The first group of sites erupted around the birth of Christ, 1950 years BP, (HAH, HNH, SV), the ages of the second group are calculated at about 3000 years BP (BEH), and the third group displays ages of over 5000 years BP (BDH, DRH, HK). There are no matching data in the period from 3000 to 5000 years BP, which represents a period of over 2000 years without any validated volcanic activity. The gap of data in this period could indicate an eruption cycle of the Snæfells volcano. The oldest ages determined are more than 5000 years BP, the next group around 3000 years BP, and the youngest around the birth of Christ, 1950 years BP. The volcano has now been inactive for the last 2000 years, but it should be noted that similar periods have also been recorded in the past and, in fact, there is no evidence that the Snæfells volcano does not erupt in cycles of 2000 years.

6 Appendix

List of Abbreviations of Snæfellsjökull Sites

Berserkjahraun	BSH
Sandarhraun	SAH
Prestahraun/Væjuhraun	PV
Neshraun	NSH
Burstahraun	BUH
Beruvikurhraun	BEH
Drangahraun	DRH
Svartahraun/Valhraun	SV
Haahraun	HAH
Blafeldarhraun	BLH
Buđahraun	BDH
Hnaushraun	HNH
Klifhraun	KLH
Hellnahraun/Kalfatrađahraun	HK

Table of Samples for NRM

BEH 1	BEH1_12b
	BEH1_12a
	BEH1_22a
	BEH1_22b
	BEH1_23b
	BEH1_24a
	BEH1_24b
BEH 2	BEH2_11a
	BEH2_12a
	BEH2_14a
	BEH2_16a
	BEH2_17a
	BEH2_18a
BLH 1	BLH1_11a
	BLH1_11b
	BLH1_12b
	BLH1_13a
	BLH1_13b
BSH 1	BSH1_11a
	BSH1_11b
	BSH1_12b
	BSH1_21a
	BSH1_21b
	BSH1_22a
	BSH1_22b
	BSH1_23a
	BSH1_31a
	BSH1_33a
	BSH1_33b
	BSH1_34a
BUH 1	BUH1_11a
	BUH1_11b
	BUH1_12a
	BUH1_12b
	BUH1_13b
	BUH1_14a
	BUH1_14b
	BUH1_15a
	BUH1_22a
	BUH1_32a
HK 1	HK1_21a
	HK1_22a
HK 2	KH2_11b1

	HK2_12a1
	HK2_13a1
HNH 1	HNH1_11a
	HNH1_12b
	HNH1_13a
	HNH1_21a
	HNH1_22a
KLH 2	KLH2_11b
	KLH2_12a
	KLH2_22a
	KLH2_23a
	KLH2_23b
NSH 1	NSH1_11a
	NSH1_12b
	NSH1_21a
	NSH1_21b
	NSH1_22a
	NSH1_23a
	NSH1_23b
	NSH1_24a
	NSH1_24b
	NSH1_31a
	NSH1_31b
	NSH1_32b
	NSH1_33a
	NSH1_33b
PV 1	PV1_11b
	PV1_12a
	PV1_21a
	PV1_22a
	PV1_23a
	PV1_24a
	PV1_26a
	PV1_31a
	PV1_31b
	PV1_32b
SAH 1	SAH1_11a
	SAH1_22a
SAH 2	SAH2_12a

Tables of Samples for ARM

BDH	BDH1_21A
	BDH2_11A
BEH	BEH1_12A
	BEH2_15A
BLH	BLH1_12A
	BLH2_22A
BSH	BSH1_12A
	BSH1_23A
	BSH1_32A
BUH	BUH1_13A
	BUH1_21A
	BUH1_31A
HK	HK1_23A
	HK2_11A
HNH	HNH1_12A
	HNH1_23A
KLH	KLH2_11A
	KLH2_21A
NSH	NSH1_12A
	NSH1_22B
	NSH1_32A
PV	PV1_11A
	PV1_25A
	PV1_32A
SAH	SAH1_12A
	SAH1_21A
	SAH2_11A

Table of Samples for High and Low Temperature Measurements

	High temperature		Low Temperature
BDH 1	BDH1_200		BDH1A
	BDH1_400		BDH1B
	BDH1_700		
BEH 2	BEH2_200		BEH2A
	BEH2_400		
	BEH2_700		
BLH2	BLH2_200		BLH2A
	BLH2_400		
	BLH2_700		
BSH 1	BSH1_200		BSH1A
	BSH1_400		BSH1B
	BSH1_700		
BUH 1	BUH1_200		BUH1A
	BUH1_400		
	BUH1_700		
HK 1	HK1_200		HK1A
	HK1_400		
	HK1_700		
HNH 1	HNH1_200		HNH1A
	HNH1_400		
	HNH1_700		
KF 1	KF1_200		KF1A
	KF1_400		
	KF1_700		
KLH 2	KLH2_200		KLH2A
	KLH2_400		KLH2B
	KLH2_700		
NSH 1	NSH1_200		NSH1A
	NSH1_400		
	NSH1_700		
PV 1	PV1_200		PV1A
	PV1_400		
	PV1_700		
SAH 2	SAH2_200		SAH2A
	SAH2_400		
	SAH2_700		
SV 1	SV1_200		SV1A
	SV1_400		
	SV1_700		

Table of Samples for AMS

BDH	BDH1-21A
BEH	BEH1-12A
	BEH1-23A
	BEH2-15A
BLH	BLH1-12A
	BLH2-22A
BSH	BSH1-12A
	BSH1-23A
	BSH1-32A
BUH	BUH1-13A
	BUH1-21A
	BUH1-31A
HK	HK1-23A
	HK2-11A
HNH	HNH1-12A
	HNH1-23A
KLH	KLH2-11A
	KLH2-21A
NSH	NSH1-12A
	NSH1-22B
	NSH1-32B

Table for Mini-Inch Cores for Thellier Measurements

A	DRH1_1
B	DRH1_2
C	DRH1_3
D	DRH1_4
E	DRH1_5
F	HAH1_1
G	HAH1_2
H	HAH1_3
I	HAH1_4
J	HAH1_5
K	BDH1_1
L	BDH1_21 Top
M	BDH2_1
O	BEH1_12 Top

P	BEH1_22 Top
Q	BEH1_21 End
T	BEH2_18 Top A
U	BEH2_12 End
V	BEH2_14 Top
X	BLH1_12 End
Y	BLH2_1
Z	BLH2_21 End
1	BSH1_12 Top
2	BSH1_22 Top
3	BSH1_32 End
4	BSH1_32 Top
37	BSH1_34 End
5	HK1_1
6	HK1_23 Top
7	HK1_1
8	HK2_13 Top
11	HNH1_12 Top
12	HNH1_22 Top
13	HNH1_31 Top
14	HNH1_11 Top
21	PV1_11B
22	PV1_23 Top
23	PV1_31 Top
31	SAH1_12 End
32	SAH1_22 A
33	SAH2_11 End
34	SAH2_11 Top

35	SAH2_1
36	SAH2_1
37	BSH1_34 End
41	BUH1_14 Top
42	BUH1_22 Top
43	BUH1_31 End
51	NSH1_12 Top
52	NSH1_23 Top
53	NSH1_31 Top
61	KLH1_11 Top
62	KLH1_11 End
63	KLH2_12 Top
64	KLH2_21 Top

Measuring Steps for Thellier Measurements

Temperature (°C)	Type	Code	Comments
0 – NRM	TH	0	
100	TH	100	
100	PT	101	
150	TH	150	
150	PT	151	
200	TH	200	
100	CK	102	
200	PT	201	
100	AC	103	
200	TL	204	
250	TH	250	
250	PT	251	
300	TH	300	
200	CK	202	
300	PT	301	
200	AC	203	
340	TH	340	
340	PT	341	
380	TH	380	
300	CK	302	
380	PT	381	

300	AC	303	
380	TL	384	
420	TH	420	
420	PT	421	
460	TH	460	
380	CK	382	
460	PT	461	
380	AC	383	
460	TL	464	
490	TH	490	
490	PT	491	
520	TH	520	
460	CK	462	
520	PT	521	
460	AC	463	
520	TL	524	
550	TH	550	
550	PT	551	
580	TH	580	
520	CK	522	
580	PT	581	
520	AC	523	
580	TL	584	
610	TH	610	
610	PT	611	

Samples for Thellier Measurements:

Group 1:	
BEH1_12	O, X
BEH1_22	P
BEH1_21	Q
BEH2_18	T, U
PV1_11B	21
PV1_23	22
PV1_31	23
HNH1_12	11, 14
HNH1_22	12
HNH1_31	13
HK1_1	5
HK1_23	6
HK1_1	7
HK2_13	8
Group 2:	
DRH1_1	A

DRH1_2	B
DRH1_3	C
DRH1_4	D
DRH1_5	E
SAH2_11E	33
SAH2_11T	34
SAH2_1	35
SV1_13	71
SV1_23	72
SV1_32	73
SV1_42	74
SV1_52	75
HAH1_1	F
HAH1_2	G
HAH1_3	H
HAH1_4	I
HAH1_5	J
BDH1_1	K
BDH1_21	L
BDH2_1	M

Beruvikurhraun BEH

BEH1_12a   Alteration type 1

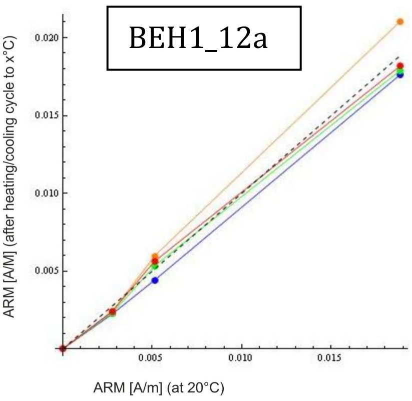

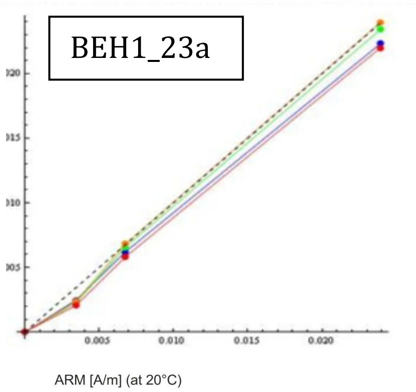

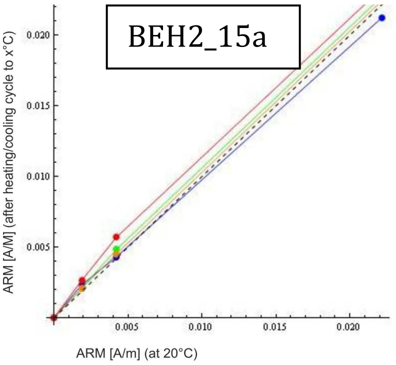

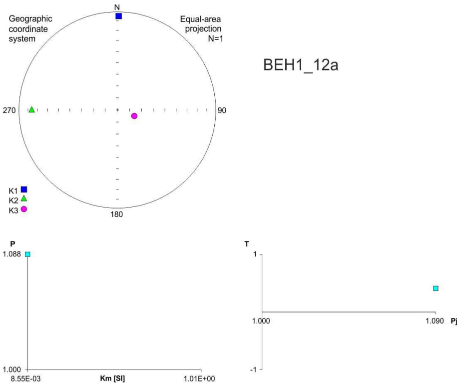

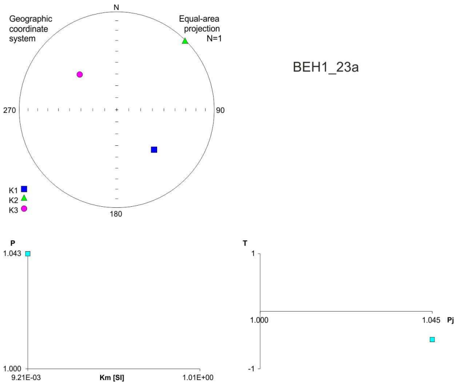

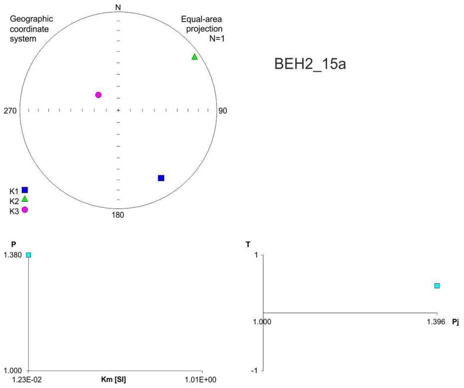

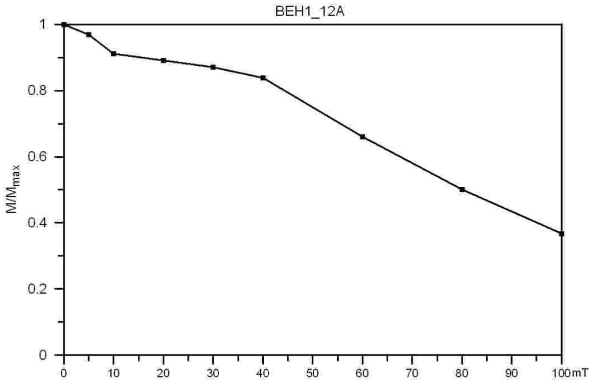

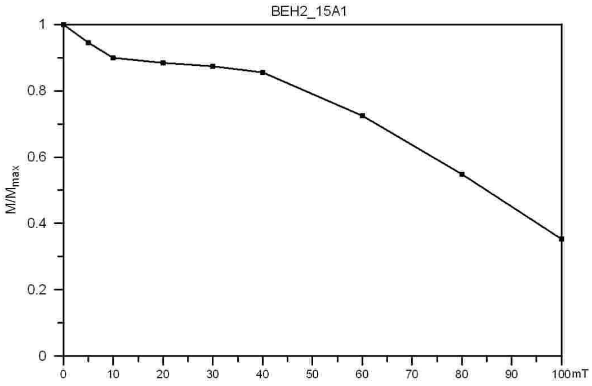
BEH2_15A1
M/Mmax
1
0.8
0.6
0.4
0.2
0
0
10
20
30
40
50
60
70
80
90
100mT

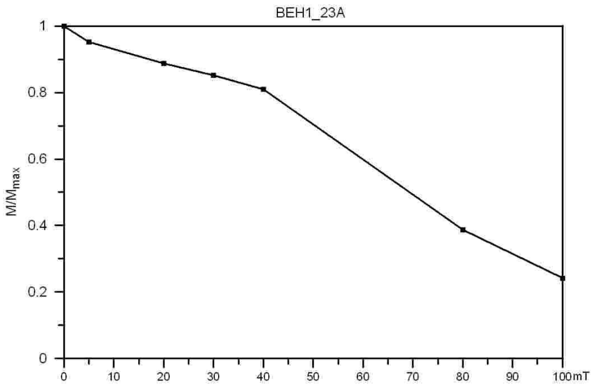
BEH1_23A
M/Mmax
1
0.8
0.6
0.4
0.2
0
0
10
20
30
40
50
60
70
80
90
100mT

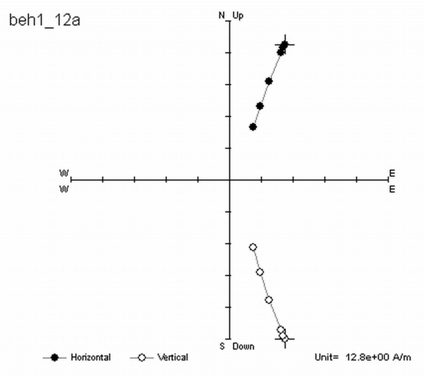
beh1_12a
N Up
W
W
E
E
S Down
Horizontal
Vertical
Unit= 12.8e+00 A/m

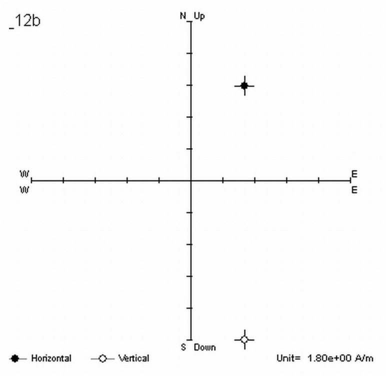
_12b
N Up
W
W
E
E
S Down
Horizontal
Vertical
Unit= 1.80e+00 A/m

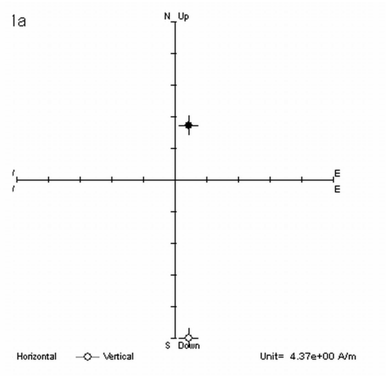
1a
N Up
E
E
S Down
Horizontal
Vertical
Unit= 4.37e+00 A/m

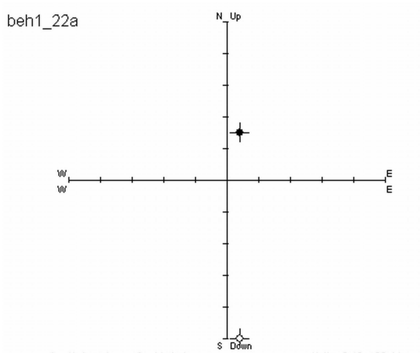
beh1_22a
N Up
W
W
E
E
S Down
Horizontal
Vertical
Unit= 3.12e+00 A/m

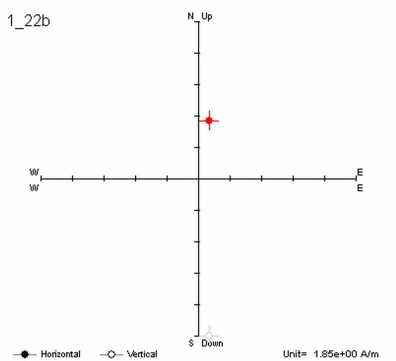
1_22b
N Up
W
W
E
E
S Down
Horizontal
Vertical
Unit= 1.85e+00 A/m

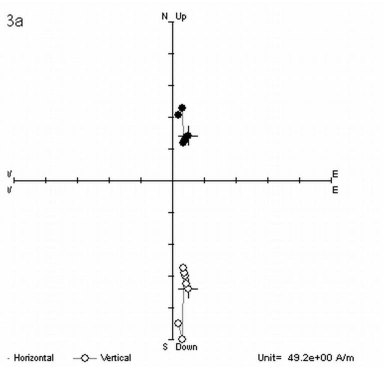
3a
N Up
E
E
S Down
Horizontal
Vertical
Unit= 49.2e+00 A/m

BEH1

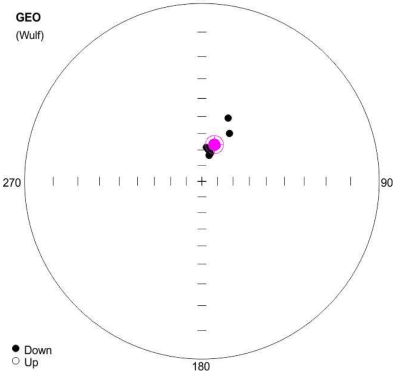
N
GEO
(Wulf)
270
90
180
Down
Up

BEH2

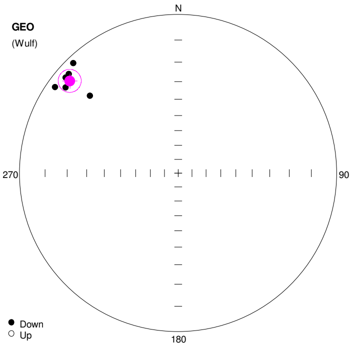
N
GEO
(Wulf)
270
90
180
Down
Up

BEH2_15a: MDF = 85,0 mT

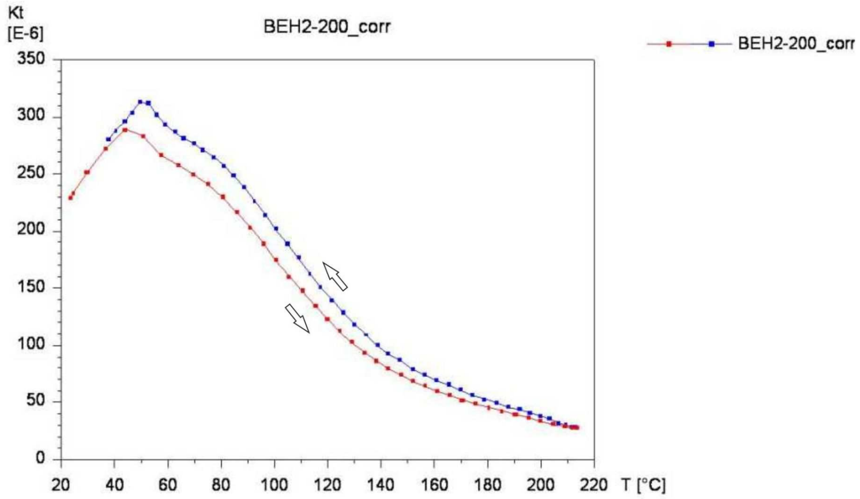

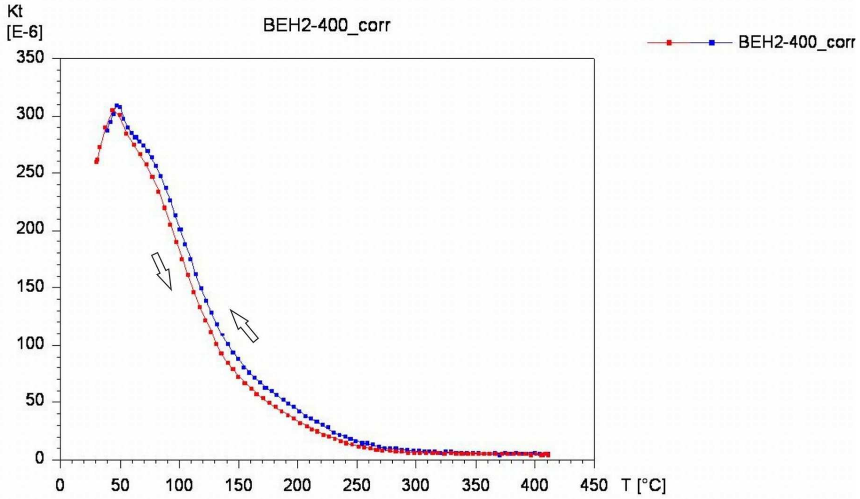

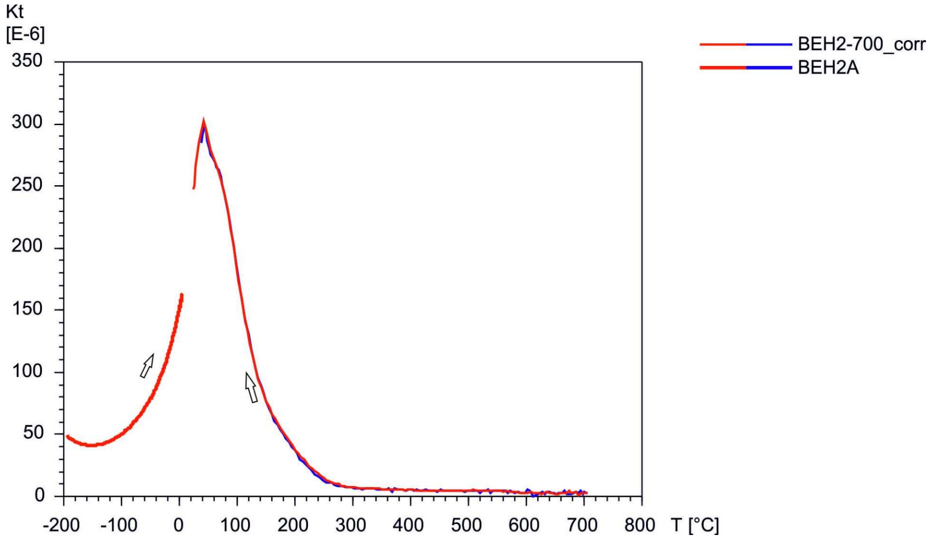

Hellnahraun/Kalfatraðahraun HK

HK1_23A Alteration type 1

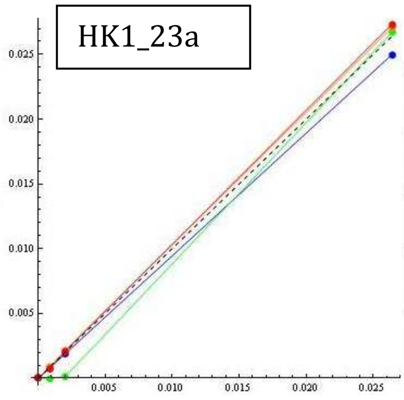

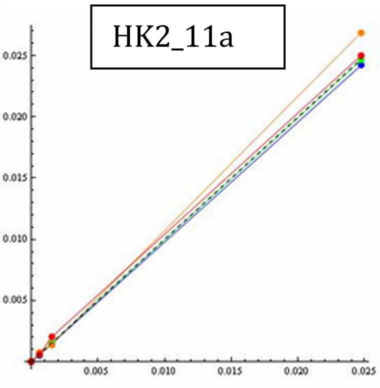

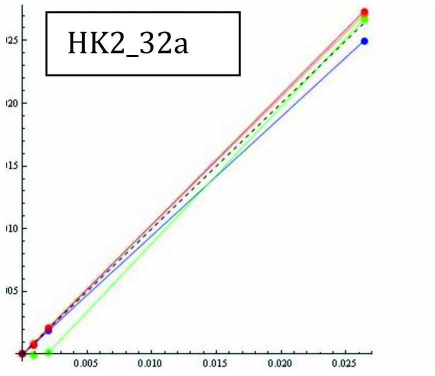

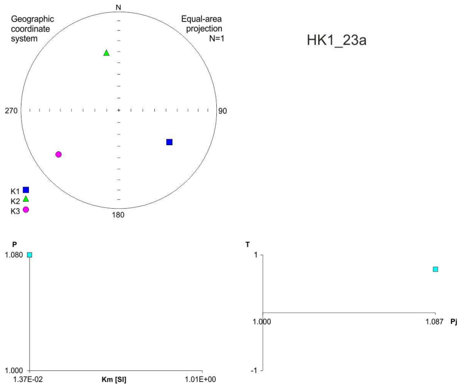

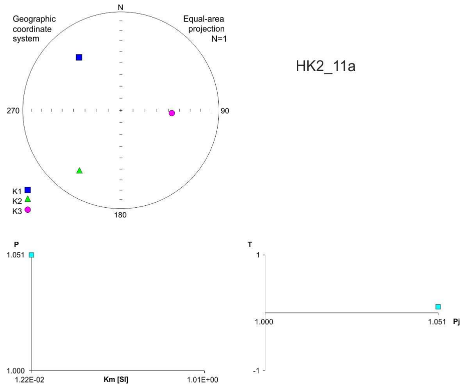

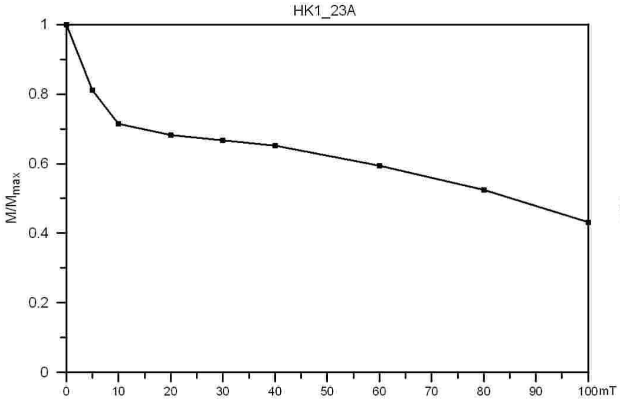

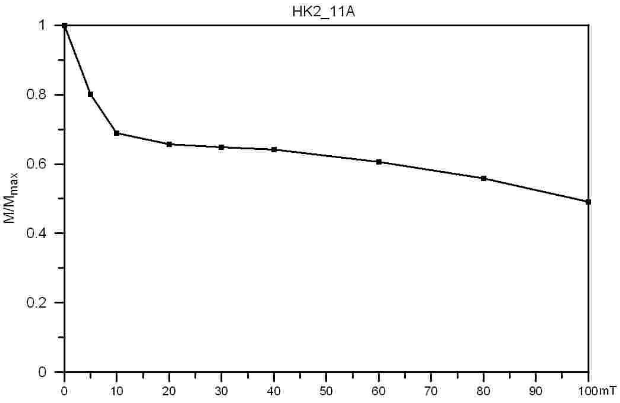

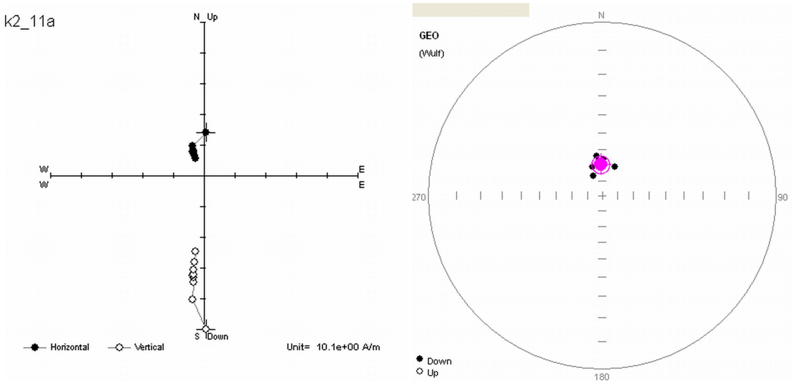

HK2_11A: MDF = 97,1 MT

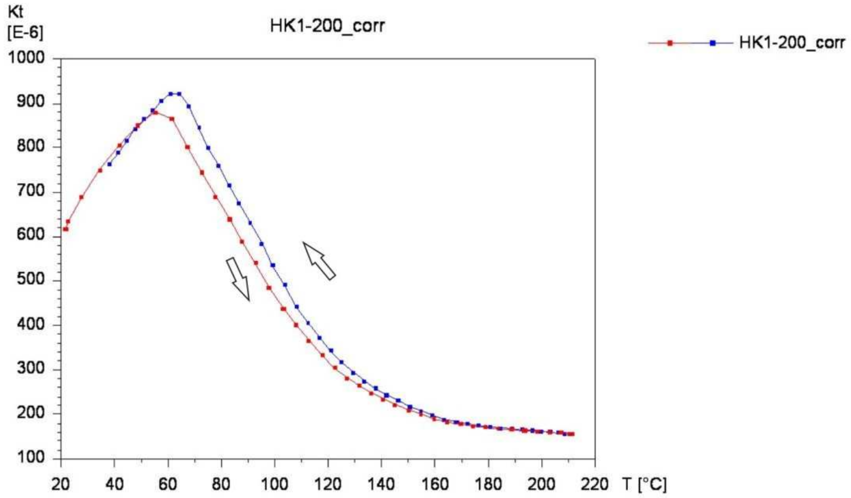

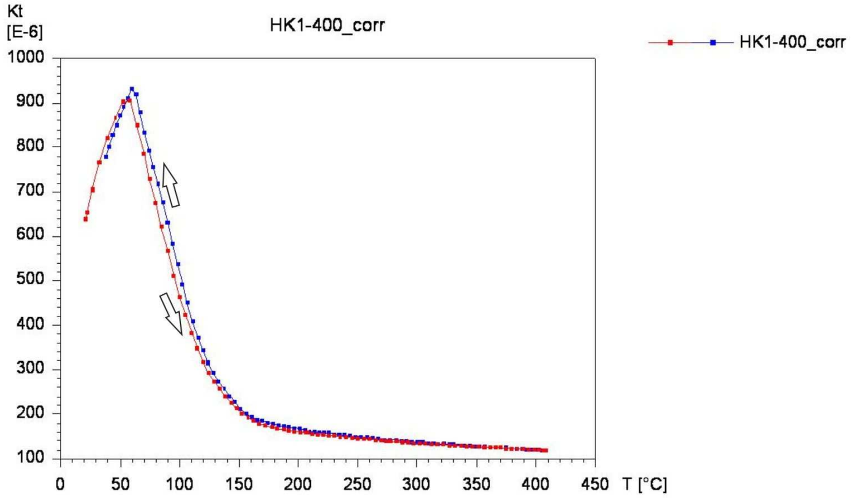

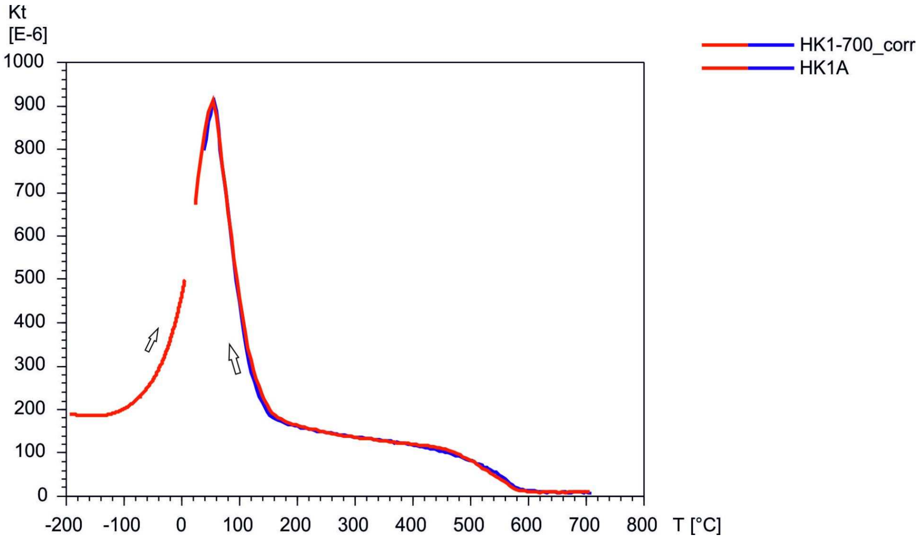

Hnaushraun HNH

HNH1_12A Alteration type 2

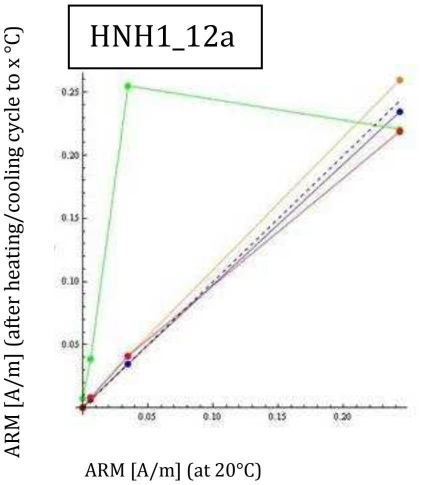

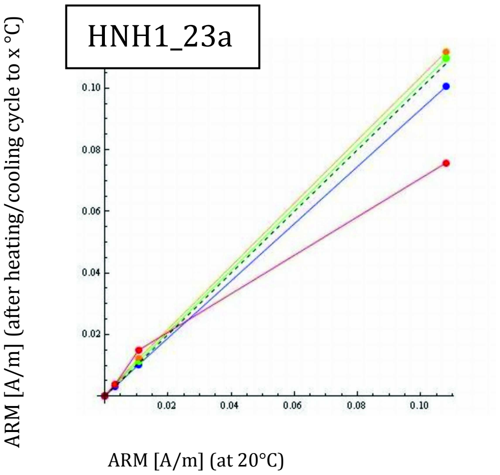

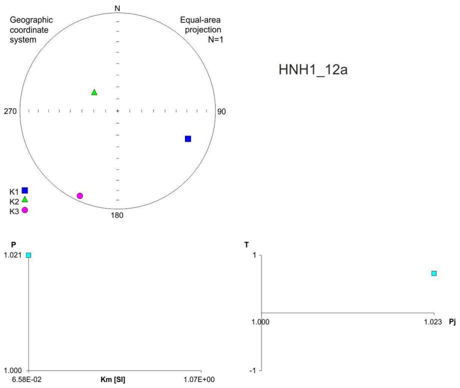

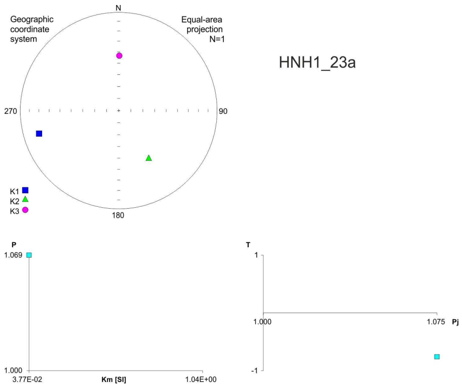

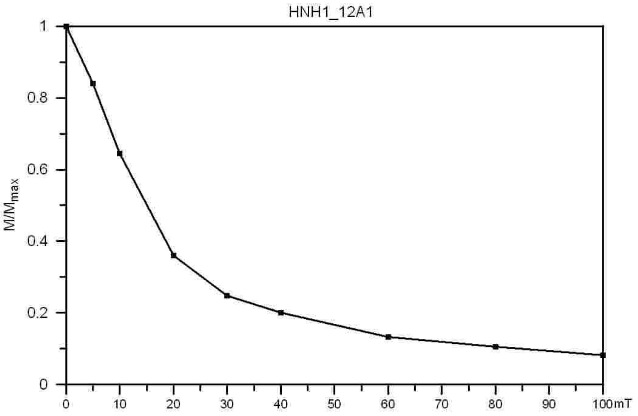
HNH1_12A1
1
0.8
0.6
0.4
0.2
0
M/M$_{max}$
0
10
20
30
40
50
60
70
80
90
100mT

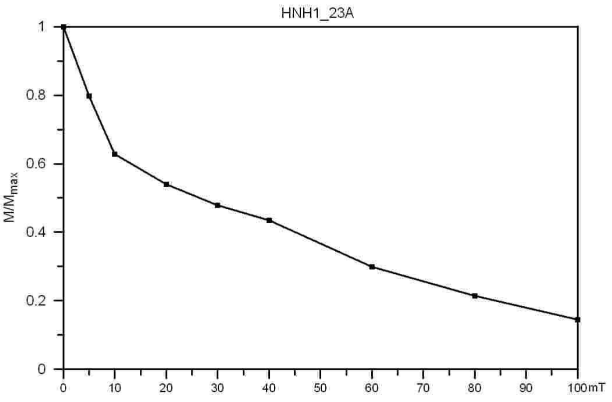
HNH1_23A
1
0.8
0.6
0.4
0.2
0
M/M$_{max}$
0
10
20
30
40
50
60
70
80
90
100mT

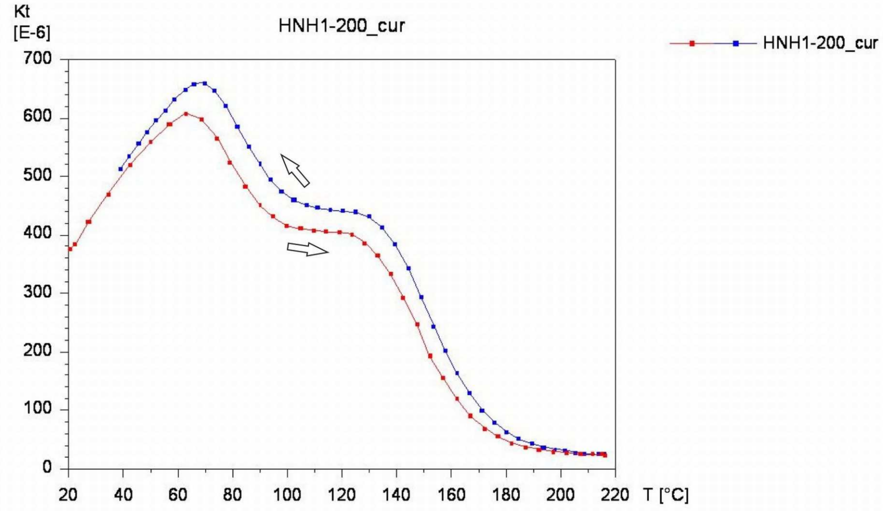
Kt
[E-6]
HNH1-200_cur
HNH1-200_cur
700
600
500
400
300
200
100
0
20
40
60
80
100
120
140
160
180
200
220
T [°C]

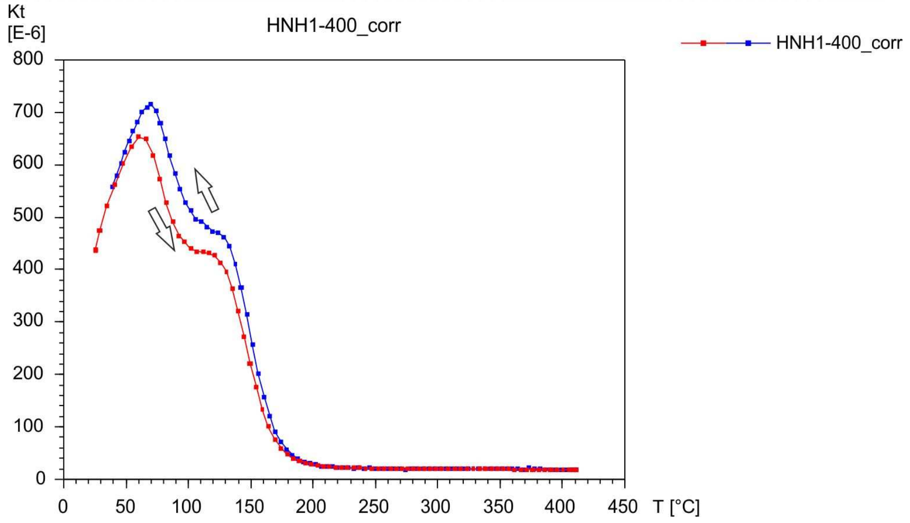
Kt
[E-6]
HNH1-400_corr
HNH1-400_corr
800
700
600
500
400
300
200
100
0
0
50
100
150
200
250
300
350
400
450
T [°C]

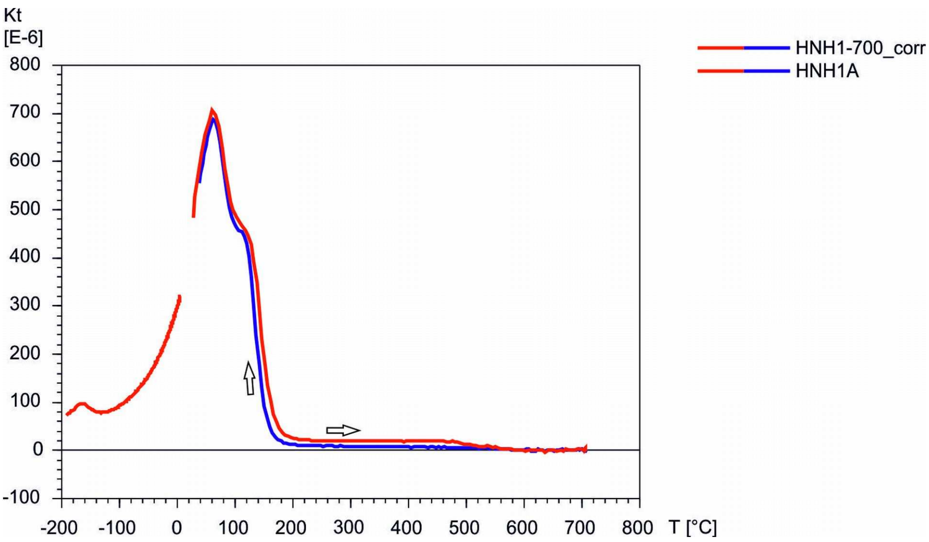

Prestahraun/Væjuhraun PV

PV1_11A

Alteration type 2

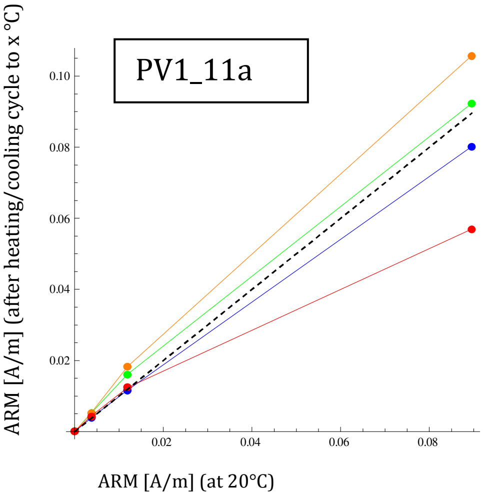

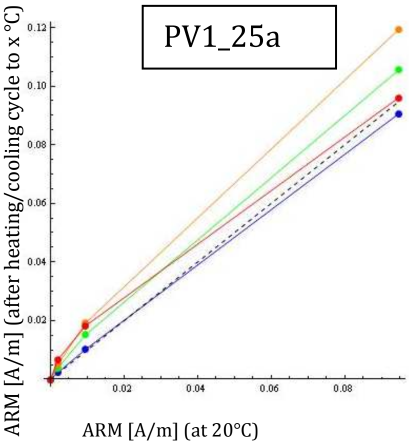

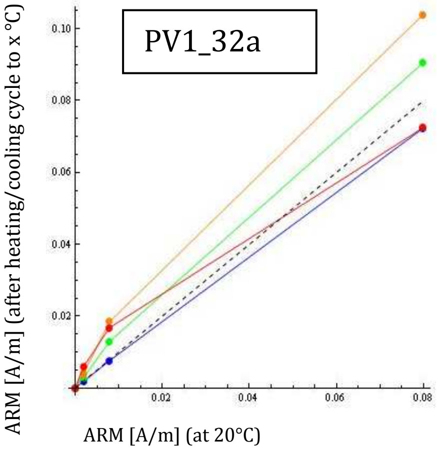

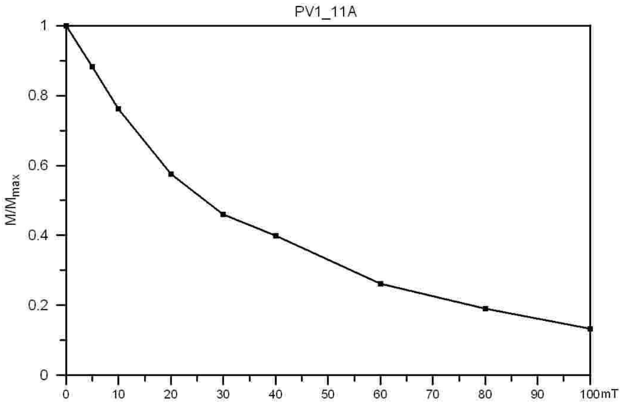

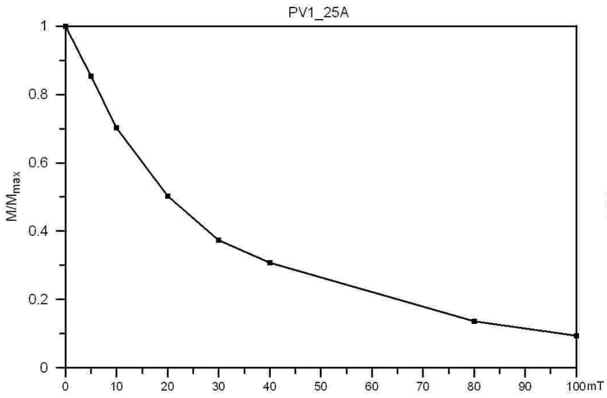
PV1_25A
M/M$_{max}$
1
0.8
0.6
0.4
0.2
0
0
10
20
30
40
50
60
70
80
90
100mT

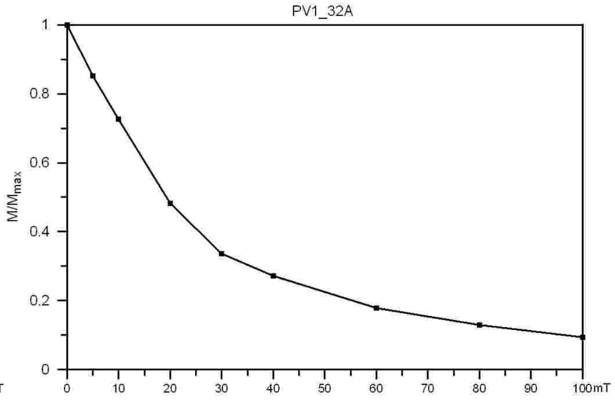
PV1_32A
M/M$_{max}$
1
0.8
0.6
0.4
0.2
0
0
10
20
30
40
50
60
70
80
90
100mT

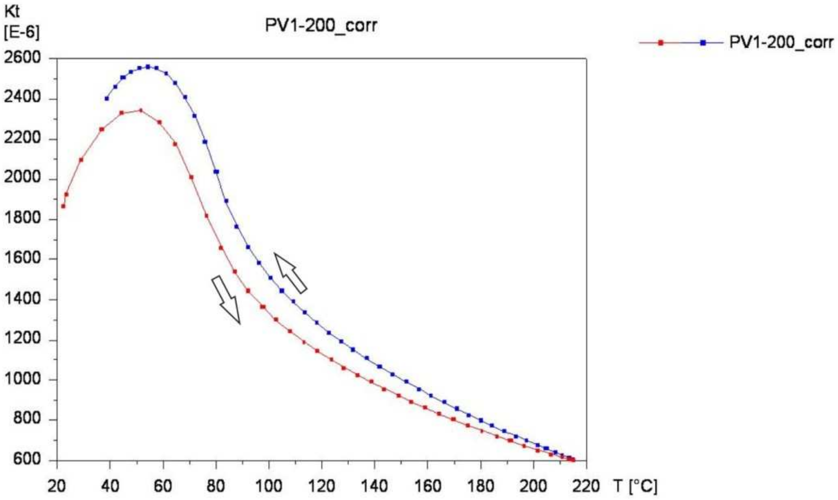
Kt
[E-6]
PV1-200_corr
PV1-200_corr
2600
2400
2200
2000
1800
1600
1400
1200
1000
800
600
20
40
60
80
100
120
140
160
180
200
220
T [°C]

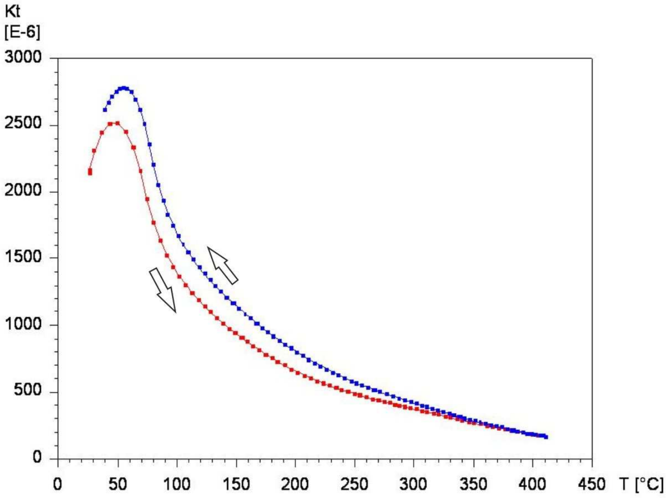
Kt
[E-6]
3000
2500
2000
1500
1000
500
0
0
50
100
150
200
250
300
350
400
450
T [°C]

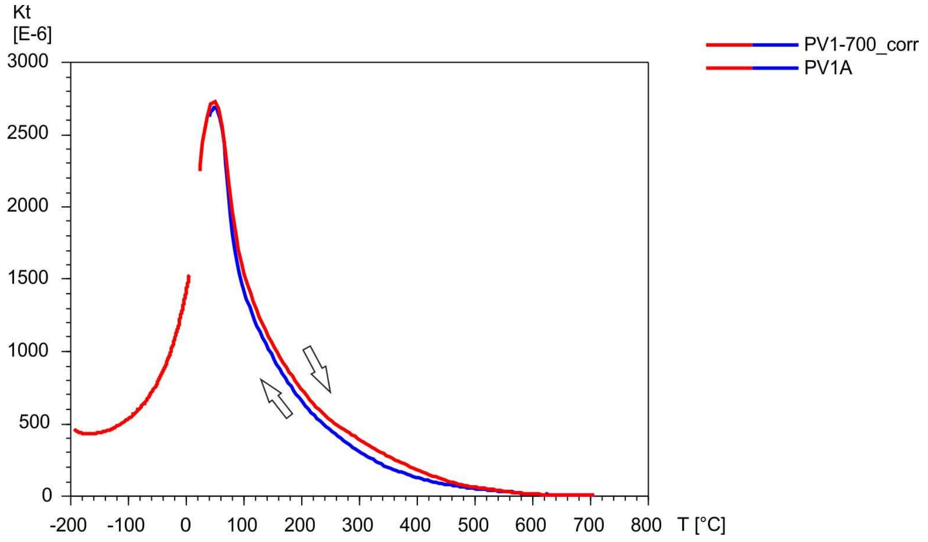

Sandarhraun SAH

SAH2_11A

Alteration type 3

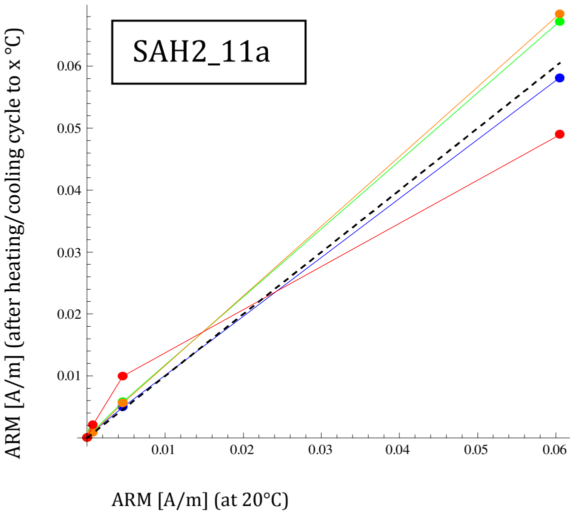

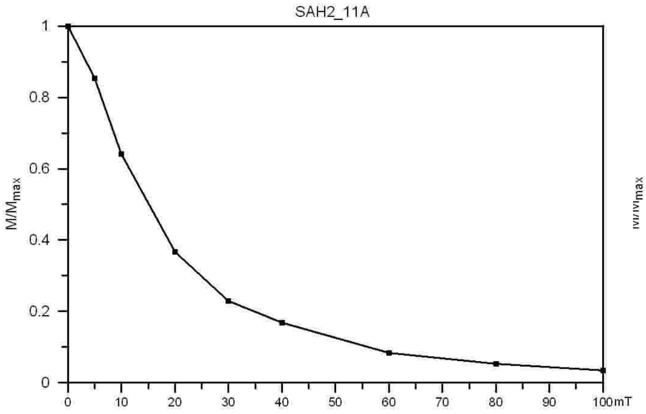
SAH2_11A
M/M$_{max}$
1
0.8
0.6
0.4
0.2
0
0
10
20
30
40
50
60
70
80
90
100mT

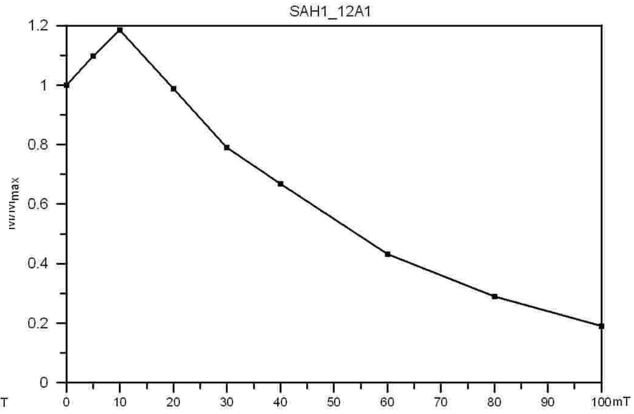
SAH1_12A1
M/M$_{max}$
1.2
1
0.8
0.6
0.4
0.2
0
0
10
20
30
40
50
60
70
80
90
100mT

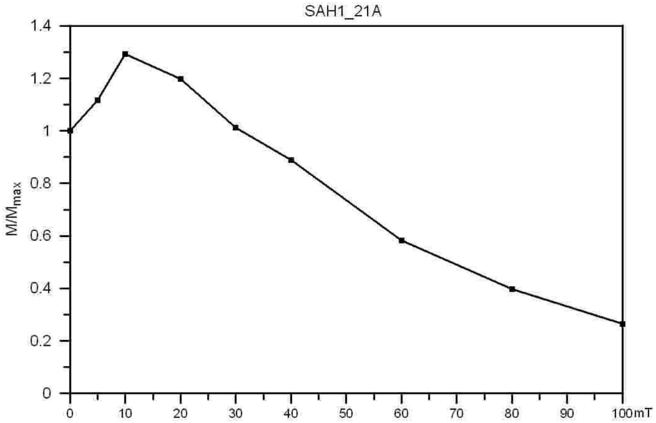
SAH1_21A
M/M$_{max}$
1.4
1.2
1
0.8
0.6
0.4
0.2
0
0
10
20
30
40
50
60
70
80
90
100mT

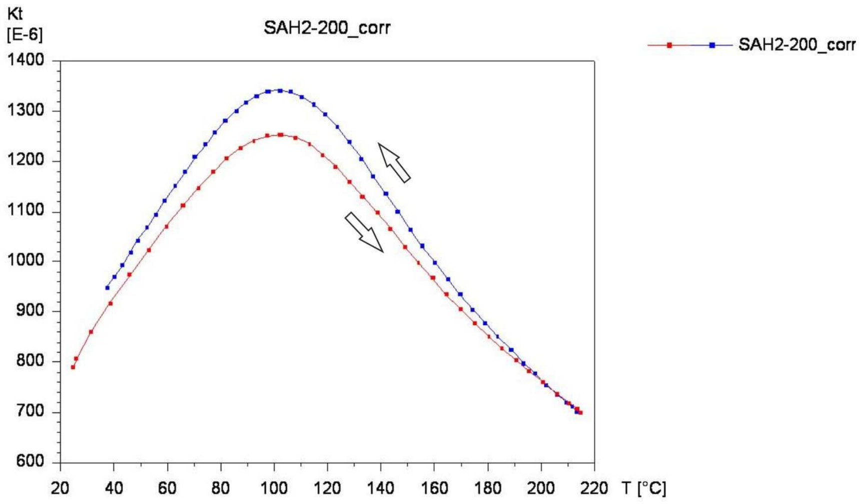
Kt
[E-6]
SAH2-200_corr
SAH2-200_corr
1400
1300
1200
1100
1000
900
800
700
600
20
40
60
80
100
120
140
160
180
200
220
T [°C]

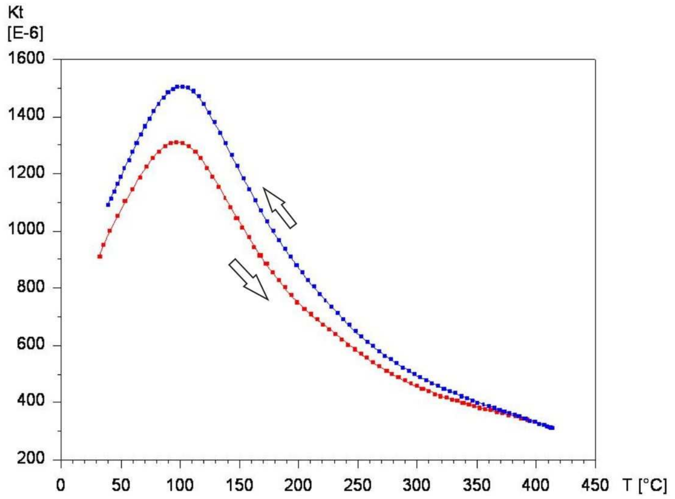

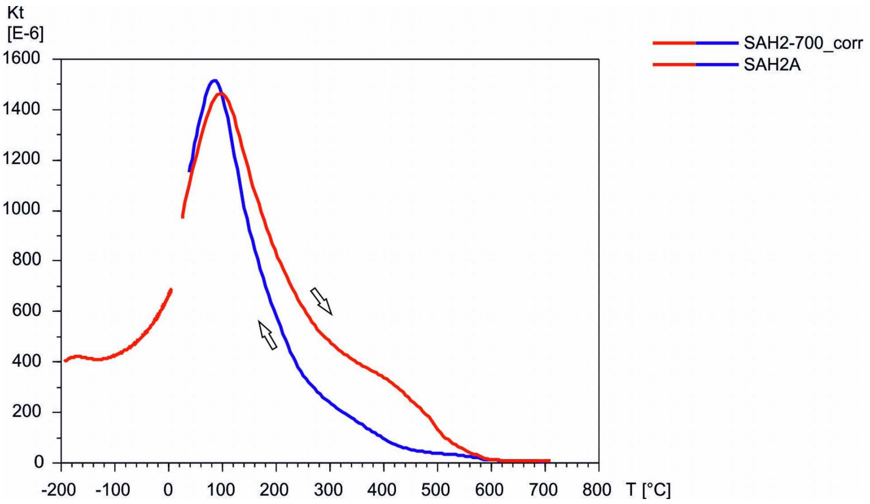

Buđahraun BDH

BDH1_21A Alteration type 4

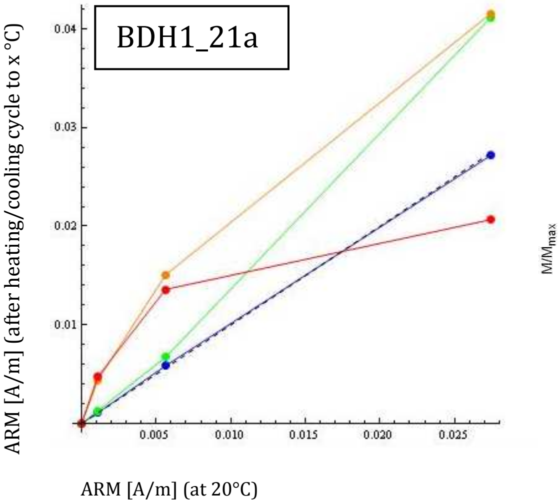

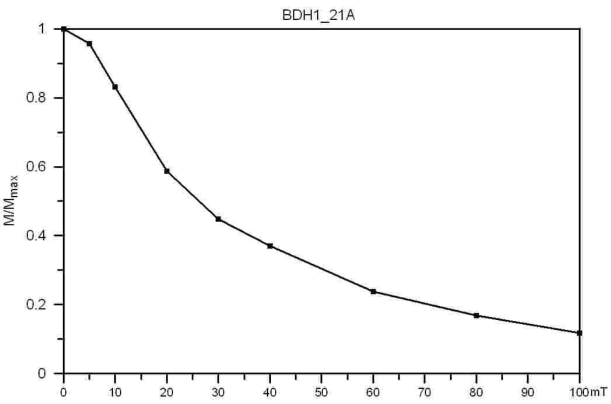

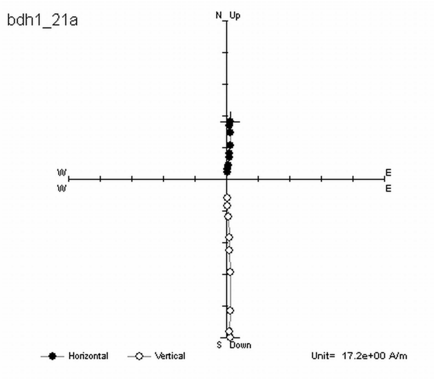
bdh1_21a
N Up
W
W
E
E
S Down
Horizontal
Vertical
Unit= 17.2e+00 A/m

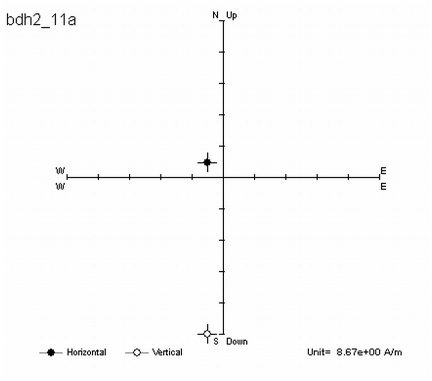
bdh2_11a
N Up
W
W
E
E
S Down
Horizontal
Vertical
Unit= 8.67e+00 A/m

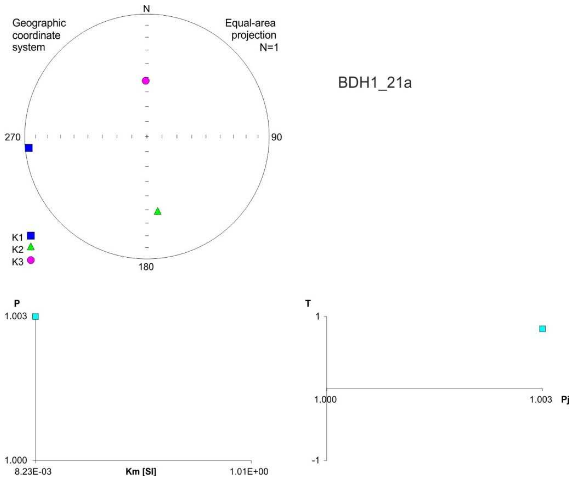
Geographic coordinate system
N
Equal-area projection N=1
BDH1_21a
270
90
180
K1
K2
K3
P
1.003
1.000
8.23E-03
Km [SI]
1.01E+00
T
1
1.000
1.003
Pj
-1

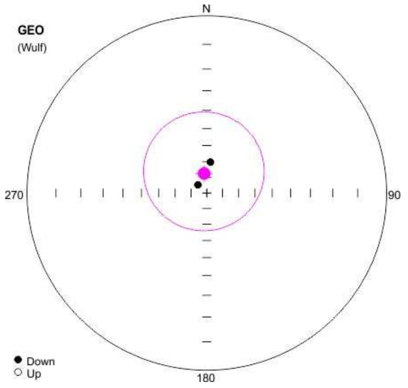
GEO
(Wulf)
N
270
90
180
Down
Up

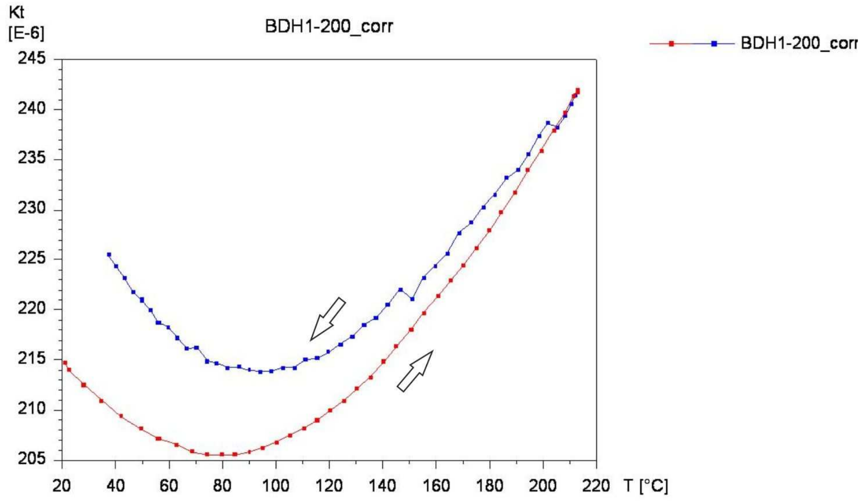
Kt
[E-6]
BDH1-200_corr
245
240
235
230
225
220
215
210
205
20
40
60
80
100
120
140
160
180
200
220
T [°C]
BDH1-200_corr

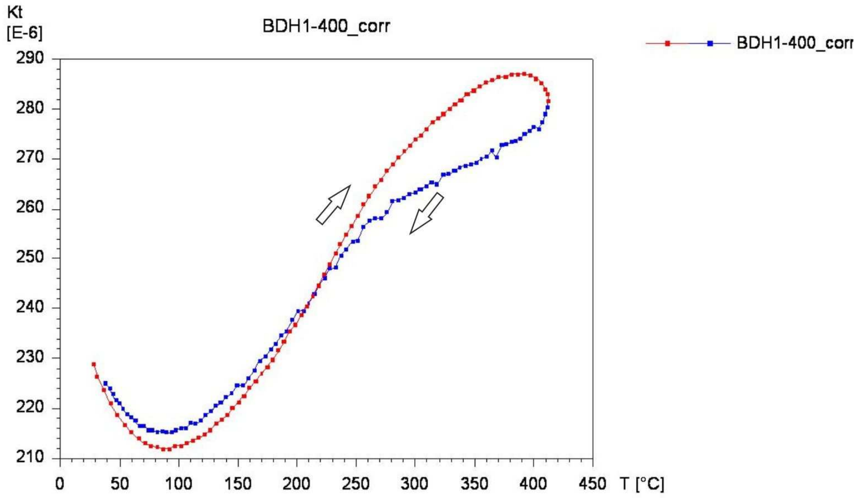

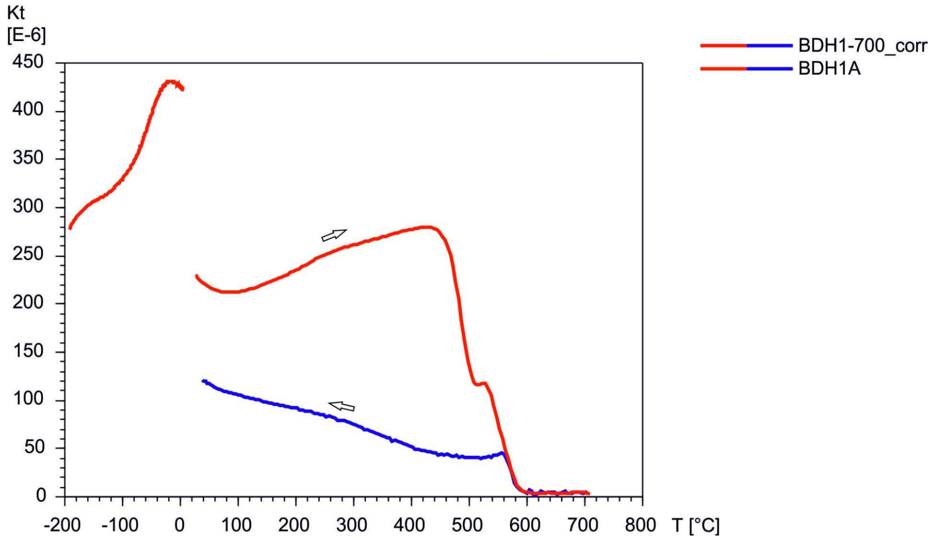

Berserkjahraun BSH

BSH1_12A

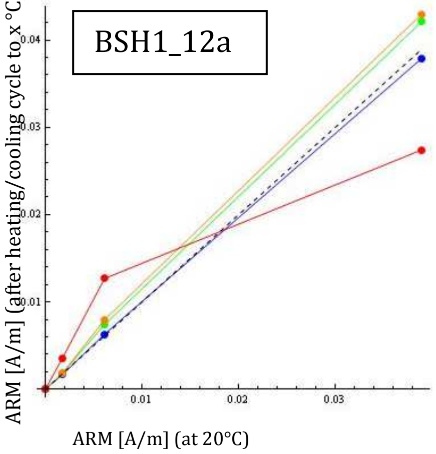

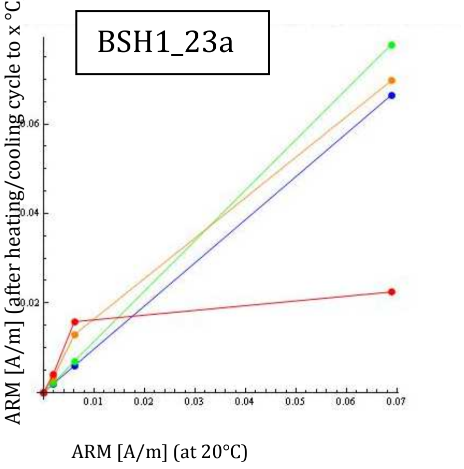

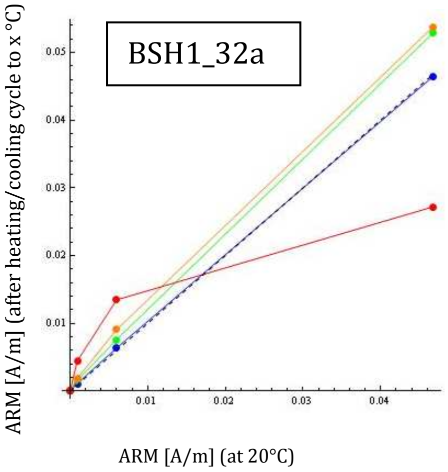
BSH1_32a
ARM [A/m] (after heating/cooling cycle to x °C)
0.05
0.04
0.03
0.02
0.01
0.01
0.02
0.03
0.04
ARM [A/m] (at 20°C)

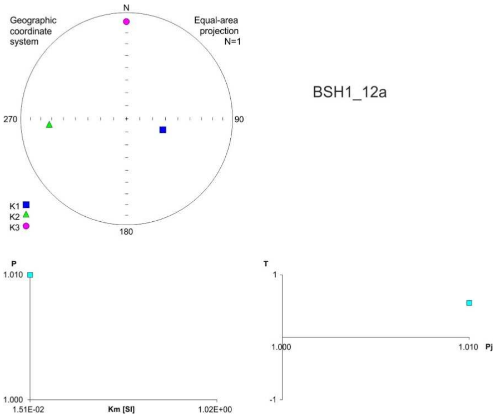
Geographic coordinate system
N
Equal-area projection N=1
270
90
180
K1 ■
K2 ▲
K3 ●
BSH1_12a
P
1.010
1.000
1.51E-02
Km [SI]
1.02E+00
T
1
1.000
1.010
Pj
-1

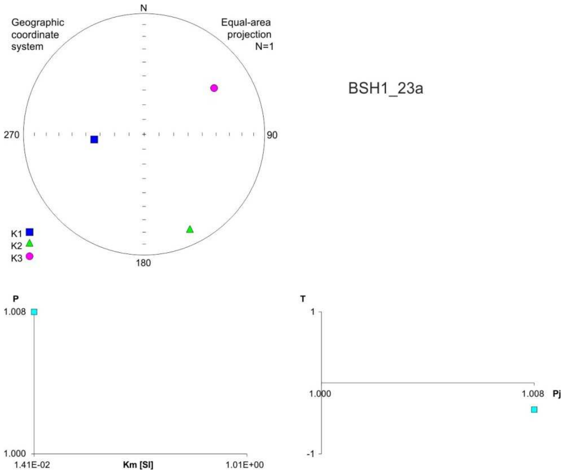
Geographic coordinate system
N
Equal-area projection N=1
270
90
180
K1 ■
K2 ▲
K3 ●
BSH1_23a
P
1.008
1.000
1.41E-02
Km [SI]
1.01E+00
T
1
1.000
1.008
Pj
-1

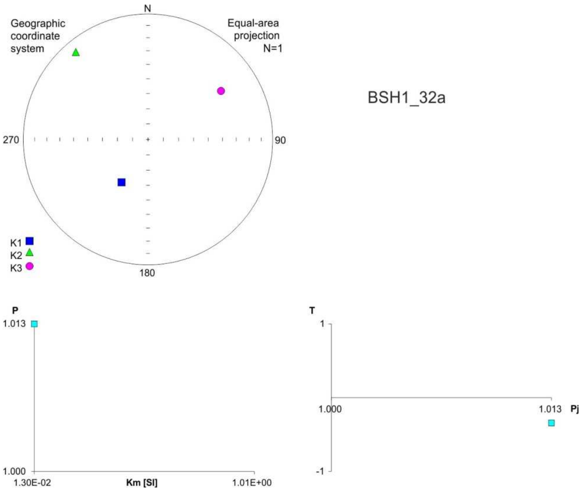
Geographic coordinate system
N
Equal-area projection N=1
270
90
180
K1 ■
K2 ▲
K3 ●
BSH1_32a
P
1.013
1.000
1.30E-02
Km [SI]
1.01E+00
T
1
1.000
1.013
Pj
-1

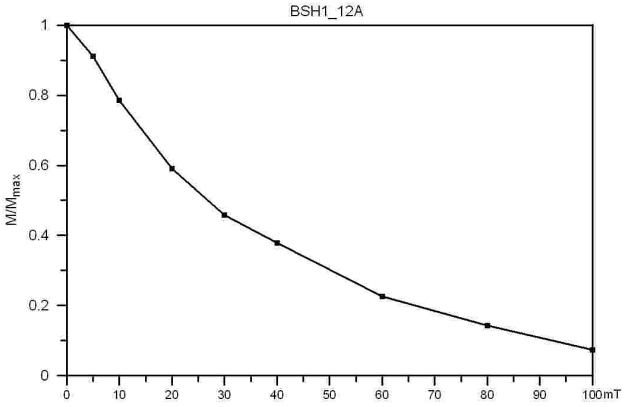
BSH1_12A
M/M$_{max}$
1
0.8
0.6
0.4
0.2
0
0
10
20
30
40
50
60
70
80
90
100mT

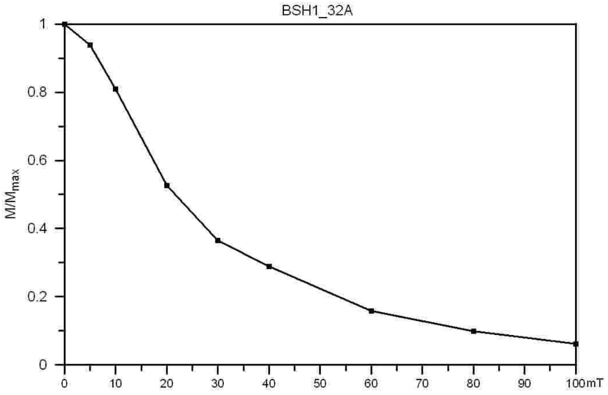
BSH1_32A
M/M$_{max}$
1
0.8
0.6
0.4
0.2
0
0
10
20
30
40
50
60
70
80
90
100mT

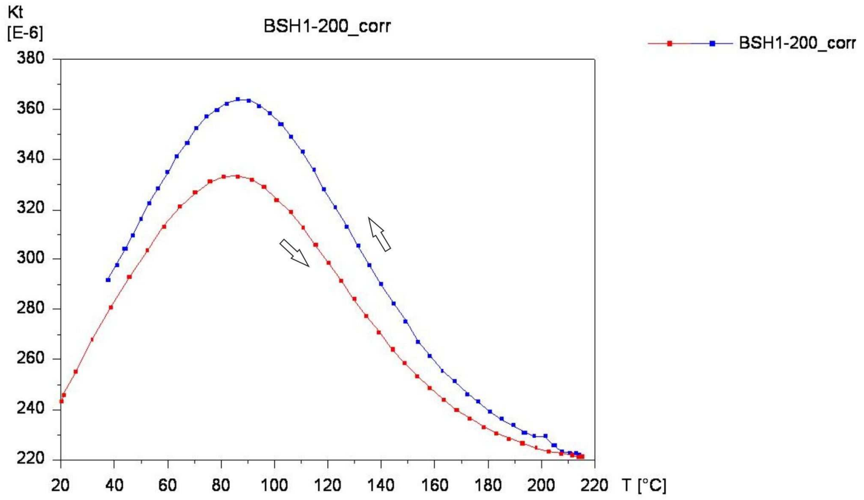
Kt
[E-6]
BSH1-200_corr
BSH1-200_corr
380
360
340
320
300
280
260
240
220
20
40
60
80
100
120
140
160
180
200
220
T [°C]

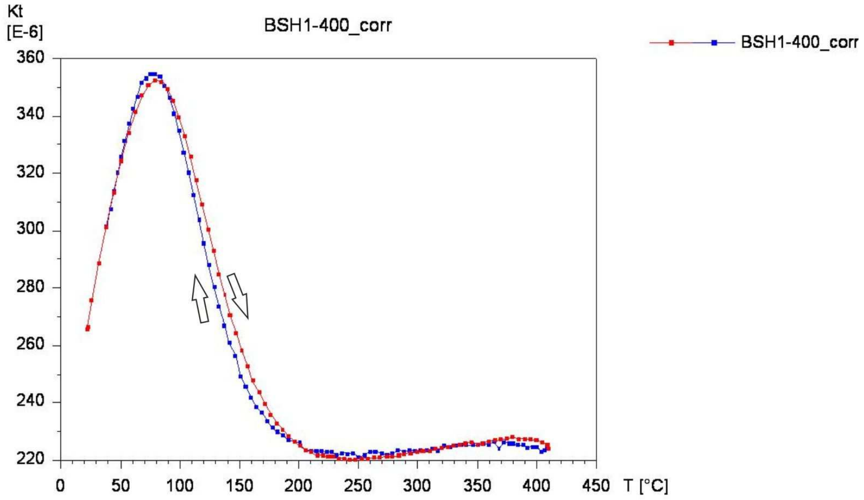
Kt
[E-6]
BSH1-400_corr
BSH1-400_corr
360
340
320
300
280
260
240
220
0
50
100
150
200
250
300
350
400
450
T [°C]

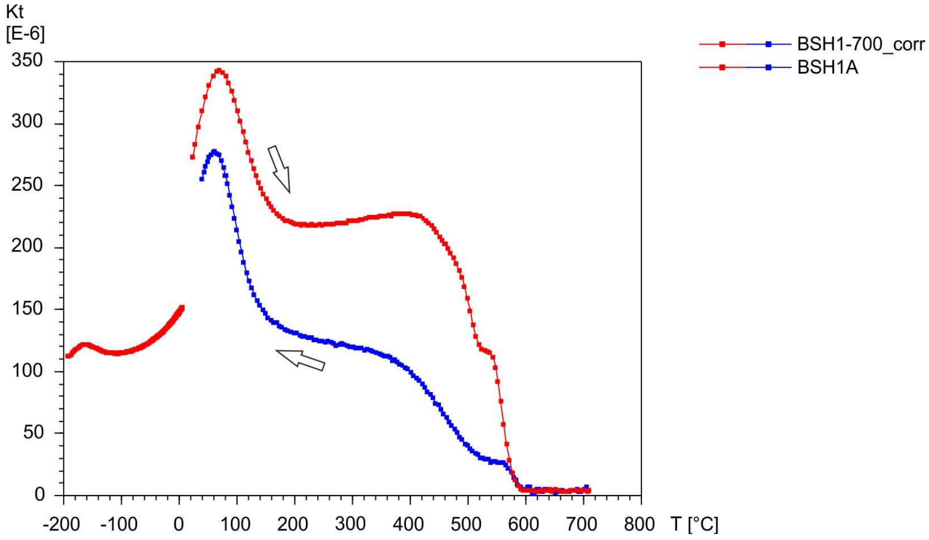
Kt
[E-6]
BSH1-700_corr
BSH1A
350
300
250
200
150
100
50
0
-200
-100
0
100
200
300
400
500
600
700
800
T [°C]

Neshraun NSH

NSH1_12A

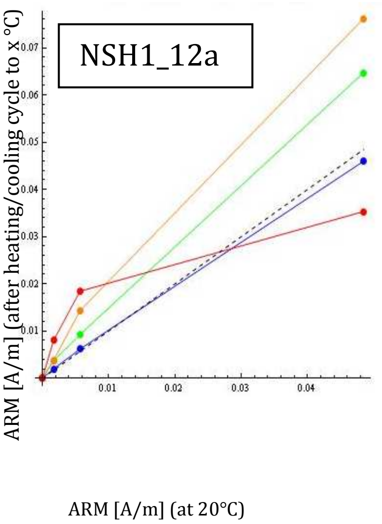

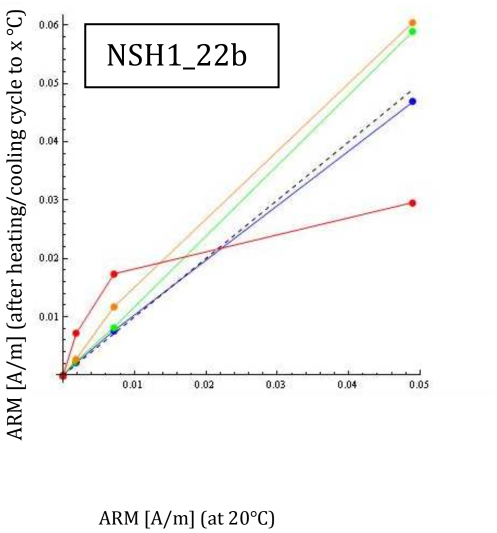

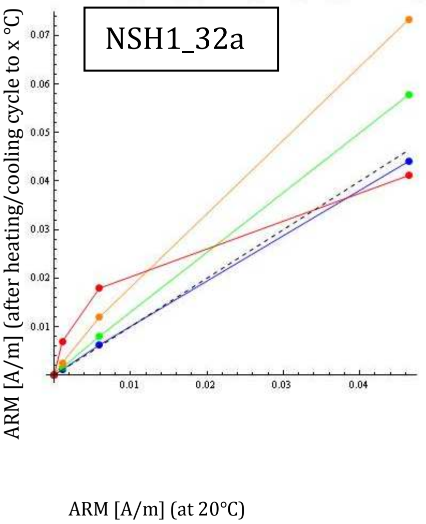

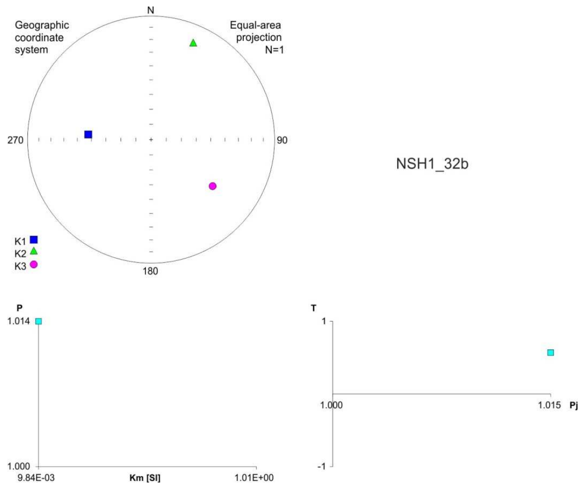

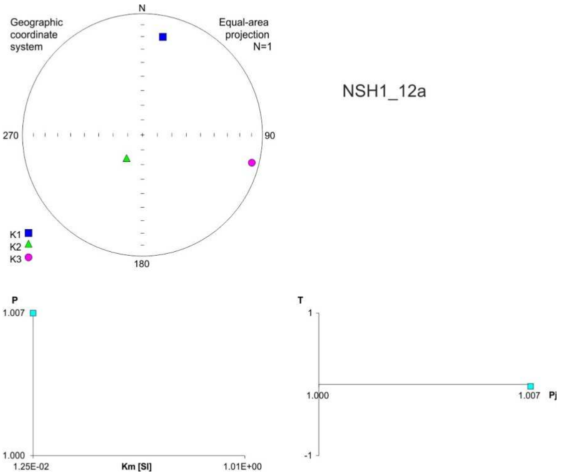

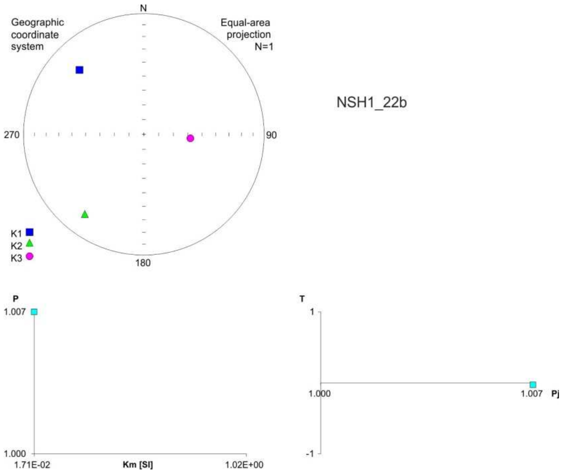

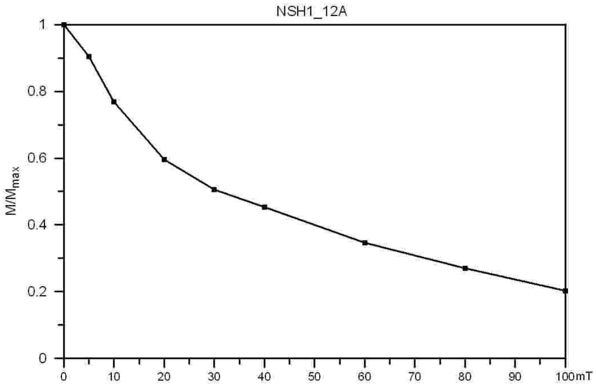
NSH1_12A
M/M$_{max}$
1
0.8
0.6
0.4
0.2
0
0
10
20
30
40
50
60
70
80
90
100mT

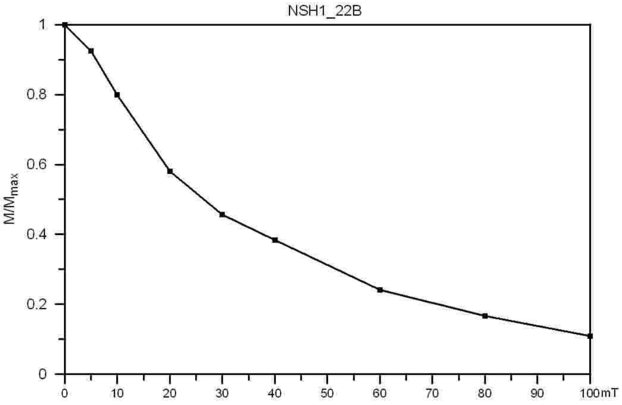
NSH1_22B
M/M$_{max}$
1
0.8
0.6
0.4
0.2
0
0
10
20
30
40
50
60
70
80
90
100mT

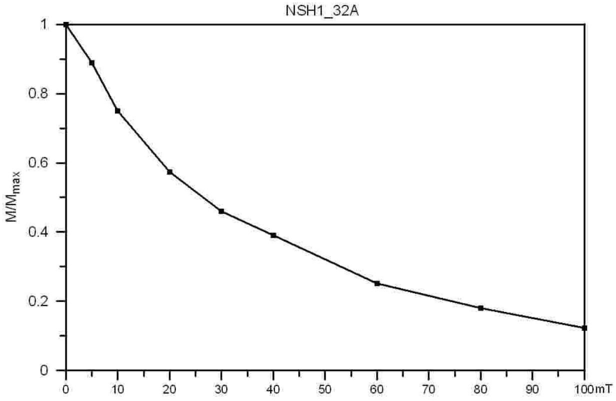
NSH1_32A
M/M$_{max}$
1
0.8
0.6
0.4
0.2
0
0
10
20
30
40
50
60
70
80
90
100mT

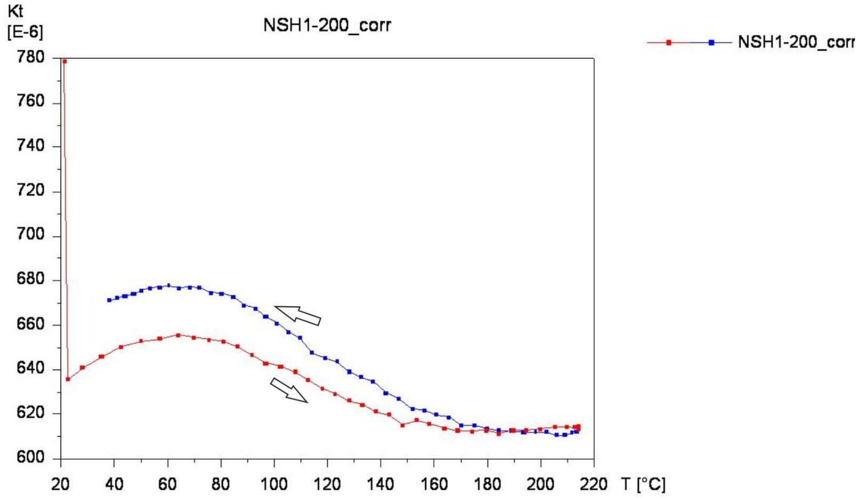
Kt
[E-6]
NSH1-200_corr
NSH1-200_corr
780
760
740
720
700
680
660
640
620
600
20
40
60
80
100
120
140
160
180
200
220
T [°C]

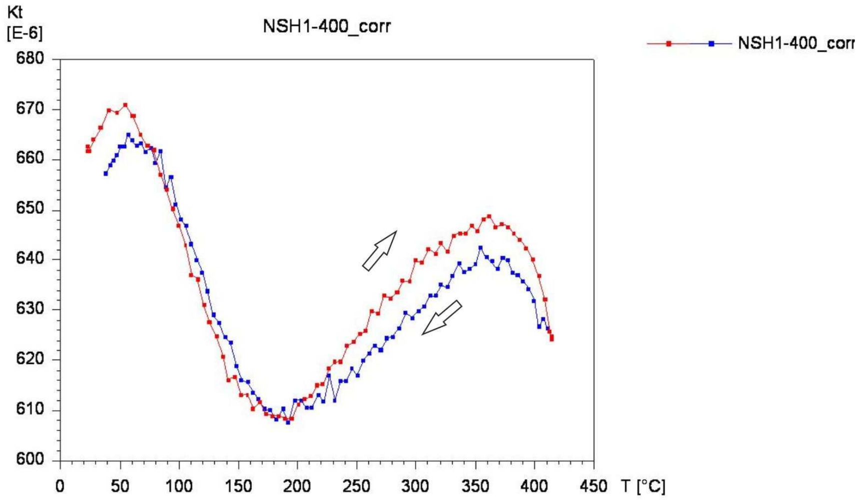
Kt
[E-6]
NSH1-400_corr
NSH1-400_corr
680
670
660
650
640
630
620
610
600
0
50
100
150
200
250
300
350
400
450
T [°C]

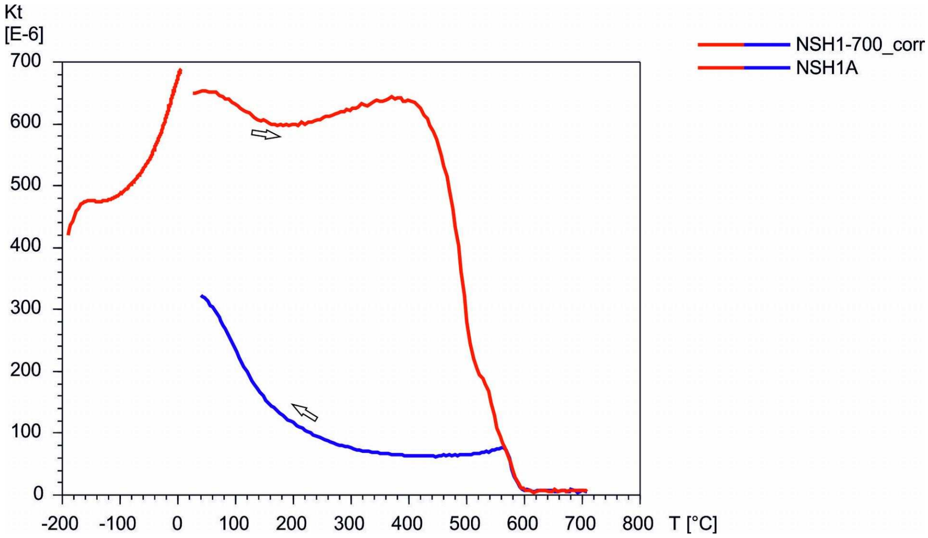
Kt
[E-6]
NSH1-700_corr
NSH1A
700
600
500
400
300
200
100
0
-200
-100
0
100
200
300
400
500
600
700
800
T [°C]

Burstahraun BUH

BUH1_13A

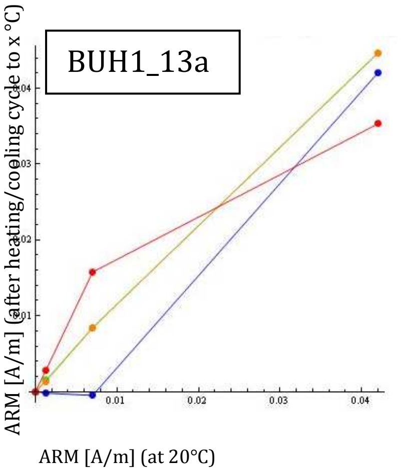

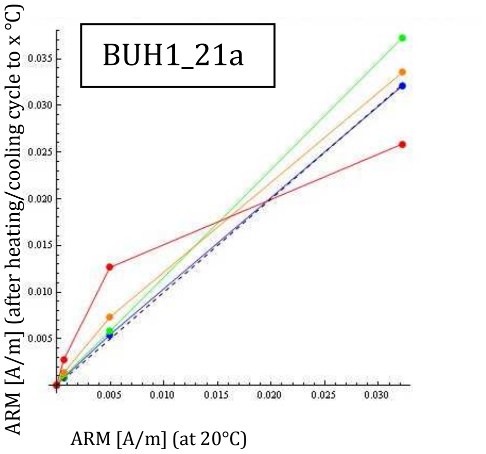

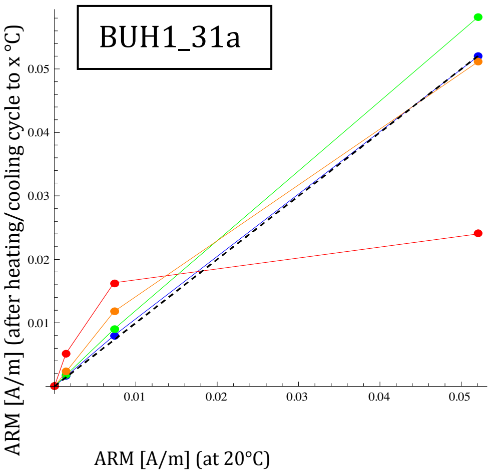

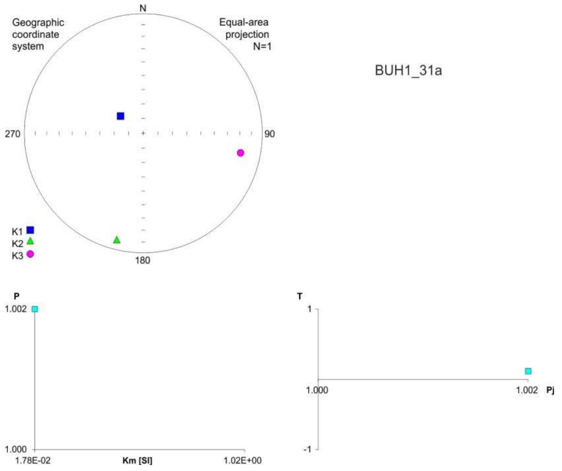

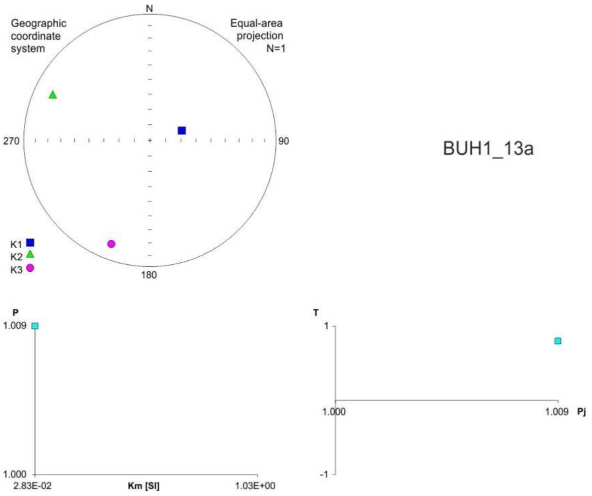

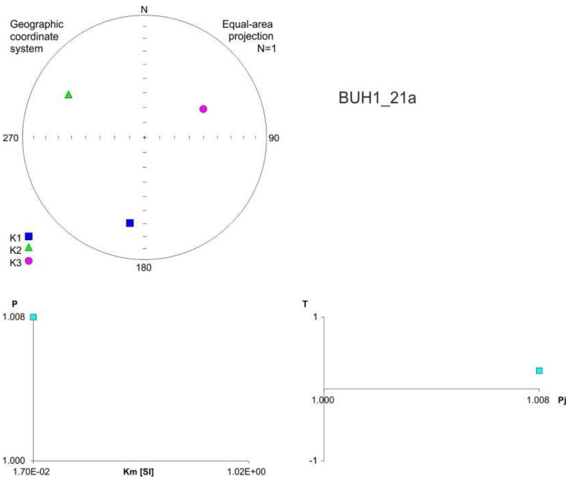

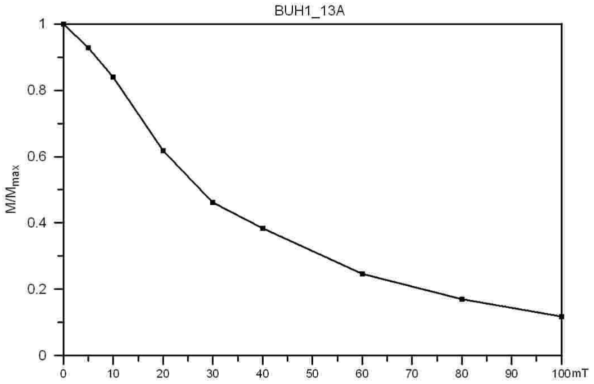
BUH1_13A
M/M$_{max}$
1
0.8
0.6
0.4
0.2
0
0
10
20
30
40
50
60
70
80
90
100mT

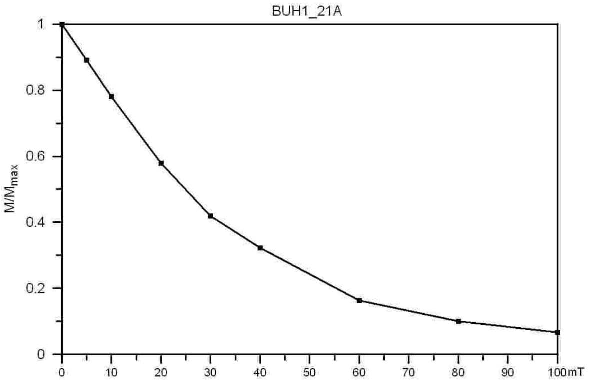
BUH1_21A
M/M$_{max}$
1
0.8
0.6
0.4
0.2
0
0
10
20
30
40
50
60
70
80
90
100mT

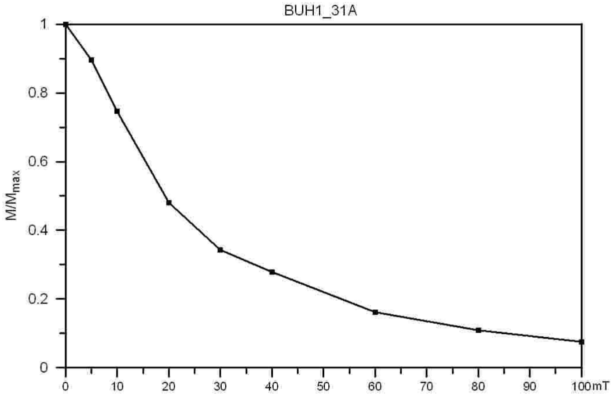
BUH1_31A
M/M$_{max}$
1
0.8
0.6
0.4
0.2
0
0
10
20
30
40
50
60
70
80
90
100mT

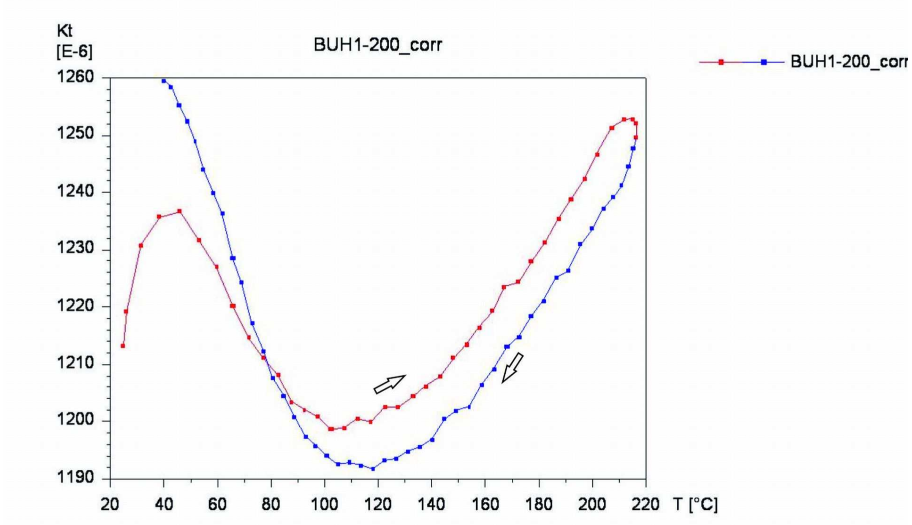
Kt
[E-6]
BUH1-200_corr
BUH1-200_corr
1260
1250
1240
1230
1220
1210
1200
1190
20
40
60
80
100
120
140
160
180
200
220
T [°C]

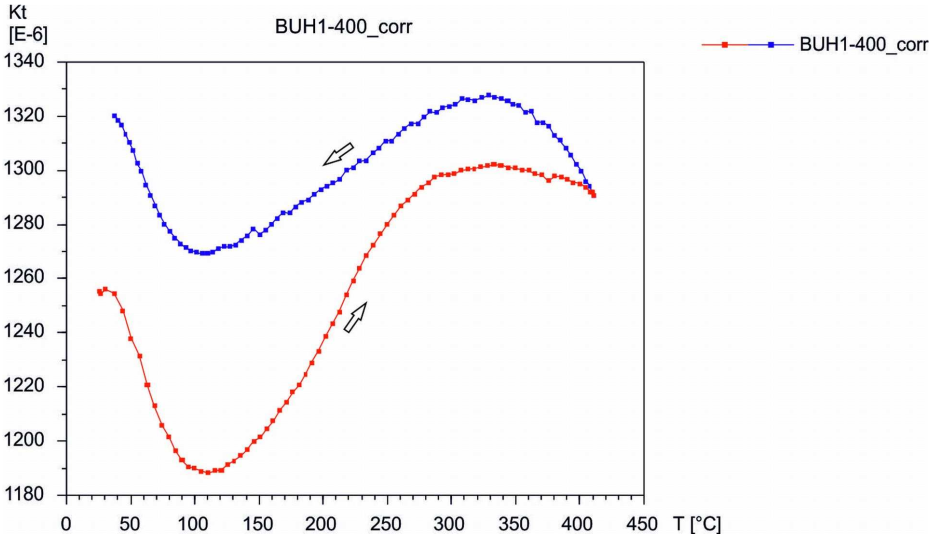
Kt
[E-6]
BUH1-400_corr
1340
1320
1300
1280
1260
1240
1220
1200
1180
0
50
100
150
200
250
300
350
400
450
T [°C]
BUH1-400_corr

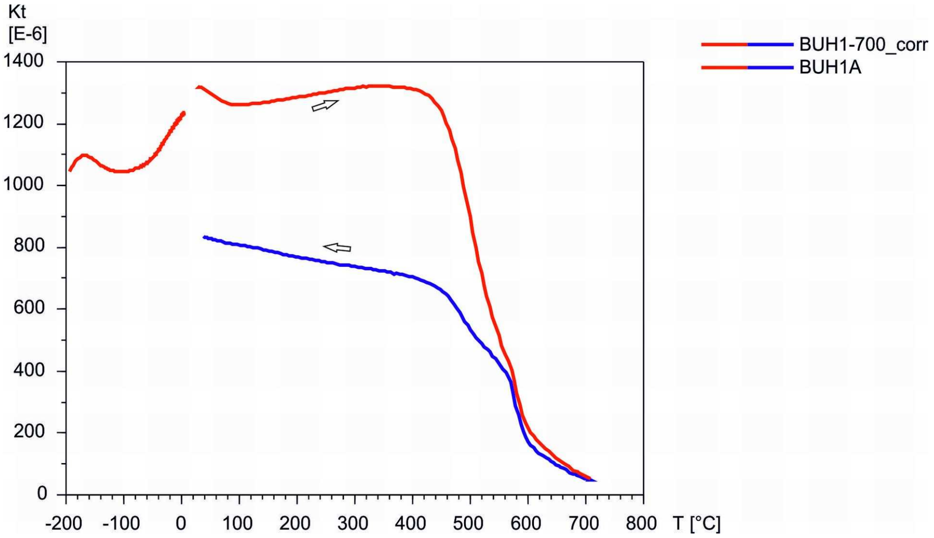
Kt
[E-6]
1400
1200
1000
800
600
400
200
0
-200
-100
0
100
200
300
400
500
600
700
800
T [°C]
BUH1-700_corr
BUH1A

Drangahraun DRH

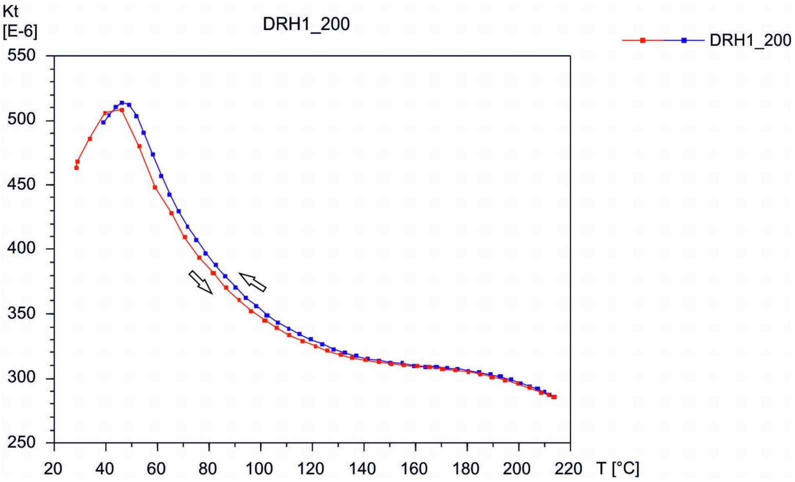

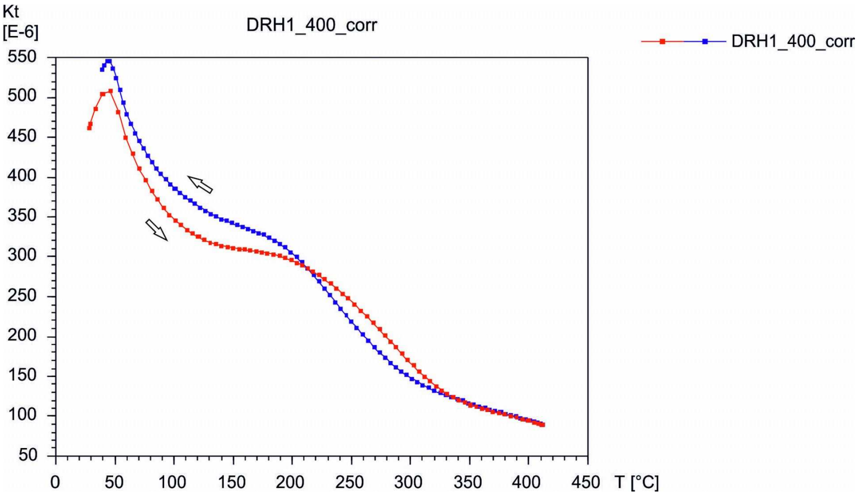

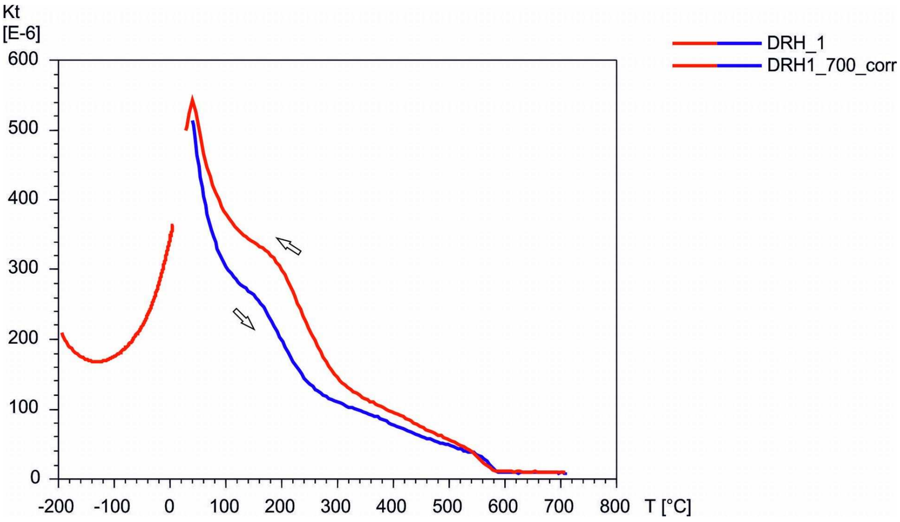

Svartahraun/Valhraun SV

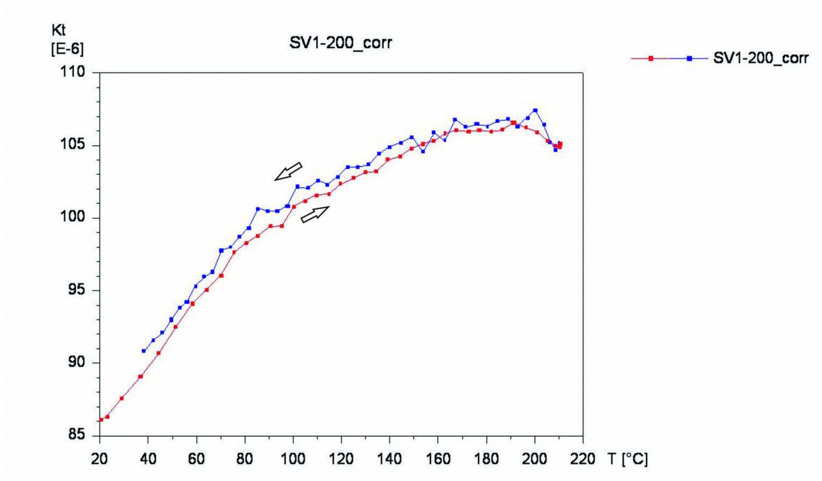

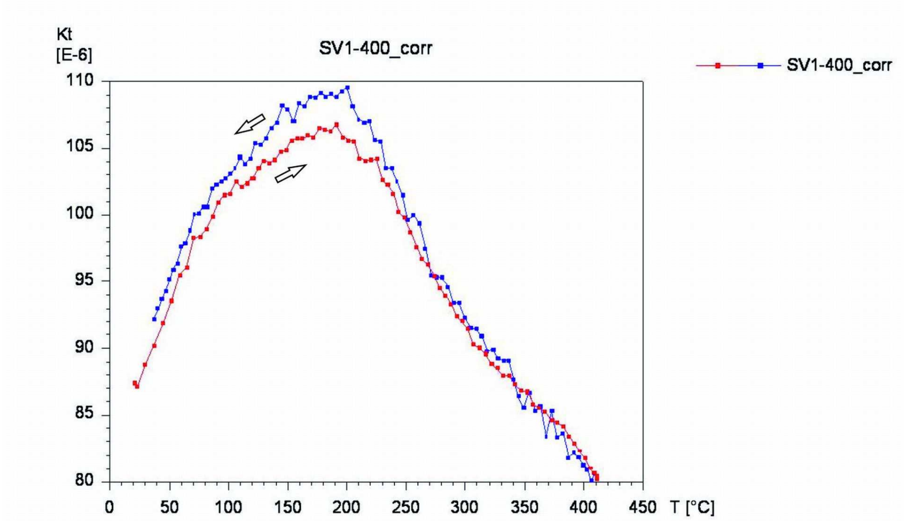

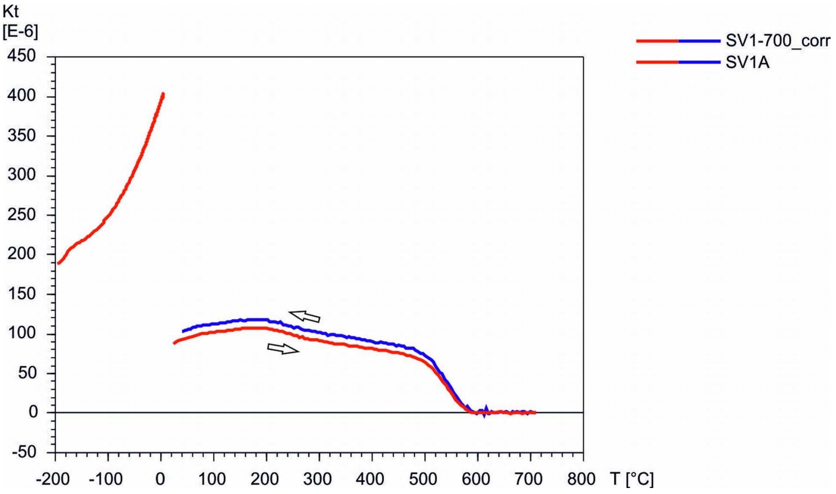

Haahraun HAH

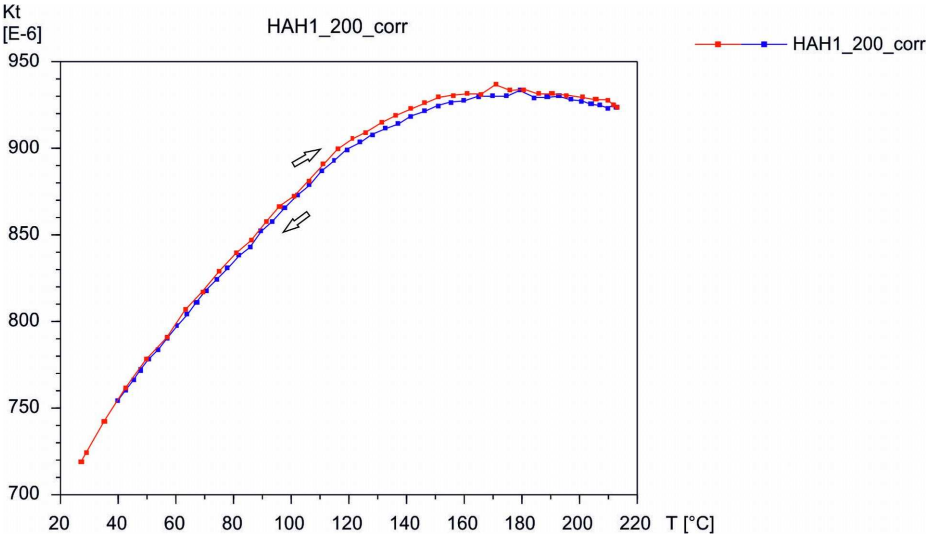

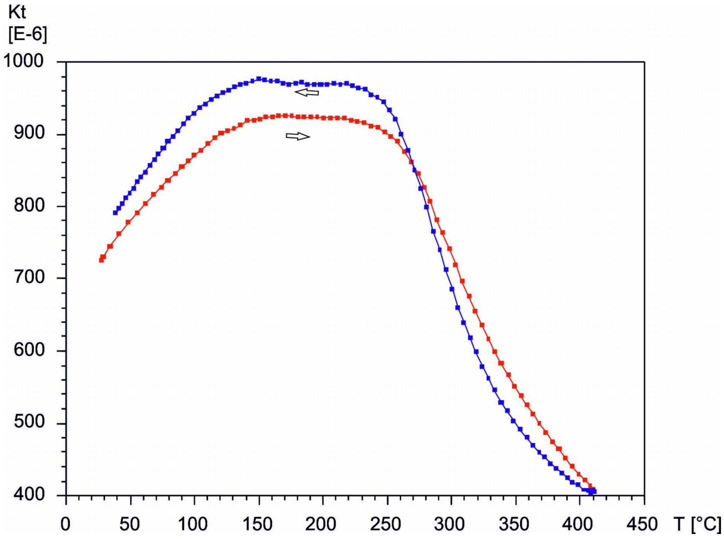

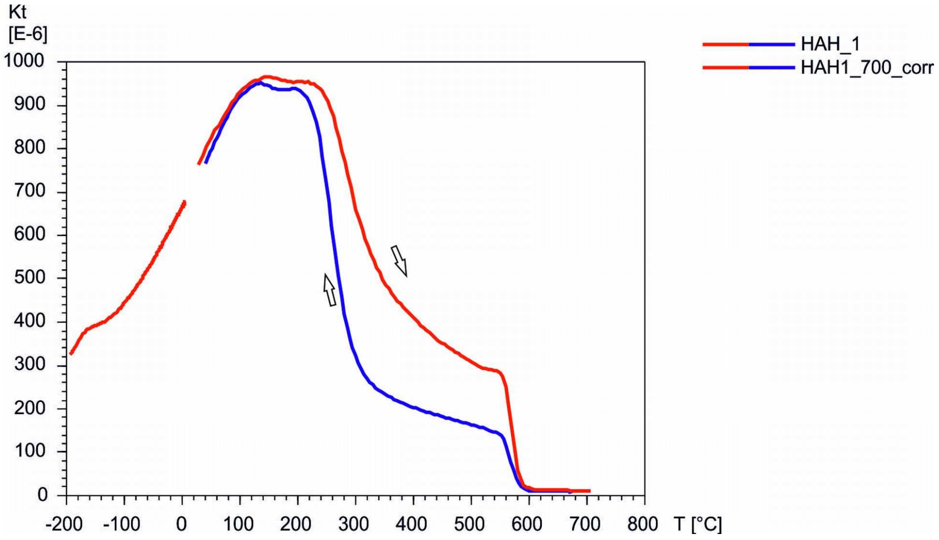

Blafeldarhraun BLH

BLH1_12A

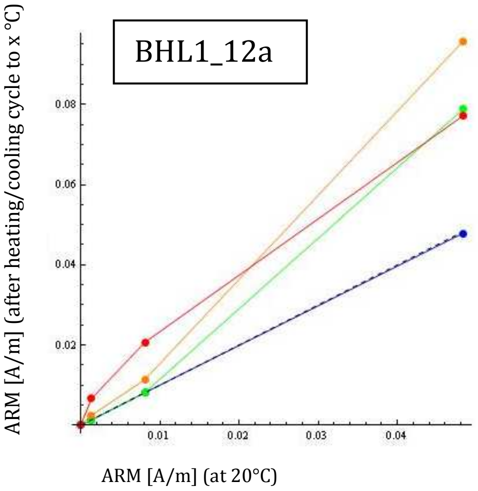

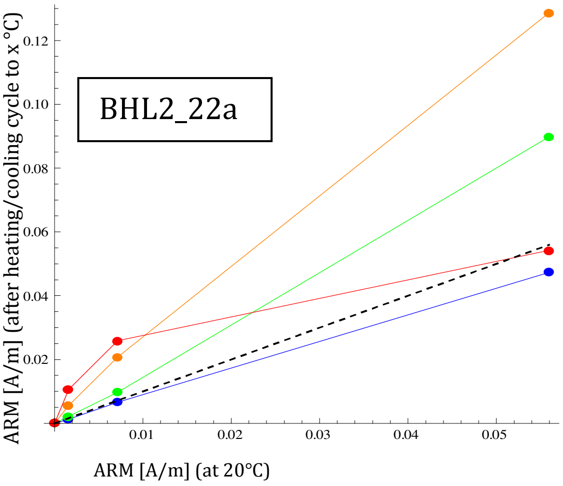

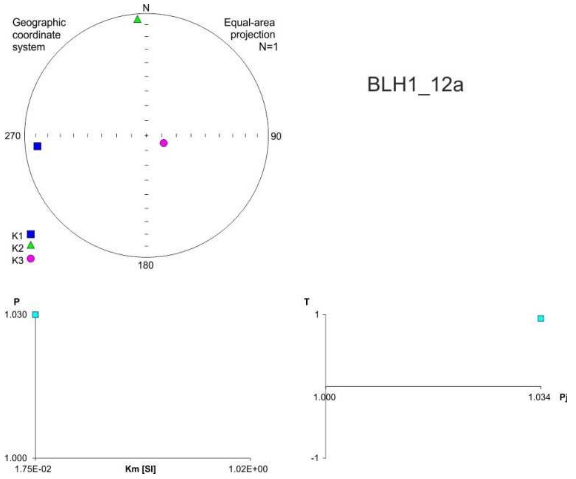

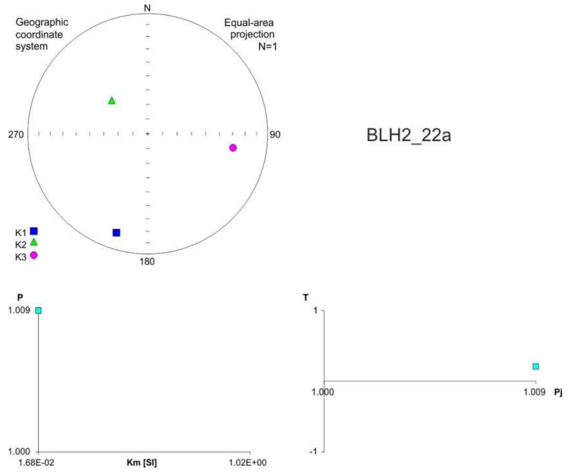

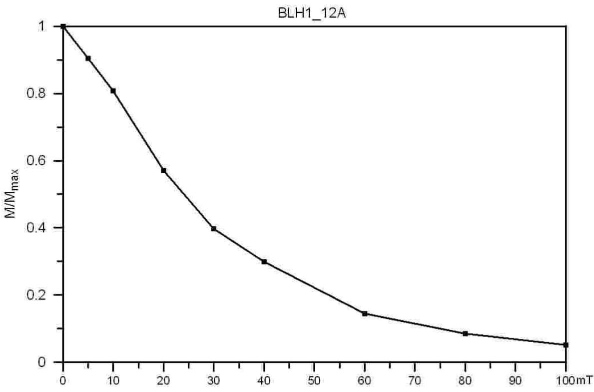

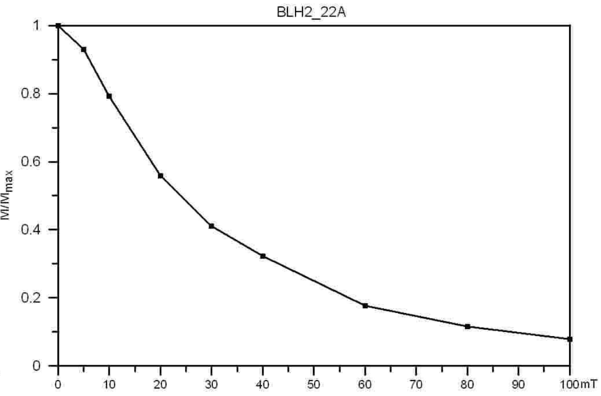

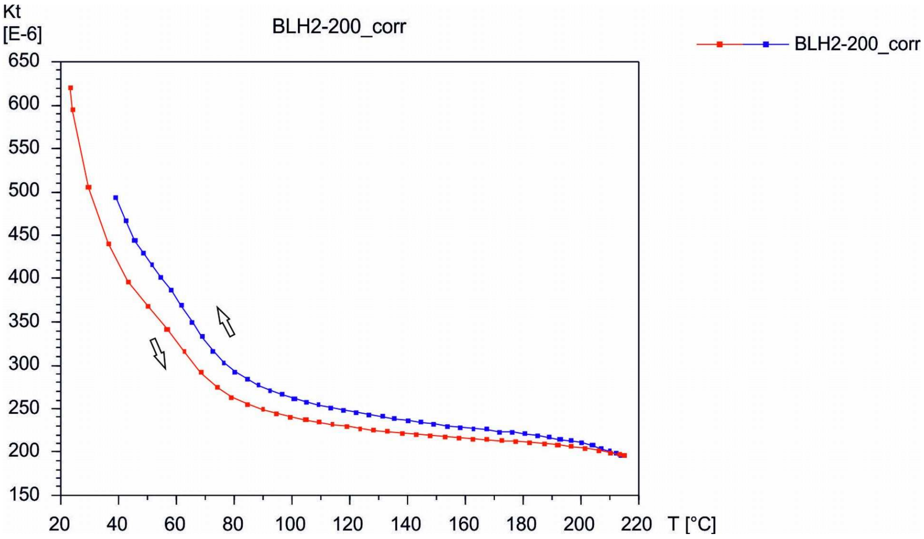
Kt
[E-6]
BLH2-200_corr
BLH2-200_corr
650
600
550
500
450
400
350
300
250
200
150
20
40
60
80
100
120
140
160
180
200
220
T [°C]

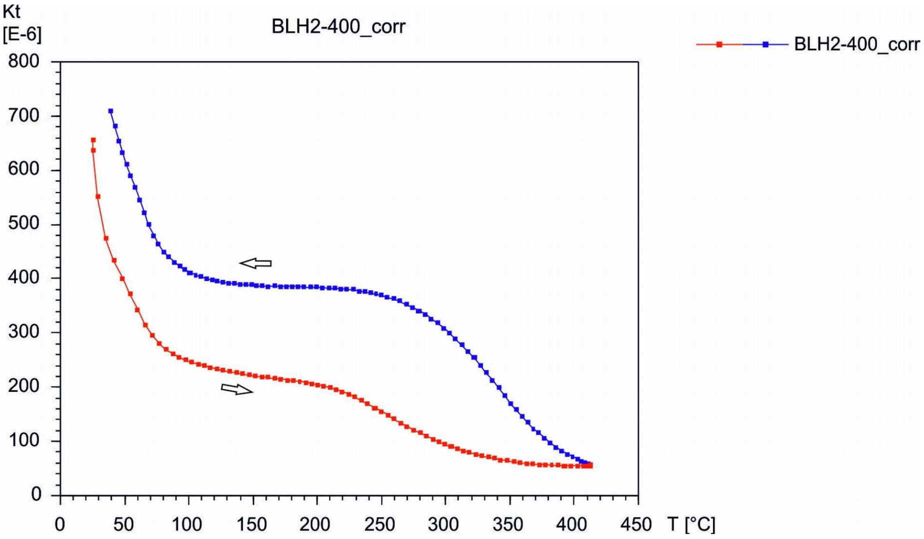
Kt
[E-6]
BLH2-400_corr
BLH2-400_corr
800
700
600
500
400
300
200
100
0
0
50
100
150
200
250
300
350
400
450
T [°C]

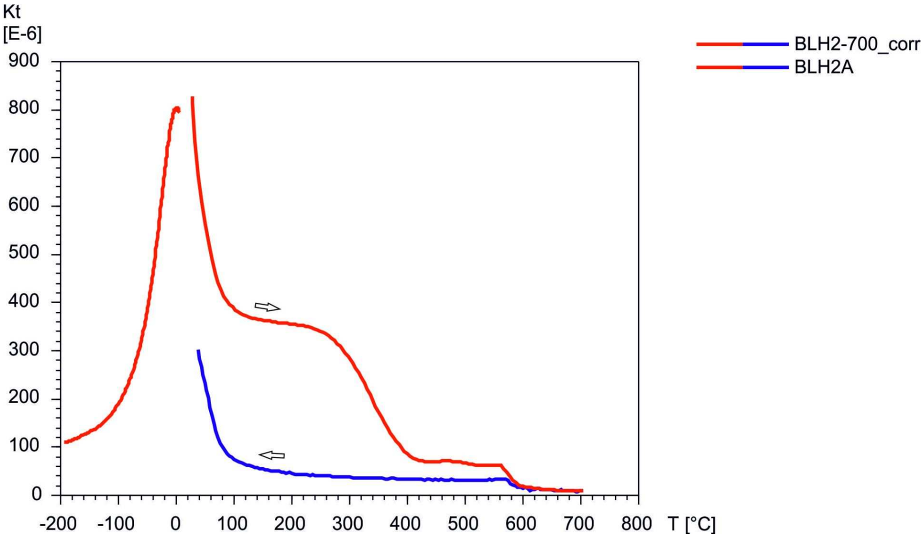
Kt
[E-6]
BLH2-700_corr
BLH2A
900
800
700
600
500
400
300
200
100
0
-200
-100
0
100
200
300
400
500
600
700
800
T [°C]

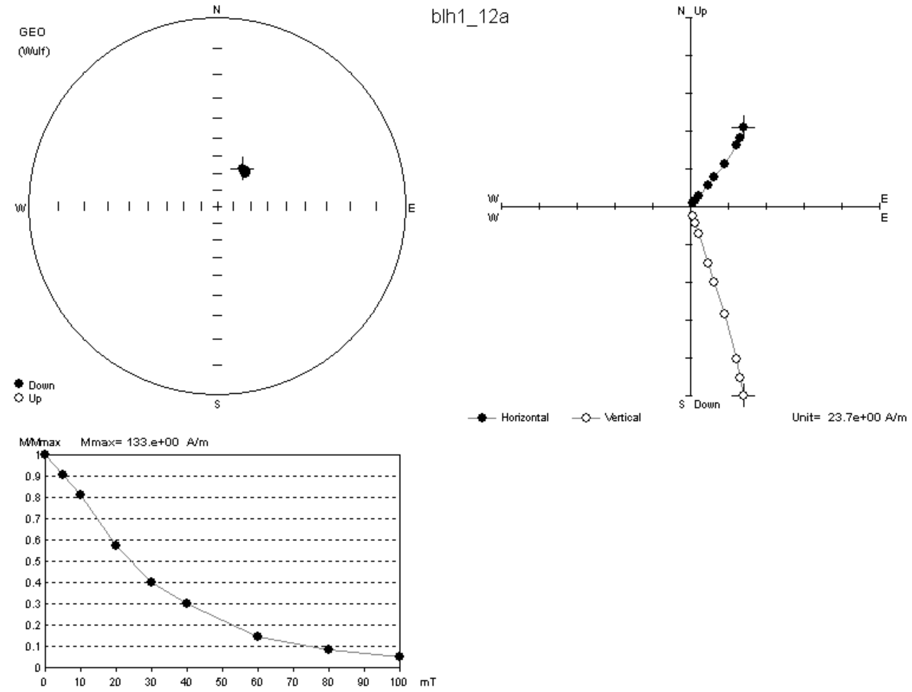

BLH1_12a: MDF = 24,1 MT

Klifhraun KLH

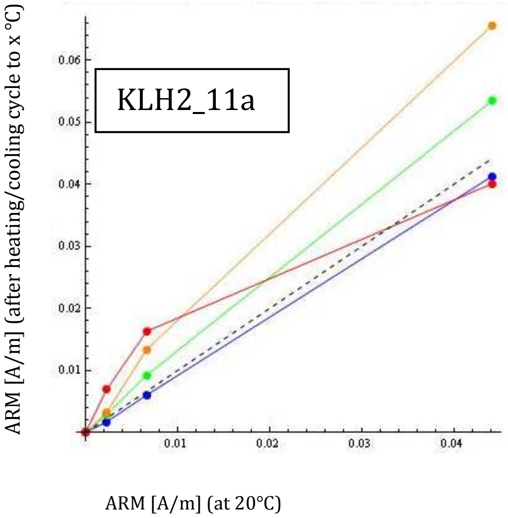

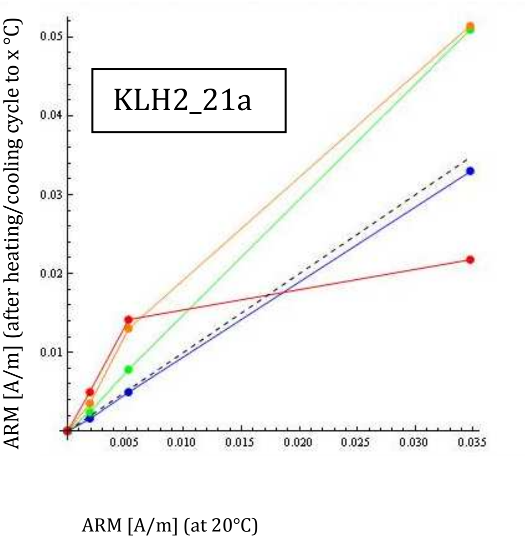

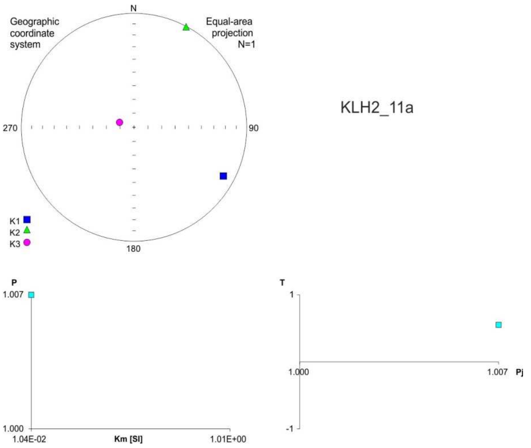
Geographic coordinate system
N
Equal-area projection N=1
270
90
180
KLH2_11a
K1
K2
K3
P
1.007
1.000
1.04E-02
Km [SI]
1.01E+00
T
1
1.000
1.007
Pj
-1

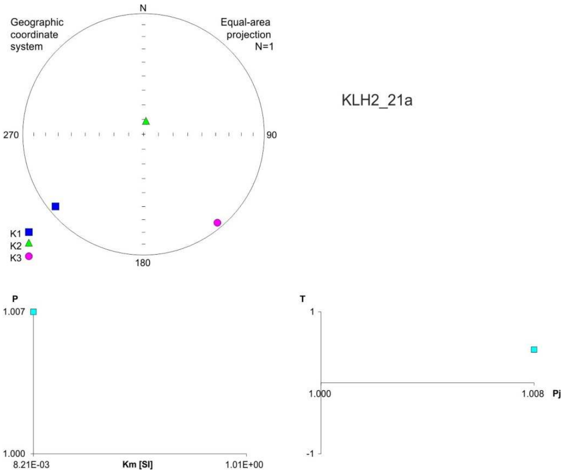
Geographic coordinate system
N
Equal-area projection N=1
270
90
180
KLH2_21a
K1
K2
K3
P
1.007
1.000
8.21E-03
Km [SI]
1.01E+00
T
1
1.000
1.008
Pj
-1

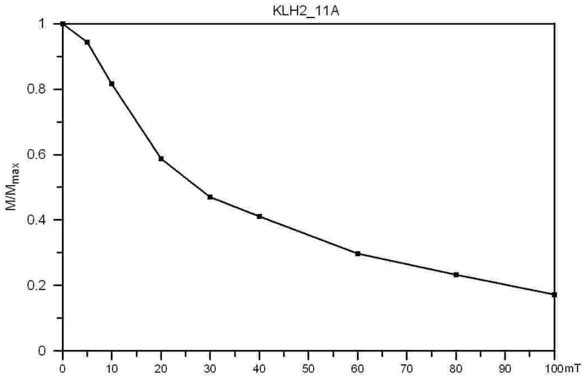
KLH2_11A
M/Mmax
1
0.8
0.6
0.4
0.2
0
0
10
20
30
40
50
60
70
80
90
100mT

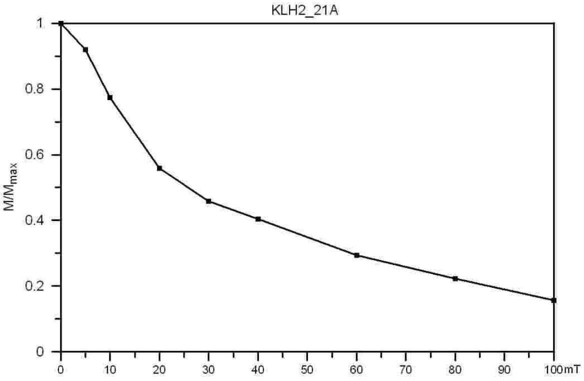
KLH2_21A
M/Mmax
1
0.8
0.6
0.4
0.2
0
0
10
20
30
40
50
60
70
80
90
100mT

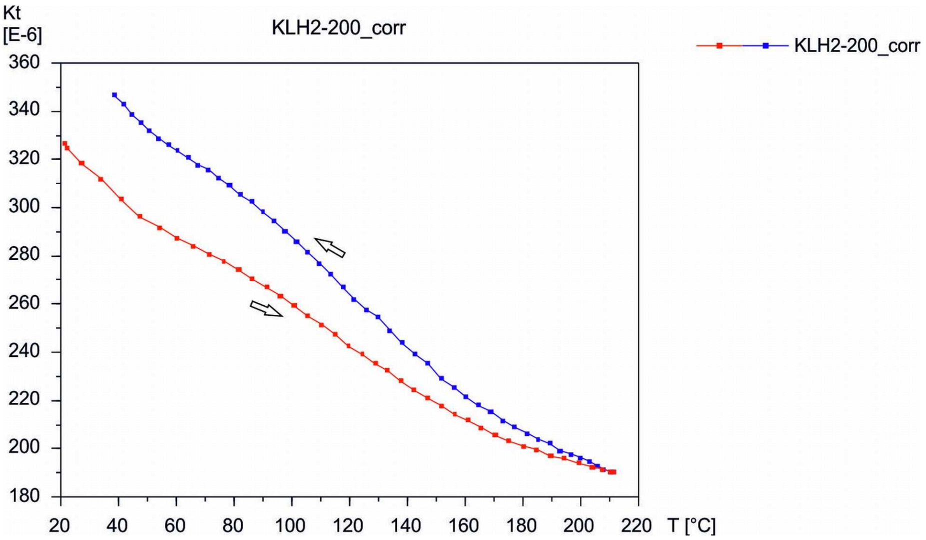
Kt [E-6]
KLH2-200_corr
360
340
320
300
280
260
240
220
200
180
20
40
60
80
100
120
140
160
180
200
220
T [°C]
KLH2-200_corr

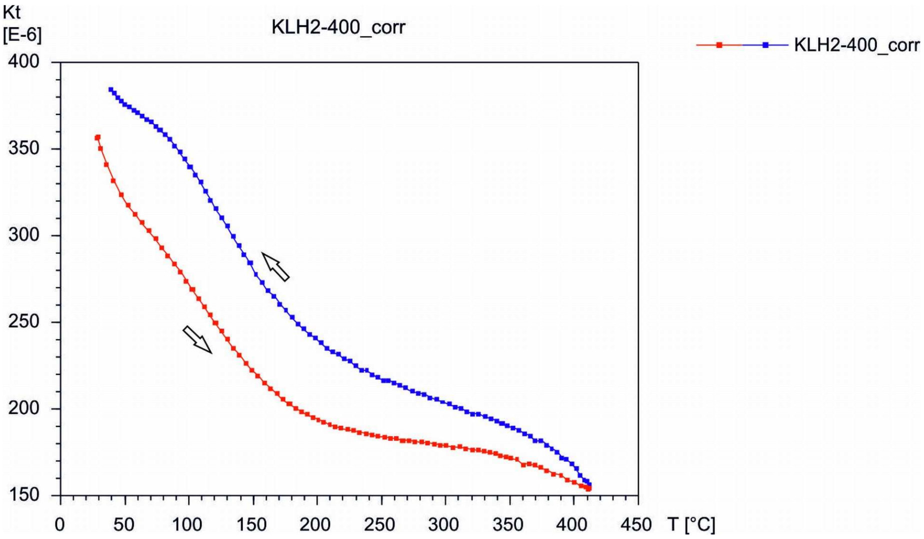

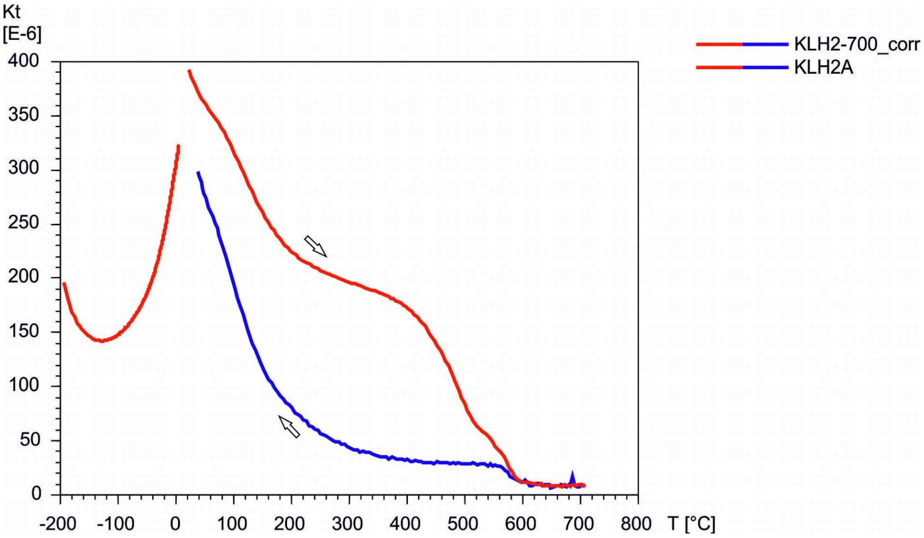

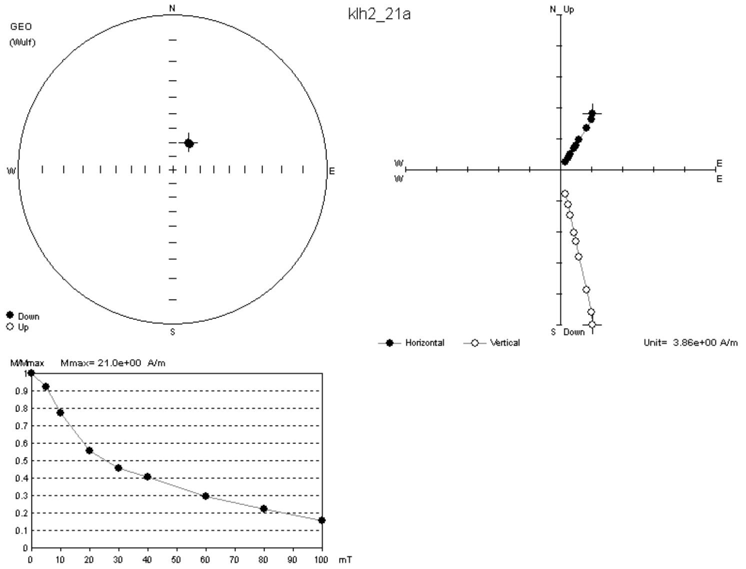

KLH2_21a: MDF = 25,8 mT

7 References

Allen C.C., 1979, Volcano-ice interactions on Mars, J.Geophys.Res. 84, pp 8048-8059.

Andrews, J.T., et al., 2000, The N and W Iceland Shelf: insight into the Last Glacial Maximum ice extent and deglaciation based on acoustic stratigraphy and basal AMS dates, Quaternary Sci. Rev. 19, pp. 619-631.

Arai, Y., 1963, Secular variation in intensity of the past geomagnetic field, M.Sc. thesis, pp 84, Univ. Tokyo, Tokyo.

Bourgeois et al., 1998, Pleistocene subglacial volcanism in Iceland: tectonic implications, Earth planet Sci. Lett. 164, pp. 165-178.

Butler, R.F., 1992, Paleomagnetism: Magnetic Domains to Geologic Terranes. Blackwell, Boston, pp. 319.

Coe, R.S., 1967a, The determinations of paleointensities of the Earth’s magnetic field with emphasis on mechanisms which could cause non-ideal behavior in Thelliers method. J. Geomagn. Geoelectr. 19, pp. 157–179.

Coe, R.S., 1967b, Paleointensity of the Earth’s magnetic field determined from tertiary and quaternary rocks. J. Geophys. Res. 72, pp. 3247–3262.

Coe, R.S., Grommé, S., Mankinen, E.A., 1978, Geomagnetic paleointensities from radiocarbon-dated lava flows on Hawaii and the question of the Pacific nondipole low. J. Geophys. Res. 83, 1740–1756.

Einarsson P., et al., 1997, Centre of the Iceland hotspot experiences volcanic unrest. EOS, Trans., Am. Geophys. Union 78, pp. 374-375.

Einarsson, P., 1991, Geologie von Island, Gesteine und Landschaften, Verlag Mál og menning, Reykjavík, pp 299.

Eysteinsson H., Gunnarsson K., 1995, Maps of gravity, bathymetry and magnetic for Iceland and surroundings In: vol. Orkustofnun, Reykjavik, 05-95055/JHD-07.

Fabian, K., 2000. Acquisition of thermoremanent magnetization in weak magnetic fields. Geophys. J. Int. 142, 478–486.

Fabian, K., 2001, A theoretical treatment of paleointensity determination experiments on rocks containing pseudo-single or multi domain magnetic particles. Earth Planet. Sci. Lett. 188, pp. 45–58.

Fisher, R., 1953, Dispersion on a sphere. Proc. R. Soc. London, Ser. A 217, pp. 295-305.

Geirsdóttir, Á. et al., 2007, Glaciation, erosion, and evolution of Iceland, J Geodynamics 43, pp. 170-186.

Goguitchaichvili, A., et al., 1999, An attempt to determine the absolute geomagnetic field intensity in southwestern Iceland during the Gauss-Matuyama reversal, Phys. Earth Planet. Inter., 115, 53–66.

Gromme, C.S., et al., 1969, Magnetic Properties and Oxidation of Iron-Titanium Oxide Minerals in Alae and Makaopuhi Lava Lakes, Hawaii, J. Geophys. Res., 74(22), pp. 5277-5293.

Gudmundsson, A.I., Kjartansson, H., 1984, Guide to the geology of Iceland, Bókaútgáfan Örn og Örlygur hf, Reykjavík.

Hardarson, B.S., et al., 1997, Rift relocation – geochemical and geochronological investigation of a paleo-rift in northwest Iceland, Earth and Planet Sci. Lett. 153, pp 181-196.

Hemetsberger, S., 2002, Untersuchung der magnetischen Suszeptibilitätsanomalie entlang der steirischen Eisenstrasse, Diploma Thesis, Universität Leoben, 80 S., Leoben.

Hug-Fleck, C J., 1987, Island geologisch-vulkanologische Momentaufnahme einer Vulkaninsel, Kneissl-Touristik – der Natur auf der Spur, Elzach-Katzenmoos.

Hug-Fleck, C., 1988, Islands Geologie, Conrad Stein, Kiel.

Jacoby, W., Gudmundsson, M., 2007, Preface Hotspot Iceland: An introduction, J Geodynamics 43, pp. 1-5.

Jelinek, V., 1978, Statistical processing of anisotropy of magnetic susceptibility measured on groups of specimens. Studia Geophys. et geol., 22, pp. 50–62.

Jelinek, V., 1981, Characterization to the magnetic fabric of rocks. Tectonophys., 79, pp. 63–67.

Jóhannesson H., Flores R. M., Jónsson J., 1981, A short account of the Holocene tephrachronology of the Snæfellsjökull central volcano, Western Iceland, Jökull 31, pp. 23-30.

Kosterov, A.A., Prévot, M., 1998, Possible mechanisms causing failure of Thellier paleointensity experiments in some basalts, Geophys. J. Int. 134, pp 554–572.

Krása, D., Heunemann, C., Leonhardt, R., Petersen, N., 2003, Experimental procedure to detect multidomain remanence during Thellier–Thellier experiments, Phys. Chem. Earth 28, pp. 681–687.

Kristjánsson, L. et al., 2003, A detailed paleomagnetic study of the oldest (approximate to 15 Myr) lava sequences in Northwest Iceland, Geophysical Journal International 155, pp. 991-1005.

Lanos, Ph., et al., 1999, Archeomagnetism, methodology and applications: implementation and practice of the archeomagnetic method in France and Bulgaria, European J. Archaeology, 2(3), pp. 365–392.

Larson, G., et al., 2002, Correlation of late Holocene terrestrial and marine tephra markers, north Iceland: implications for reservoir age changes, Polar Research 21(2), pp. 283-290.

Leonhardt, R., Matzka, J., Menor, E.A., 2003, Absolute paleointensities and paleodirections from Fernando de Noronha, Brazil. Phys. Earth Planet. Int. 139, pp. 285–303.

Leonhardt, R., Heunemann, C., Krása, D., 2004, Analyzing absolute paleointensity determinations: Acceptance criteria and the software ThellierTool4.0, Geochem. Geophys. Geosyst., Vol. 5.

Leonhardt, R., Krása, D., Coe, R.S., 2004b. Multidomain behavior during Thellier paleointensity experiments: a phenomenological model. Phys. Earth Planet. Int. 147, 127–140.

Leonhardt, R., Fabian, K., and Schnepp, E., 2010, Holocene global geomagnetic field reconstruction based on archeomagnetic data: Assessing error sources and uncertainties, conference abstract.

Moorbath S., Sigurdsson, H., Goodwin, R., 1968, K-Ar ages of the oldest exposed rocks in Iceland, Earth planet. Sci.Lett.4, pp. 197-205.

Morris, A., 2003, A Paleomagnetic and rock magnetic glossary. Tectonophysics, 377, pp. 211-228.

Moskowitz, B.M., 1981, Methods for estimating Curie temperatures of titanomaghemites from experimental Js-T data, Earth and Planetary Science Letters Volume 53, pp 84-88.

Neél, L., 1948, Magnetic properties of ferrites: ferrimagnetism and antiferromagnetism. Ann. Phys. 3, pp. 137-198.

Perrin, M., 1998, Paleointensity determination, domain structure, and selection criteria. J. Geophys. Res. 103, pp 30591–30600.

Petrovsky, E., Kapicka, A., 2006, On determination of the Curie point from thermomagnetic curves, J. Geophys. Res., Vol. 111.

Riisager, P., and Riisager, J., 2001, Detecting multidomain magnetic grains in Thellier paleointensity experiments, Phys. Earth Planet. Inter., 125, pp 111–117.

Rogers, J., et al., 1979, Magnetic anisotropy in ancient pottery, Nature Vol. 277, pp. 644-646.

Saemundsson, K., 1978, Fissure swarms and central volcanoes of the Neovolcanic zones of Iceland, Geol. J. Spec. Issue 10, pp. 415-432.

Saemundsson, K., 1979, Outline of the geology of Iceland, Jökull 29, pp. 7-28.

Schell, Ch., 2006, Characterization of geological structures by using petrophysical parameters and the effect of anisotropy, Diploma Thesis, University of Leoben, Leoben.

Schnepp, E., Lanos, P. and Chauvin, A., 2009, Geomagnetic paleointensity between 1300 and 1750 A.D. derived from a bread oven floor sequence in Lübeck, Germany, Geochem. Geophys. Geosyst., 10, Q08003, doi:10.1029/2009GC002470

Selkin, P.A., Tauxe, L., 2000, Long-term variations in paleointensity. Phil. Trans. Roy. Soc. Lond. 358, pp. 1065–1088.

Shcherbakov, V.P., McClelland, E., Shcherbakova, V.V., 1993, A model of multidomain thermoremanent magnetization incorporating temperature-variable domain structure. J. Geophys. Res. 98, pp 6201–6216.

Shcherbakova, V.V., Shcherbakov, V.P., Heider, F., 2000, Properties of partial thermoremanent magnetization in pseudosingle domain and multidomain magnetite grains. J. Geophys. Res. 105, pp. 767–781.

Smith, K. T., Sigurðsson, F., Sturkell, E., 2008, Palaeoenvironmental Reconstruction as a Tool in Hazard Assessment: a case study at Snæfellsjökull, Raunvísindaþing – Natural Science Symposium, Program Abstracts, p. 160.

Smith, Kate and Sigmundsson, Freysteinn 2007, Volcanogenic hazards and risks to road systems, Rannsóknir Vegagerðarinnar, Ráðstefna á Hótel Nordica 2. Nóvember 2007. Conference abstract.

Soffel, Chr., 1991, Paläomagnetismus und Archäomagnetismus. Springer Verlag, Berlin – Heidelberg – New York, pp. 276.

Steinthórsson, S., 1976: Tvær nýjar C14-aldursákvarðanir á öskulögum úr Snæfellsjökli, Náttúrufræðingurinn 37, pp 236-238.

Stuiver, M., Reimer, P.J., 1993, Extended C-14 data-base and revised Calib 3.0 C-14 age calibration program, Radiocarbon 35, pp 215-230.

Tarling, D. H., Hrouda, F., 1993, The Magnetic Anisotropy of Rocks. Chapman & Hall, London, pp. 217.

Tauxe, L., 1998, Paleomagnetic Principles and Practice, Kluwer Academic Publishers, London.

Tauxe, L., 2009, Essentials of Paleomagnetism: Web Edition 1.0 (March 18, 2009), <http://magician.ucsd.edu/Essentials/>

Telford, W.M., et al., 1990, Applied Geophysics, 2nd ed., ISBN 0521339383. Cambridge, UK: Cambridge University Press, pp. 790.

Thellier, E., 1938, Sur l'animantation des terres cuites et ses applications géophysiques. Thése de Doctorat, Paris, tire à part de: Ann. Inst. Phys. Globe Paris, 16, pp. 157-302.

Thellier, E., Thellier, O., 1959, Sur l'intensité du champ magnétique terrestre dans le passé historique et géologique. Ann. Géophys. 15, pp. 285–376.

Thordarson, T., Höskuldsson, Á., 2006 (2nd edition), Classic Geology in Europe 3, Iceland, Harpenden: Terra Publishing.

Tryggvason, K., Huseby, E.S., Stefansson, R., 1983, Seismig image of the hypothesized hot spot, Tectonophysics 100, pp. 97-118.

Veitch, R.J., et al., 1984, An investigation of the intensity of the geomagnetic field during roman times using magnetically anisotropy bricks and tiles, Arch. Sc. Genève, Vol. 37, pp. 359-373.

Werner, R., Schmincke, H.U., Sigvaldson, G., 1996, A new model for the evolution of table mountains: volcanological and petrological evidence from Herdubreid and Herdubreidatögl volcanoes (Iceland), Geolog. Rundschau. 85, pp. 390-397.

Zijderveld, J. D. A., 1967, Demagnetization of rocks, Analysis of results. In: Collinson, D.W., Creer, K.M. and Runcorn, S. K. (Editors), Methods in Paleomagnetism. Elsevier, Amsterdam, pp. 254-286.